NASA-CR-194771

NAGW-3150
IN-47-CR
OCIT.
198564

133P

A REGIONAL ANALYSIS OF CLOUDY MEAN SPHERICAL ALBEDO OVER THE MARINE STRATOCUMULUS REGION AND THE TROPICAL ATLANTIC OCEAN

A Thesis

Submitted to the Faculty

of

Purdue University

by

Kathryn M. Ginger

In Partial Fulfilment of the

Requirements for the Degree

of

Master of Science

December 1993

(NASA-CR-194771) A REGIONAL ANALYSIS OF CLOUDY MEAN SPHERICAL ALBEDO OVER THE MARINE STRATOCUMULUS REGION AND THE TROPICAL ATLANTIC OCEAN M.S. Thesis (Purdue Univ.) 133 p

N94-24049

Unclas

G3/47 0198564

ACKNOWLEDGMENTS

I would especially like to thank my parents for their love and support. Mom, you have always made me feel special and as if I could do anything. Dad, thanks for helping me move countless times during my grad school career. I won't forget the radiator episode in going to Colorado.

I would like to thank Suzanne and Mike (the Hoosiers) for offering good humor, sound legal and personal advice and for being interested in meteorology. I really look up to you guys. What's a gustfront!?!

Thanks, Lizzy and Jon. Your emotional support during the rough times of the last two years has been a saving grace.

Thanks, Anne (the Chicker) for making me a meteorologist with style! Not all scientists are as weird as you think. Thanks for taking care of the MOO in my absence.

I would like to thank Timmy B. for his love and support. Thank you for the Saturday morning gab sessions and the times we have beep-bopped around the country in the last two years, but most of all thanks for being my best friend and being there when I needed you . . . and the popcorn.

I would like to thank Brendan Larson for a listening ear and interesting weather discussions.

I would like to thank Wendy Abshire for making my stays at COMET enjoyable and a great learning experience. Next time Falafel King is on me.

I would like to thank my fellow meteorologist, Mindi King, for being a great roommate and study buddy (especially on the Z-O equation).

A special thanks goes to Perry Ramsey, Mark Bourassa, and Rich Cullather (alias The Dirty Clubs Gang) for thoughtful insights, provocative political commentary and fantastic card games and not to mention a lot of help in putting this document together.

Another special thanks goes to Dr. Tim Spangler who made me realize that yes, I could be a meteorologist.

And finally, I would like to thank my committee members . . . Dr. Harshvardhan for giving me the freedom to pursue other interests not related to my thesis, Dr. Snow for introducing me into Project Atmosphere and Dr. Smith for very helpful suggestions on clarifying the content of this work.

This research was sponsored by the National Aeronautics and Space Administration under Grant NAGW-3150.

TABLE OF CONTENTS

LIST OF TABLES

LIST OF FIGURES

Figure Page

Figure Page

ABSTRACT

Ginger, Kathryn M. M.S., Purdue University, December 1993. A regional analysis of cloudy mean spherical albedo over the marine stratocumulus region and the tropical Atlantic ocean. Major Professor: Harshvardhan.

Since clouds are the largest variable in Earth's radiation budget, it is critical to determine both the spatial and temporal characteristics of their radiative properties. This study examines the relationships between cloud properties and cloud fraction in order to supplement grid scale parameterizations. The satellite data used in this study is from three hourly ISCCP (International Satellite Cloud Climatology Project) and monthly ERBE (Earth Radiation Budget Experiment) data on a 2.5° × 2.5° latitude-longitude grid. Mean cloud spherical albedo, the mean optical depth distribution and cloud fraction are examined and compared off the coast of California and the mid-tropical Atlantic for July 1987 and 1988. Individual grid boxes and spatial averages over several grid boxes are correlated to Coakley's (1991) theory of reflection for uniform and broken layered cloud and to Kedem, et al.'s (1990) findings that rainfall volume and fractional area of rain in convective systems is linear. Kedem's hypothesis can be expressed in terms of cloud properties. That is, the total volume of liquid in a box is a linear function of cloud fraction.

Results for the marine stratocumulus regime indicate that albedo is often invariant for cloud fractions of 20% to 80%. Coakley's satellite model of small and large clouds with cores (1 km) and edges (100 m) is consistent with this observation. The cores maintain high liquid water concentrations and large droplets while the edges contain low liquid water concentrations and small droplets. Large clouds are just a collection of cores.

The mean optical depth (TAU) distributions support the above observation with TAU values of 3.55 to 9.38 favored across all cloud fractions. From these results, a method based upon Kedem, et al's theory is proposed to separate the cloud fraction and liquid water path (LWP) calculations in a general circulation model (GCM). In terms of spatial averaging, a linear relationship between albedo and cloud fraction is observed.

For tropical locations outside the Intertropical Convergence Zone (ITCZ), results of cloud fraction and albedo spatial averaging followed that of the stratus boxes containing few overcast scenes. Both the ideas of Coakley and Kedem, et al. apply. Within the ITCZ, the grid boxes tended to have the same statistical properties as stratus boxes containing many overcast scenes. Because different dynamical forcing mechanisms are present, it is difficult to devise a method for determining subgrid scale variations. Neither of the theories proposed by Kedem, et al. or Coakley works well for the boxes with numerous overcast scenes.

1. INTRODUCTION

Clouds are the largest variable in Earth's radiation budget, so it is critical to determine both the spatial and temporal characteristics of their radiative properties. Clouds absorb and emit long wave radiation, provide for the release of latent heat, allow for the redistribution of sensible heat, and reflect the majority of incident short wave radiation that is reflected by the Earth system. Thus, they act as the vital link between radiative processes, atmospheric dynamics and hydrology (Coakley, 1991; Sheu and Curry, 1992; Xu and Krueger, 1991).

As an example, marine stratocumulus clouds may produce the largest increase in reflected radiation for a given small change in emitted radiation (Cahalan and Snider, 1989; Ohring and Clapp, 1980; Hartmann and Short, 1980). Radiative cooling then increases at cloud top and possibly leads to an enhancement of precipitation in convectively unstable clouds (Cotton and Anthes, 1990).

Because climate modeling attempts to incorporate the above mentioned link, it is important to be able to evaluate cloud radiative properties at both the grid and subgrid scales. According to Cess et al. (1990), it is the difference in general circulation model (GCM) cloud parameterizations which leads to variable radiative responses among various GCM's. Once cloud radiative properties like liquid water path (LWP) and albedo are better known and properly parameterized, widespread acceptance of climate model predictions is likely.

Two problems of the parameterization process are grid resolution and the non-linearity of cloud radiative properties. In terms of resolution, most general circulation models have a horizontal grid spacing of 250 km or greater. On the other hand, clouds exhibit variability on a scale of less than 8 km. Clouds themselves also exhibit a non-linear relationship between cloud liquid water and radiative properties like albedo. These concerns are intertwined because cloud microphysical and morphological properties are related to area mean radiative properties.

A previous study by Avaste et al. (1979) dealt with the resolution problem and monthly mean albedo. Avaste et al. (1979) examined monthly mean cloud amounts over the GATE area (5° S to 20° N and 50° W to 10° W) for the years 1965 to 1972. The region was divided into 10° × 10°, 5° × 5°, and 2.5° × 2.5° quadrangles. Figure 1.1 schematically illustrates an example of his results. In the front quadrant at the higher resolution, the cloud amount may be 50% while at the coarser resolution, the cloud amount may be 100%. Not only increases in cloud amount may arise, but decreases may occur as well. Look at the left and rear quadrants where the high resolution registers 25% cloud fraction and the low resolution measures 0% cloud fraction. Because GCM's often weight radiative transfer by cloud fraction, the importance of the above variation is apparent.

Avaste et al. (1979) also made a comparison of albedo versus cloud amount for thirty-degree latitudinal oceanic belts. The monthly mean albedo included both the surface and cloudy albedo. However, the albedo measurements did not correspond in time to the cloud amount data. The results for the month of March suggest a linear relationship, but one in which extrapolating to zero cloud amount gives a negative surface albedo (Avaste et al., 1979). The study concluded that satellite derived irradiances at sufficiently small grid scales and automated analysis are the key elements in developing a global cloud climatology.

Over the past decade, a wealth of satellite data has been archived through such programs as the International Satellite Cloud Climatology Project (ISCCP), the First ISCCP Regional Experiment (FIRE) and the Earth Radiation Budget Experiment (ERBE). However, Rossow (1989) points out that "obtaining a quantitative understanding of global cloudiness has been slow."

A recent study by Coakley (1991) used one-kilometer AVHRR (Advanced Very High Resolution Radiometer) data to examine properties of uniform and broken layered clouds. For maritime stratocumulus clouds, it was found that at visible wavelengths, the average reflectance of broken clouds was approximately 80 to 85% of that for uniform clouds. From the above observations, Coakley proposes an idealized cloud model. As shown in Figure 1.2, Coakley's model contains clouds with "cores" of high liquid water content and large droplet size and "edges" of low liquid water content and small droplet size. A typical core is about 1 km in width while an edge is about 100 m in width. A broken cloud may be represented by a single core and its surrounding edge, while uniform clouds are a cluster of cores and intermingled edges.

During this same period of intensive satellite data gathering, GCM's have been incorporating physically based cloud radiative parameterizations. Thus, it is the objective of this study to use ISCCP and ERBE information as data sources for determining relationships between cloud properties and cloud fraction in order to supplement grid-scale GCM parameterizations. It is a climate model problem of cloud properties and their relationship to the radiation budget.

In order to determine relationships between regional mean cloudy albedo and cloud fraction, a study of the marine stratocumulus regime off the coast of California for July of 1987 and 1988 is presented. Relationships between ISCCP cloud fraction and albedo are drawn for typical GCM grid boxes and much larger regional domain areas. Probability distribution functions for the mean optical depth, TAU, are also presented for the grid boxes. Monthly mean ERBE scanner data (2.5° × 2.5° grid scale) of outgoing long wave radiation (OLR) and short wave (SW) albedo provides additional cloud property information for each domain area. Since marine stratocumulus has been selected as an area of study, this paper's results are compared to Coakley's findings for the same cloud type. To incorporate convective clouds, the central tropical Atlantic ocean is also studied and compared against the stratocumulus regime. Even though no comparisons are made to actual GCM output, the results of the above study will provide information for verifying and tuning GCM calculations.

Chapters 2 and 3 present a framework for satellite and GCM cloudiness, respectively. Chapter 4 presents the structure of the ISCCP satellite dataset. Chapter 5 introduces the procedure by which the mean cloudy albedo is calculated for the marine stratocumulus and tropical regimes at varying horizontal resolutions. Chapter 6 explains the reasons for favoring a spatial average over a time average. Chapter 7 describes the results of the marine stratocumulus regime and its relationship to Coakley's model. Chapter 8 describes the tropical results. And finally, Chapter 9 offers a conclusion and some suggestions for further study.

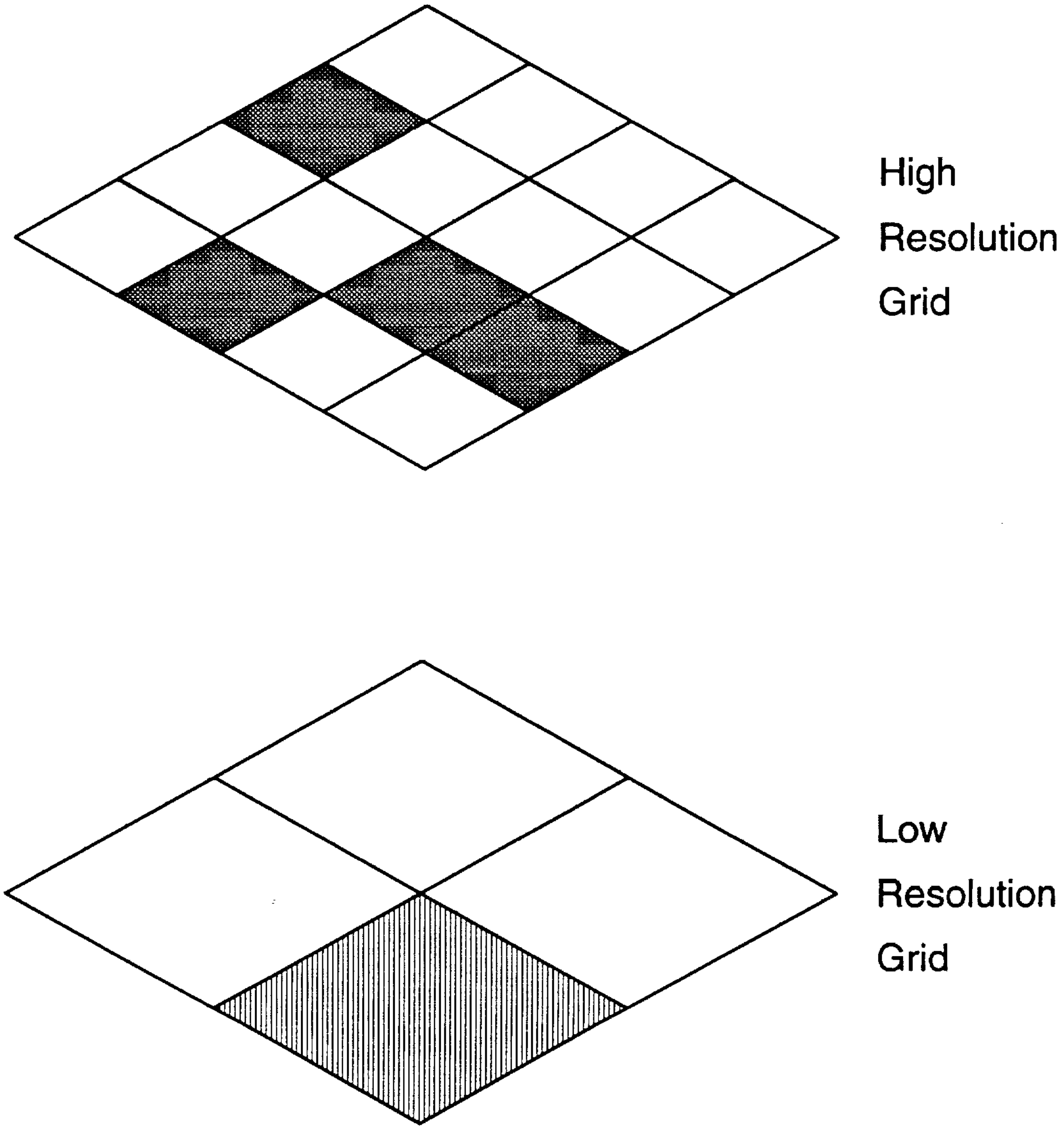

Figure 1.1 An example of the effect of grid resolution on cloud amount, (After Harshvardhan et al., 1993).

SMALL CLOUDS

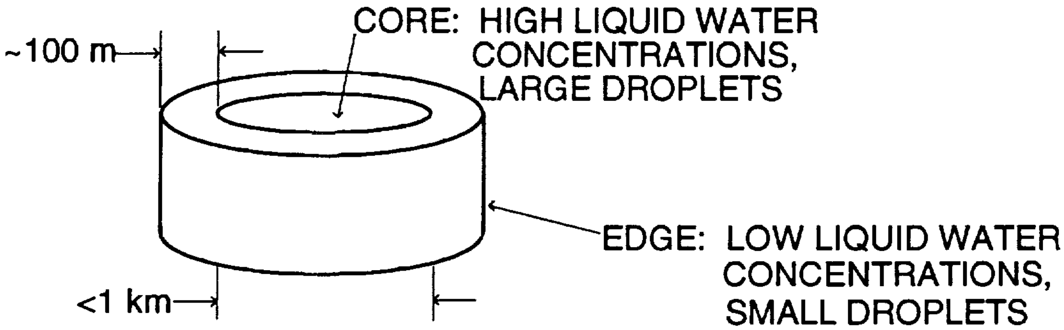

LARGE CLOUDS

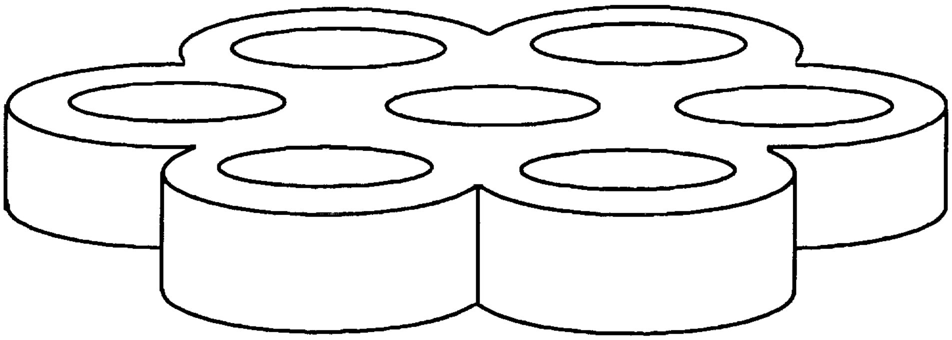

Figure 1.2 Cloud model deduced from satellite observations, (After Coakley, 1991).

2. SATELLITE FRAMEWORK

In an attempt to interpret cloud properties, particularly albedo and liquid water content, researchers have used satellite-based observations. As mentioned previously, Avaste et al. (1979) examined cloud amount from spatial averages of a satellite based cloud atlas. Hughes and Henderson-Sellers (1983) also performed spatial and temporal averages of three dimensional nephanalyses provided by the U. S. Air Force while Cahalan and Snider (1989) studied spatial coherence plots of LANDSAT data.

Avaste et al. (1979) illustrated how cloud fraction and monthly mean albedo change over different resolutions. Hughes and Henderson-Sellers (1983) attempted to infer cloud size from mean cloud amount. Cahalan and Snider (1989) concluded that large scale satellite brightness variations are strongly influenced by liquid water variations. Occasionally, changes in liquid water content are a reflection of vertical velocity.

During the following analysis of mean spherical albedo versus cloud fraction, albedo changes are illustrated on a grid resolution Avaste had available. However, the influence of cloud size, as studied by Hughes and Henderson-Sellers, can not be determined explicitly from ISCCP data. Only an estimate of areal coverage can be calculated. Finally, liquid water variations can only be inferred from ISCCP optical depth distributions. Since a stated goal of ISCCP (Rossow et al., 1988) is to translate satellite information into a cloud radiation scheme that can be used in an atmospheric model, it is necessary to create a discrete model of satellite cloudiness and discuss the effectiveness of ISCCP data as a diagnostic tool before analyzing the above optical properties.

ISCCP Model of Cloudiness

For an ISCCP model of cloudiness, each satellite scene is a box of constant latitude, ΔL, and variable longitude, Δx. Within this box, there are square pixels of side Δp every 25 km. For ISCCP, this pixel footprint is 8 km. A pixel is cloudy if either the measured visible (0.63 μm) radiance value exceeds or the infrared (11 μm) brightness temperature is less than its respective threshold value for a particular earth location (Rossow et al., 1988). The threshold values are part of a map of clear sky composites for all times and locations.

To determine the threshold values, it is assumed that clear scenes are less variable than cloudy scene radiances (Rossow and Schiffer, 1991). Then by using properties of Earth's surface and modeling radiative transfer in a clear atmosphere, a map of the clear sky composites is generated. The composites are the visible and infrared threshold values.

The visible threshold equation takes the form:

$$I_t = I_{clr} + a(S_0/\pi), \qquad \text{(VISIBLE)} \qquad (1)$$

where I_t is the visible threshold radiance value in $Wm^{-2}sr^{-1}\mu m^{-1}$, I_{clr} is the visible clear sky radiance value in $Wm^{-2}sr^{-1}\mu m^{-1}$, S_0 is spectral solar flux for the satellite channel in $Wm^{-2}\mu m^{-1}$, a is a corrective percentage based upon surface type.

The infrared threshold equation takes the form:

$$T_t = T_{clr} - b, \qquad \text{(INFRARED)} \qquad (2)$$

where T_t is the infrared threshold brightness temperature in degree Kelvin, T_{clr} is the infrared clear sky brightness temperature in degree Kelvin, and b is a temperature correction based upon surface type.

For both equations, the different surfaces are low variability water, high variability water, land (including sea ice), topographic regions, and permanently ice-covered land. Visible radiances represent a percentage of the instrument response obtained when measuring the complete solar flux, while infrared radiances are represented as brightness temperatures (Wielicki and Parker, 1992; Rossow et al., 1988). A threshold value is exceeded for cloudy pixels if $I_m > I_t$ or if $T_m < T_t$, where I_m is the measured radiance and T_m is the measured brightness temperature. The above approach relies only on information of the analyzed satellite images (Rossow, 1989).

Thus, a discrete model of satellite cloudiness consists of pixels of approximately the same size and the pixel radiance or brightness temperature exceeding a threshold (Wielicki and Welch, 1986; Wielicki and Parker, 1992; Chang and Coakley, 1993). By using these pieces of information and knowing the areal distribution within a box, the cloud fraction is determined as well as grid mean radiative properties (Harshvardhan et al., 1993).

It is also important to note here that the greatest uncertainty in the ISCCP cloud algorithm is "the assumption that all image pixels containing cloud are completely covered by a single homogeneous layer" (Rossow and Schiffer, 1991). However, preliminary results indicate cloud detection is excellent in the marine stratocumulus region (Rossow and Schiffer, 1991). For the tropics, specifically in the ITCZ, cloud detection is mixed. As long as a convective tower and associated anvil are one entity, determining optical properties is better than when a tower collapses and only the anvil remains. Thus, performance in the zones of the trade winds is not as good as the ITCZ.

ISCCP Data Versus LANDSAT Data

In order to determine the appropriateness of ISCCP data as a diagnostic tool, Harshvardhan et al. (1993) conducted a comparison of cloud detection, cloud threshold and satellite resolution between ISCCP data and the much finer resolution 57-meter LANDSAT data. For cloud detection, both the ISCCP and LANDSAT algorithms (Wielicki and Parker, 1992) use a bispectral method. As mentioned previously, ISCCP uses visible radiances and infrared brightness temperatures (Rossow et al., 1988), while LANDSAT uses nadir reflectance (0.83 μm) and visible brightness temperatures (Wielicki and Parker, 1992). By starting with the same resolution data (e.g., 1/16-kilometer pixel resolution) and applying both the LANDSAT and ISCCP cloud detection routines, lower cloud fractions and higher nadir reflectances exist for the ISCCP algorithm. Therefore, ISCCP has a more strict cloud criterion, but the trend of the data is not greatly influenced by the choice of threshold (Harshvardhan et al., 1993; Wielicki and Parker, 1992).

However, from the satellite model of cloudiness described previously, the ISCCP data pixel resolution is an 8 km footprint every 30 km. By degrading the high resolution LANDSAT data to 8 km and then applying the ISCCP cloud algorithm, the effects of resolution on the ISCCP dataset are assessed. The results of this comparison for boundary layer clouds (Harshvardhan et al., 1993) indicates an increasing cloud fraction and a decreasing reflectance for all non-completely overcast scenes.

Even though the above comparison between ISCCP and LANDSAT thresholds illustrates the effects of pixel resolution and cloud threshold, the small increase of 8.0%

from 1/16-km to 8-km resolution indicates that the ISCCP data is sufficient for modeling purposes.

3. GCM FRAMEWORK

Just as a model of satellite cloudiness is defined in the previous chapter, a GCM description of cloudiness is presented. For a GCM, cloudiness is generally classified as either stratiform or convective. The former is generated by super saturation of a grid box while the latter is generated by a convective parameterization (Harshvardhan et al., 1993). Grid box supersaturation may occur for relative humidity thresholds of 100% (Randall et al., 1989) or for some lower value if a fractional cloud cover scheme is used (Slingo, 1987). Convective parameterizations are often empirical and fall into two broad categories, moist adiabatic and penetrating convection (Cess et al., 1990). The penetrating convection scheme may use cloud mass flux or the Kuo parameterization. It is best if the criterion is based upon the cloud mass fluxes (Xu and Randall, 1992). See Cess et al. (1990) and Gates (1992) for a further listing of convective parameterizations.

Then by using cloud temperature, cloud water or altitude, diagnostic optical properties may be assigned to model generated clouds. Since model grid box properties in reality are not homogeneous, the diagnostic optical properties and cloud fraction are often "tuned" to represent small scale variations on the large scale characteristics. Then by combining the cloud optical properties, cloud cover, temperature and the gaseous constituent profile, the radiative fluxes are calculated corresponding to a model grid increment, Δx, which is typically 100-500 km. In a hypothetical sense and similar to the satellite model of cloudiness, an idealized GCM box would contain pixels of side Δp, the pixel resolution (small scale variability). The atmospheric column within these boundaries is allowed to be clear or covered by extensive clouds over a prescribed fractional area.

A pixel is either clear or cloudy but not partly cloudy. The model grid box, Δx, then contains several pixels which are clear or cloudy. The ratio of cloudy pixels to the total number of pixels is defined as the model grid cloud fraction. Each pixel is considered to be an independent contributor to the radiative flux at any vertical level of the model grid. Thus, the definition of cloud fraction here is an energy-conserving one at any pixel resolution. Unfortunately, inverting the reflected satellite radiance field to fit this pixel scheme does not work because of the nature of cloudiness. As a consequence, the satellite pixel size and reflectance above background is used to discriminate clouds and determine cloud fraction and pixel reflectance. This cloud fraction can then be used by GCM's. Then for determining grid mean radiative properties of a GCM, the distribution of reflectances over a satellite image is averaged and the contributions from clear skies is incorporated (Harshvardhan et al., 1993).

Thus, our discrete model for GCM cloudiness is as follows. Stratiform clouds are considered to exist according to a supersaturation criterion. Convective clouds are parameterized. A cloud fraction is determined. Satellite data can verify the cloud fraction parameterization for present climate simulations. Then the radiative transfer calculations are weighted by the cloud fraction. Both the cloud and radiation fields my be updated at intervals ranging from 1 to 12 hours (Harshvardhan et al., 1993).

4. DATA BASE

The ISCCP satellite data (Rossow et al., 1988) collects and analyzes satellite radiance measurements to infer the global distribution of cloud radiative properties and their diurnal and seasonal variations. This collection and analysis produces a global radiance set containing basic information on the radiative properties of the atmosphere from which cloud parameters can be derived in order to improve the relationship of actual cloud parameters to their model counterparts.

ISCCP data collection began 1 July, 1983 and still continues currently. Four different geostationary satellites (METEOSAT, GMS, GOES-WEST and GOES-EAST) provide global coverage every three hours starting at 0000 UTC. For polar coverage, the NOAA-9 and NOAA-10 satellites are included. ISCCP produces three hour (C1) and monthly (C2) cloud climatology data. Only C1 data are used in this paper.

The climatology data include location information, cloud amount, clear sky information, the distribution of cloud tops, mean radiances, mean surface and cloud properties and finally atmospheric properties. All quantities are reported for each map location and time. ISCCP provides a read program that automatically arranges the user selected data variable to an EQUAL-ANGLE configuration.

The map grid itself ranges in latitude from 90° S to 90° N and in longitude from 0° to 360° east to west. The equal angle increment is 2.5° in both latitude and longitude. The first cell corner is the intersection of the Greenwich meridian and the south pole. However, all the data quantities are reported as if they are for the center of the grid box.

For the first cell, this is 88.75° S latitude and 1.25° E longitude, and for the next cell it is 88.75° S latitude and 3.75° E longitude. The data within the map cells progresses eastward in longitude and northward in latitude. Each latitude zone is completed before moving to the next latitude zone.

In the C1 data file, the total number of pixels, the number of visible (0.63 μm) cloudy pixels, and the number of infrared (11 μm) cloudy pixels is catalogued. ISCCP also provides mean cloud radiative properties. For this study, only the mean optical depth, TAU, for visible and infrared cloudy pixels is used. Once a given visible radiance value is known and corrected for Earth-sun distance, viewing geometry and ozone absorption, the built in ISCCP radiation model uses this information, surface reflectance, and cloud top pressure to produce a cloudy visible optical depth. As a result, only daytime scenes are analyzed and no retrievals are done at night. See Rossow et al. (1988) for details. The optical depth or TAU value is an energy weighted value. Therefore, it can not be simply averaged over several grid boxes to obtain an area average optical depth. Through a look up table ISCCP converts the TAU values to linear reflectances. These reflectance values represent a spherical albedo of the cloudy portion of the grid box and are called the mean cloudy albedo. All later scatter plots for a single box or spatial average over several boxes (box groups) depict this variable versus cloud fraction.

Besides providing a single box mean cloudy TAU value, ISCCP catalogs the distribution of TAU values and different cloud top pressures for all cloudy pixels within a grid box. Table 4.1 lists the ranges of adjusted cloud top pressures and corresponding heights. Here, the word adjusted means visible radiance data is used to verify or correct the infrared assumption of opaque clouds in determining cloud top pressure.

Table 4.1 Cloud top pressure ranges and corresponding height ranges.

Pressure	Height
5 to 180 mb	12.7 to 20.7 km
180 to 310 mb	9.1 to 12.7 km
310 to 440 mb	6.6 to 9.1 km
440 to 560 mb	4.8 to 6.6 km
560 to 680 mb	3.3 to 4.8 km
680 to 800 mb	2.0 to 3.3 km
800 to 1000 mb	0.0 to 2.0 km

Within each cloud top pressure range, a distribution of TAU values and corresponding linear cloudy reflectances exists. Table 4.2 lists the categories of TAU values and their approximately equivalent reflectances.

Table 4.2 TAU categories and corresponding reflectances.

TAU	Reflectance
0 to 1.3	0 to 15 %
1.3 to 3.6	15 to 30%
3.6 to 9.4	30 to 50%
9.4 to 23	50 to 70%
23 to 125	70 to 93%

The number of satellite pixels within each TAU category is the data value provided by ISCCP. Because the TAU values are given in broad categories, the average of the range does not give an accurate representation of an individual pixel's true value. For instance, the first category gives the number of pixels with an optical depth of less than 1.3. Since most of the pixels probably have TAU values closer to 1.3, a gross underestimation of the average TAU occurs if the TAU range is averaged. However, without manipulating the data, a liquid water distribution may be inferred.

5. PROCEDURE

Since cloud variability over land is greater, the ISCCP cloud detection threshold tends to miss clouds over land (Rossow and Schiffer, 1991). Thus, only the ocean areas are considered for study. The months of July 1987 and 1988 are chosen because the 1987 FIRE (First ISCCP Regional Experiment) campaign is included. The marine stratocumulus region off the coast of California extending from 20°N to 45°N and 115°W to 155°W is the first area of study because it is the region of interest in FIRE. A second impetus for studying the marine stratocumulus regime is that it is often treated as horizontally uniform in GCM's, even though these clouds may produce large albedo changes for small OLR variations (Cahalan and Snider, 1989; Ohring and Clapp, 1980; Hartmann and Short, 1980).

Since convective clouds constitute the second most frequent cloud type, it is only logical that they be examined also. A tropical Atlantic region extending from 5°S to 35°N and 15°W to 45°W was chosen as the second area of study. The choice of the tropical Atlantic over the tropical Pacific was an arbitrary one, but it did allow most of the data to be from the METEOSAT satellite.

Figure 5.1 depicts the stratus map area while Figure 5.2 illustrates the tropical map area. On the figures, letters indicate the individual boxes of study with X marking the center of the stratus region on Figure 5.1. The tropical region is divided into two sub-regions. Figures 5.3 and 5.4 display the tropical sub-regions, areas 1 and 2, with an A or

B marking the central equal area box. The locations of the individual boxes of study are given by the following tables.

Table 5.1 Stratus box locations.

Location	Latitude	Longitude
X	32.5°N - 35.0°N	135.0°W - 138.0°W
A	25.0°N - 27.5°N	142.3°W - 145.1°W
B	30.0°N - 32.5°N	122.9°W - 125.8°W
C	42.5°N - 45.0°N	135.0°W - 138.5°W
D	22.5°N - 25.0°N	133.6°W - 136.3°W

Table 5.2 Tropical box locations.

Location	Latitude	Longitude
A	15.0°N - 17.5°N	34.0°W - 36.6°W
B	5.0°N - 7.55°N	25.2°W - 27.8°W
C	7.5°N - 10.0°N	33.0°W - 35.5°W
D	22.5°N - 25.0°N	35.5°W - 38.2°W
E	25.0°N - 27.5°N	25.1°W - 27.9°W

All spatial averaging begins at the center box and extends outward in concentric rings. For each location, the cloud fraction, mean spherical albedo, and the number of satellite pixels contained within each TAU category mentioned in Chapter 4 are calculated or are known ISCCP quantities. Although the ISCCP data is archived in an EQUAL-ANGLE format, it was originally reported in EQUAL-AREA. By discarding the duplicated EQUAL-ANGLE boxes, the EQUAL-AREA format is preserved.

The spatial mean spherical albedo, R, is calculated from the following equation,

$$R = \frac{\sum R_i C_i}{\sum C_i}, \tag{3}$$

where R_i is the mean spherical albedo for a particular box, and C_i is the number of cloudy pixels in a scene. Since only visible information is used, no temporal averaging is done.

In order to infer a liquid water distribution, the data points from the albedo versus cloud fraction graphs are sorted by cloud fraction in 0.10 increments. The pixels associated with each data point are then binned by the TAU categories in Chapter 4. The quantities are normalized and the resulting distribution mirrors (or implies) the liquid water distribution for a particular scene over an entire month.

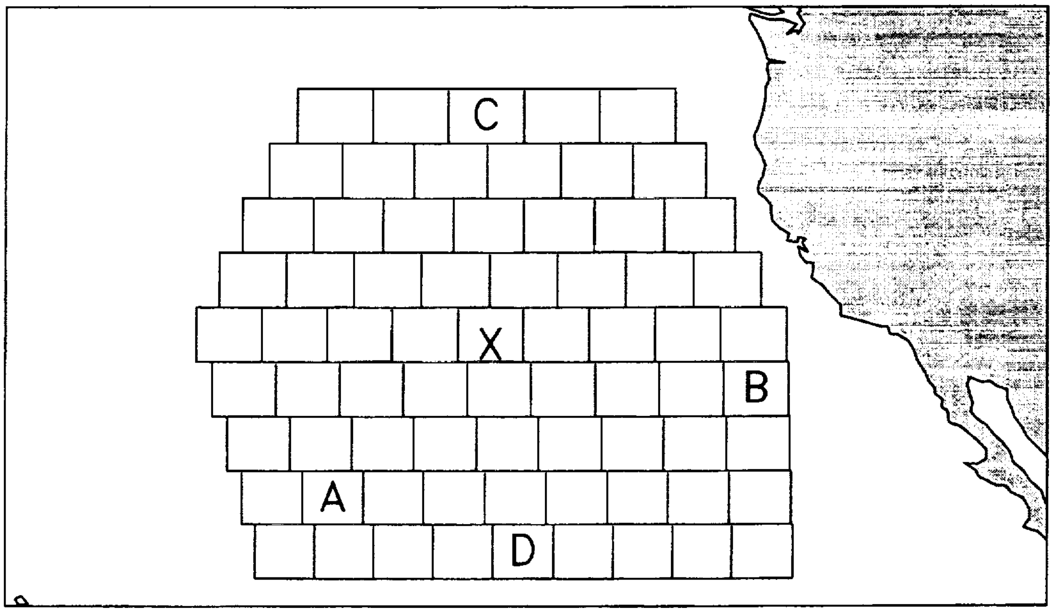

Figure 5.1 Location of EQUAL-AREA grid boxes for spatial averaging in the stratus area domain (22.5° N to 45°N and 125°W to 150°W).

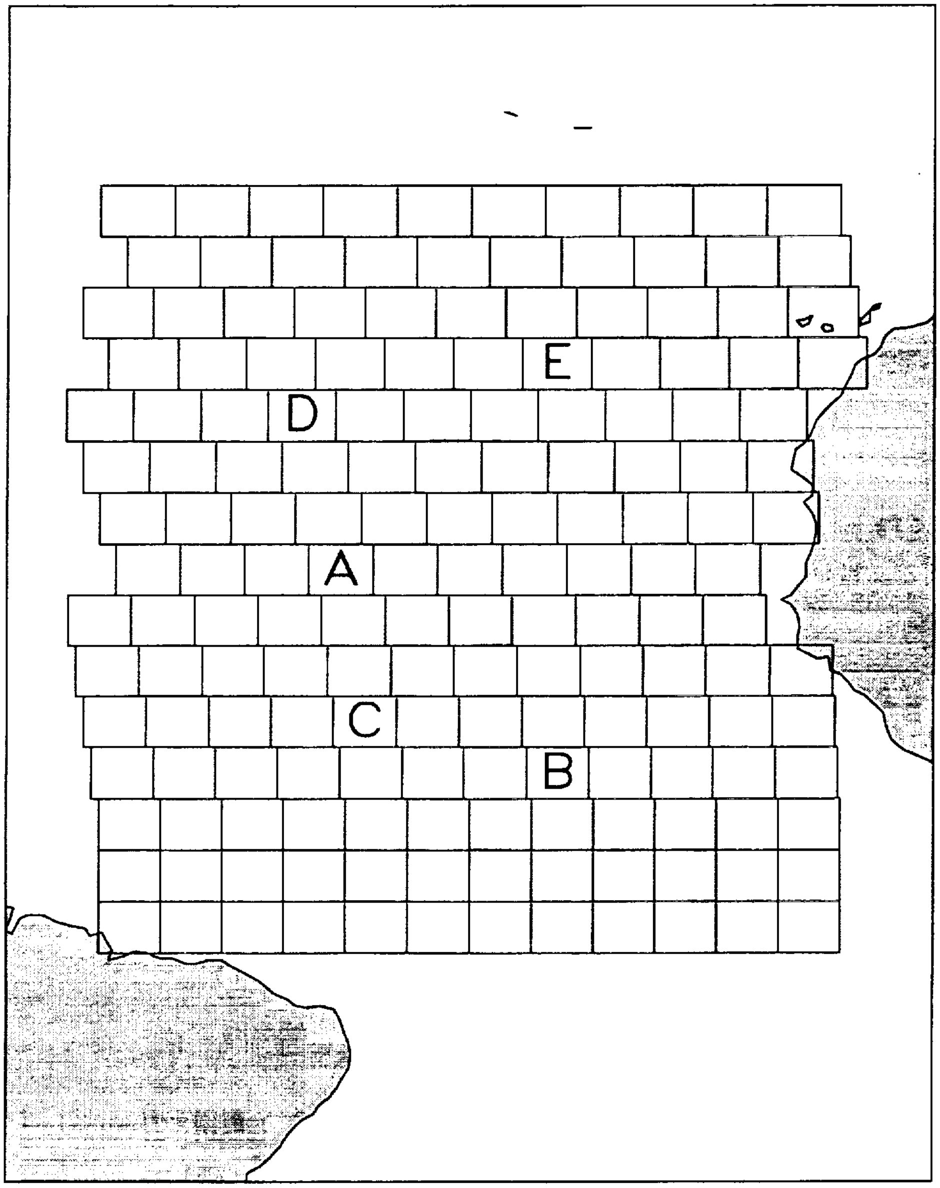

Figure 5.2 Location of EQUAL-AREA grid boxes for spatial averaging in the tropical area domain (2.5° S to 35°N and 15°W to 45°W).

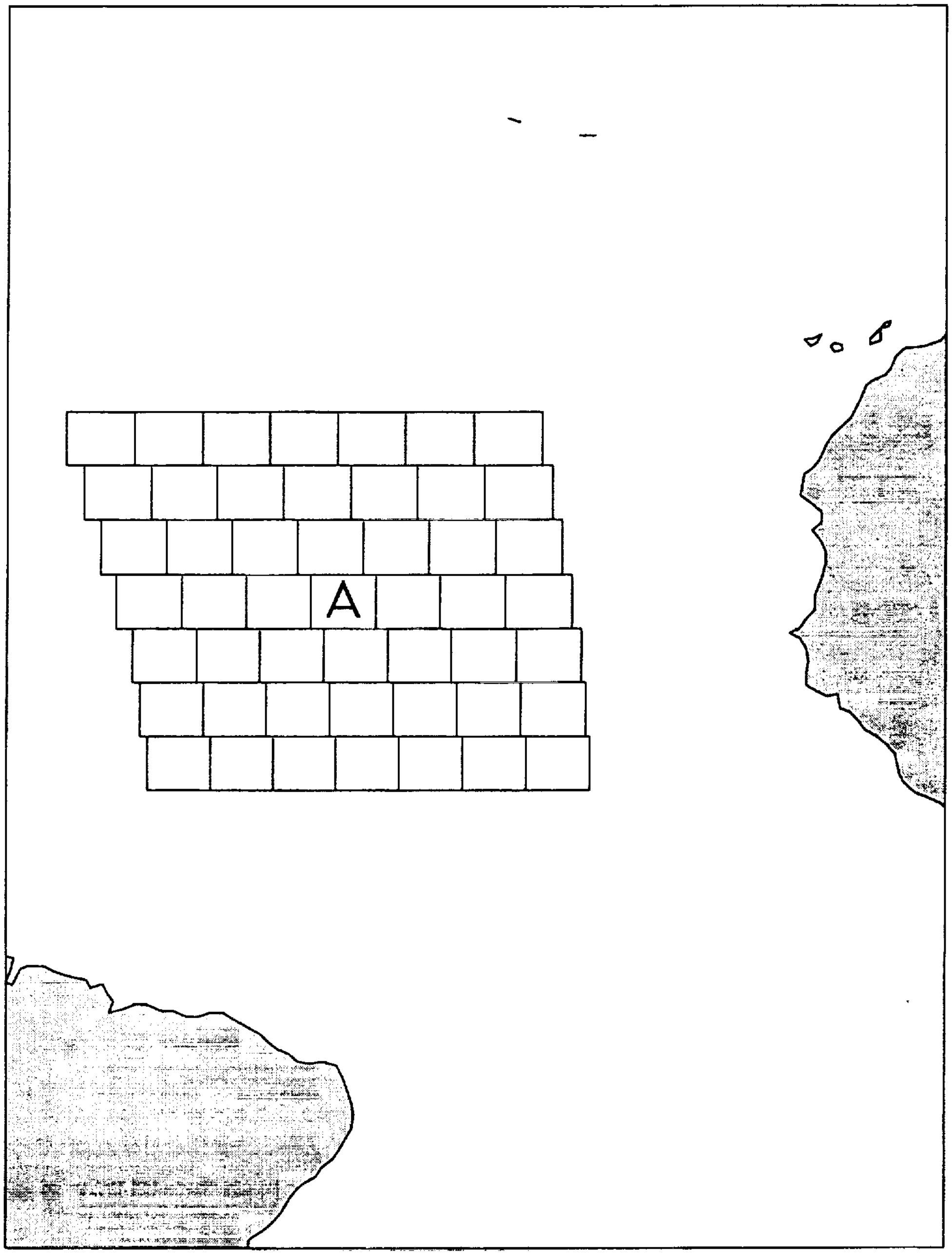

Figure 5.3 Tropical area 1 (7.5° N to 25°N and 25°W to 45°W).

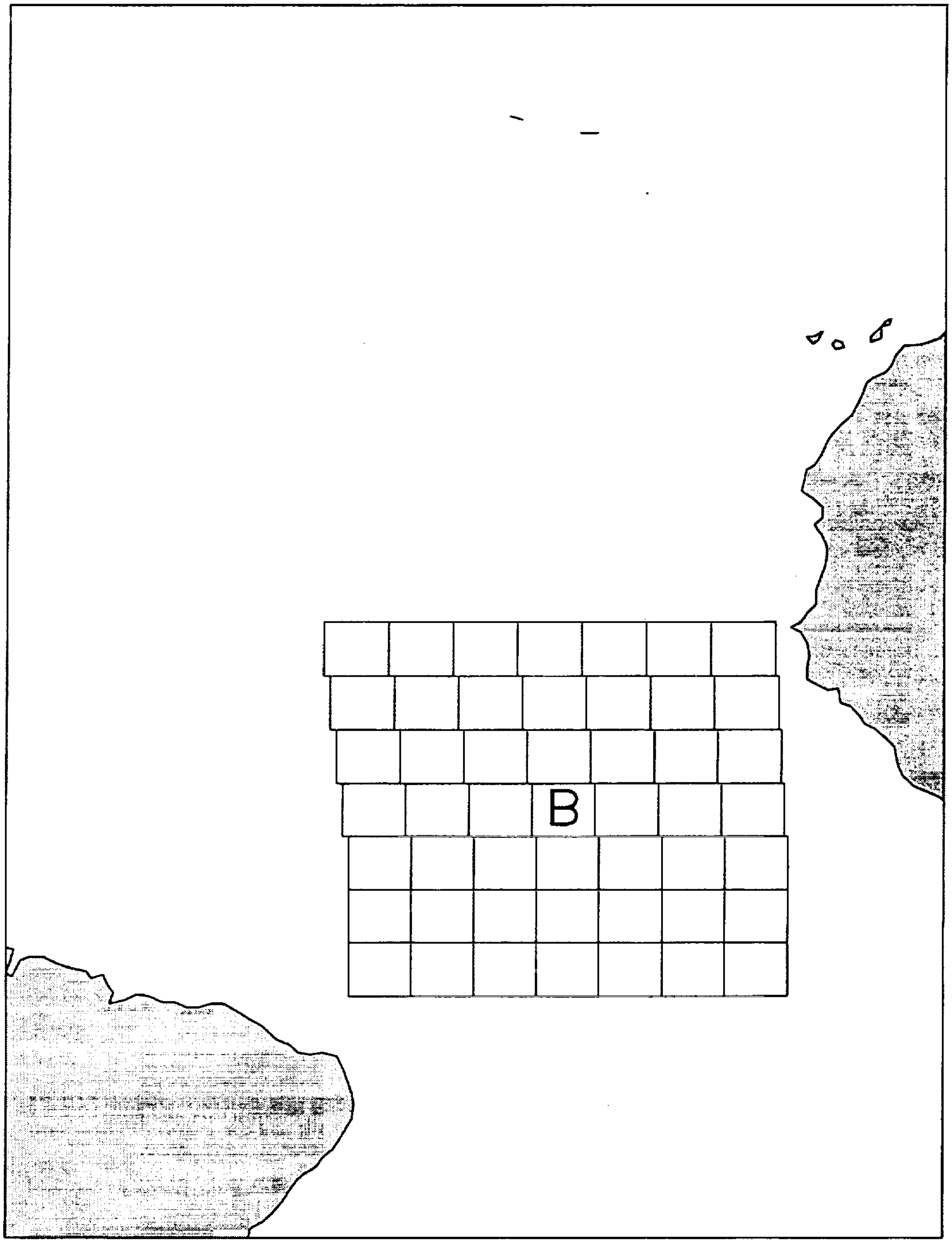

Figure 5.4 Tropical area 2 (2.5° S to 15°N and 15°W to 35°W).

6. SPATIAL AVERAGE VERSUS TIME AVERAGE

In both the two following chapters, only spatial averaging results are presented. There are three reasons why no time averaging results were computed. First, since the number of visible cloudy pixels is used to calculate the cloud fraction and the number of TAU visible/infrared pixels is determined by a "daytime" algorithm, a method is needed to infer the number of "visible" pixels during the nighttime hours.

In order to obtain an appropriate diurnal cycle, the number of visible pixels could be interpolated over the nighttime hours. Rossow et al. (1988) linearly interpolate over the number of IR only and VIS/IR pixels from dusk to dawn. Then the nighttime visible pixel quantity is obtained by adding the interpolated difference between VIS/IR and IR only to the IR only value. The value for mean cloud optical depth, TAU, is also interpolated over the nighttime period between dusk and dawn. While such a method seems appropriate for monthly averaging, it appears too crude for investigating a diurnal cycle.

Another weakness arises in attempting to apply Rossow's procedure. Typically, during the day, the number of infrared cloudy pixels may be substantially less than the number of visible cloudy pixels. This scenario occurs when broken low-level clouds have approximately the same cloud top temperature as the background ocean surface. For the marine stratocumulus layers under study here, this problem intensifies during a strong inversion when the cloud top temperature may actually be warmer than the sea surface. The resulting cloud would be non-existent in the infrared. Even cloud properties in low latitudes suffer problems by Rossow's visible adjustment. The mean optical depth, TAU, is underestimated. For both the tropical and marine stratocumulus regions, the adjustments may be off by as much as 13%. Thus, using the number of infrared cloud pixels alone or Rossow's interpolation scheme to determine a diurnal cloud fraction relationship is risky.

A second reason favoring spatial averaging is the resulting number of data points. For any particular box over an entire month, a daily time average yields 30 data points while a spatial average yields as many as 120 points. When two boxes are considered together, the number of data points changes to 60 and 120, respectively. Now the question arises as to the independence of the data points in time and space.

To examine this factor, Figures 6.1 through 6.4 illustrate cloud fraction versus mean cloudy spherical albedo for four different box locations during July 1987. Figures 6.1 and 6.2 are representative of the stratus area, while Figures 6.3 and 6.4 are representative of the tropical region. The individual letters correspond to days of the month with A representing all scenes on July 1st and B representing all scenes on July 2nd. The numbers, 1 through 5 correspond to July 27th through July 31st. For the present, ignore the trend and interpretation of the data, and look only at the data points for a particular day on an individual basis.

For both the stratus box B, Figure 6.2, and the tropical box of Figure 6.3, it is observed that a cloud fraction of greater than 90 to 95% remains 90 to 95% for all scenes on a particular day. Figures 6.5 through 6.7 illustrate this more clearly. The figures are the same graph as Figure 6.3 except that the data is at one satellite viewing hour for the entire month. For July 3rd (letter C), 7th (letter G), and 20th (letter T), the cloud fraction remains at 100% from 1200 UTC to 1800 UTC. On the other hand, an individual day like

July 10th (letter J) has a cloud fraction range from 20 to 80% over the same time period. For scenes with a cloud fraction less than 10%, the tendency is for the day to retain a low cloud fraction. This is clearly depicted for the marine stratocumulus box in Figure 6.1 on July 22nd (letter V) and July 30th (number 4). From these observations, the satellite scenes of any particular day exhibit cloud fractions over the range of 10% to 90%, unless the extremes, cloud fractions less than 10% or cloud fractions greater than 90%, are observed. Therefore, a scene is generally time independent. This provides a third impetus for presenting only a spatial average.

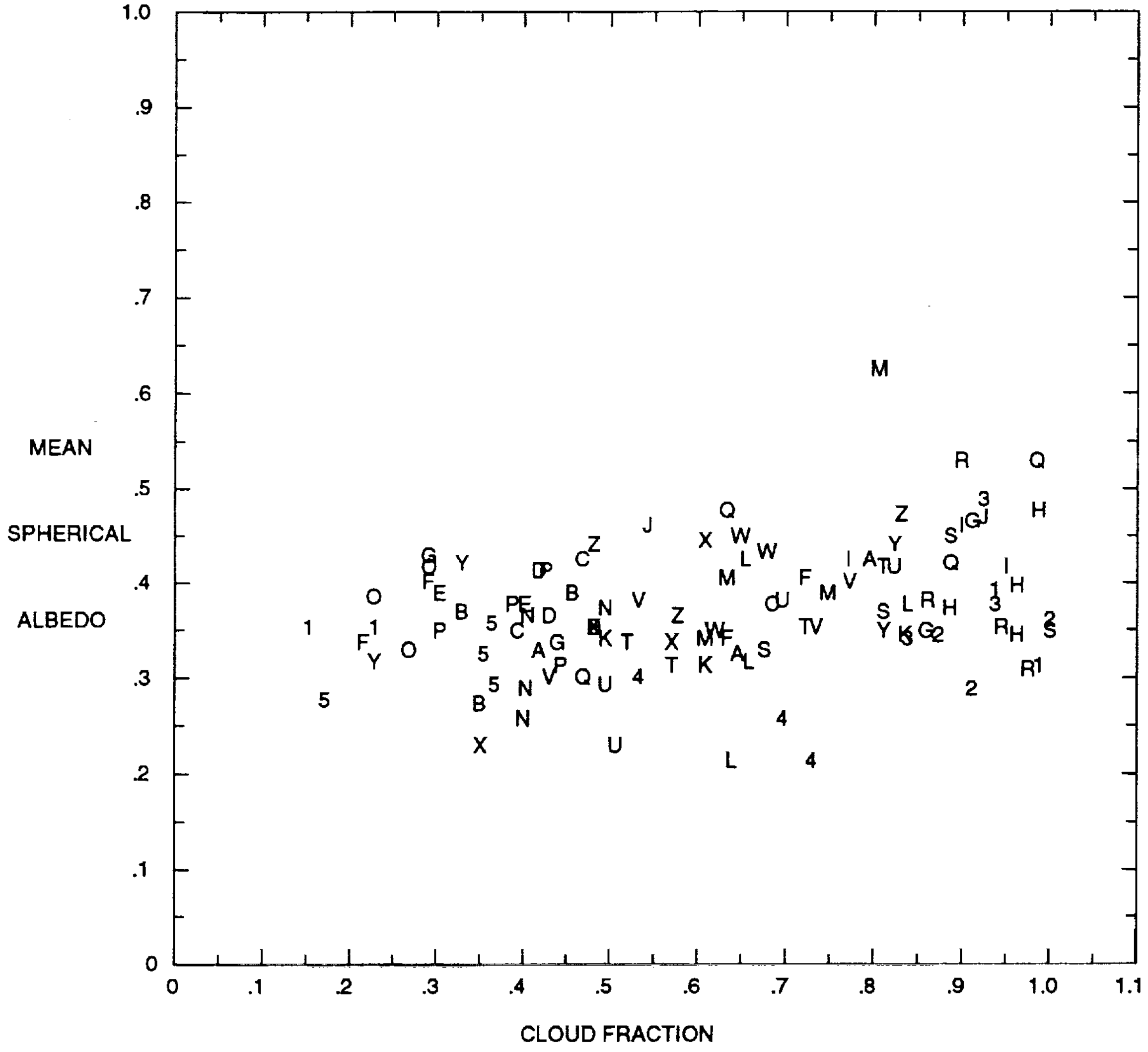

Figure 6.1 Mean spherical albedo versus cloud fraction for stratus box A, July 1987.

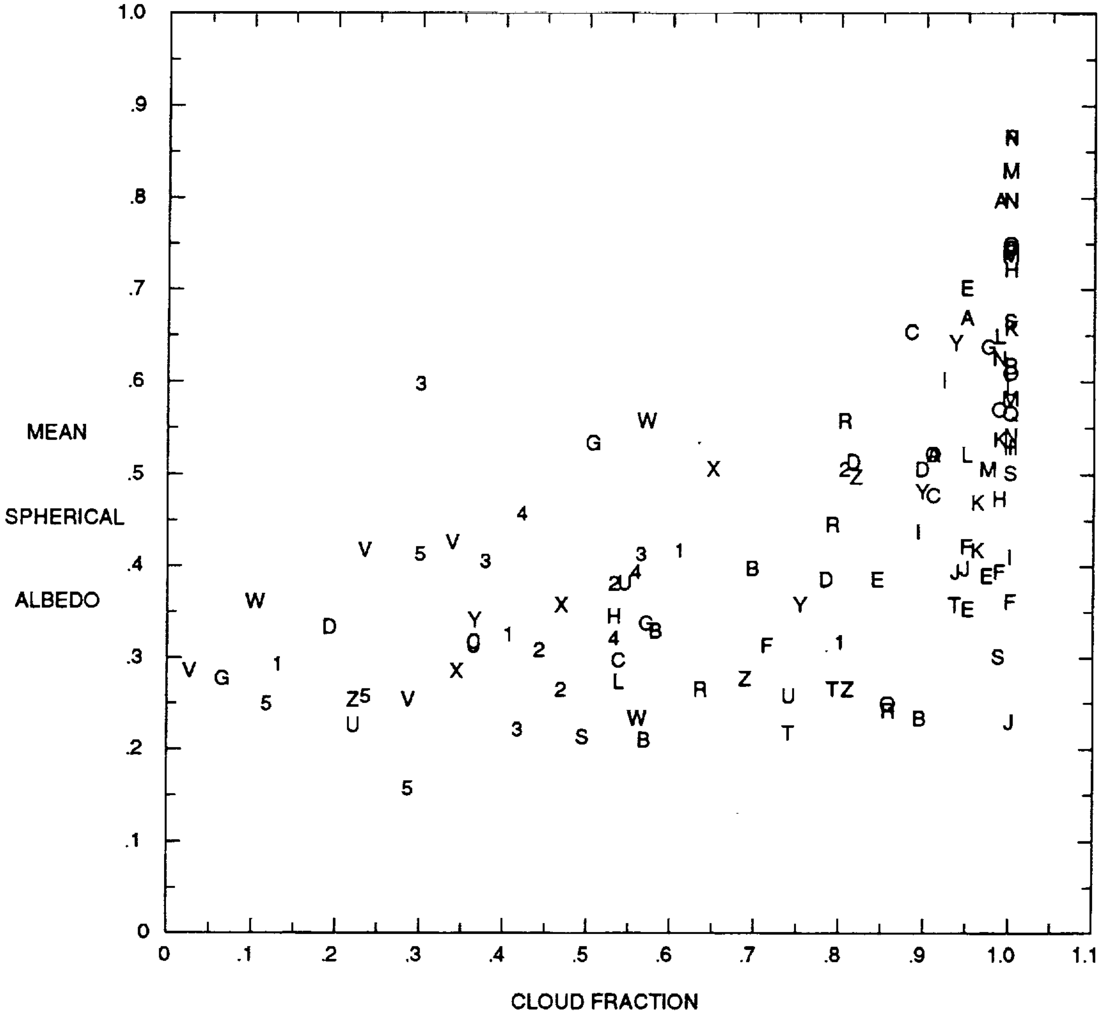

Figure 6.2 Mean spherical albedo versus cloud fraction for stratus box B, July 1987.

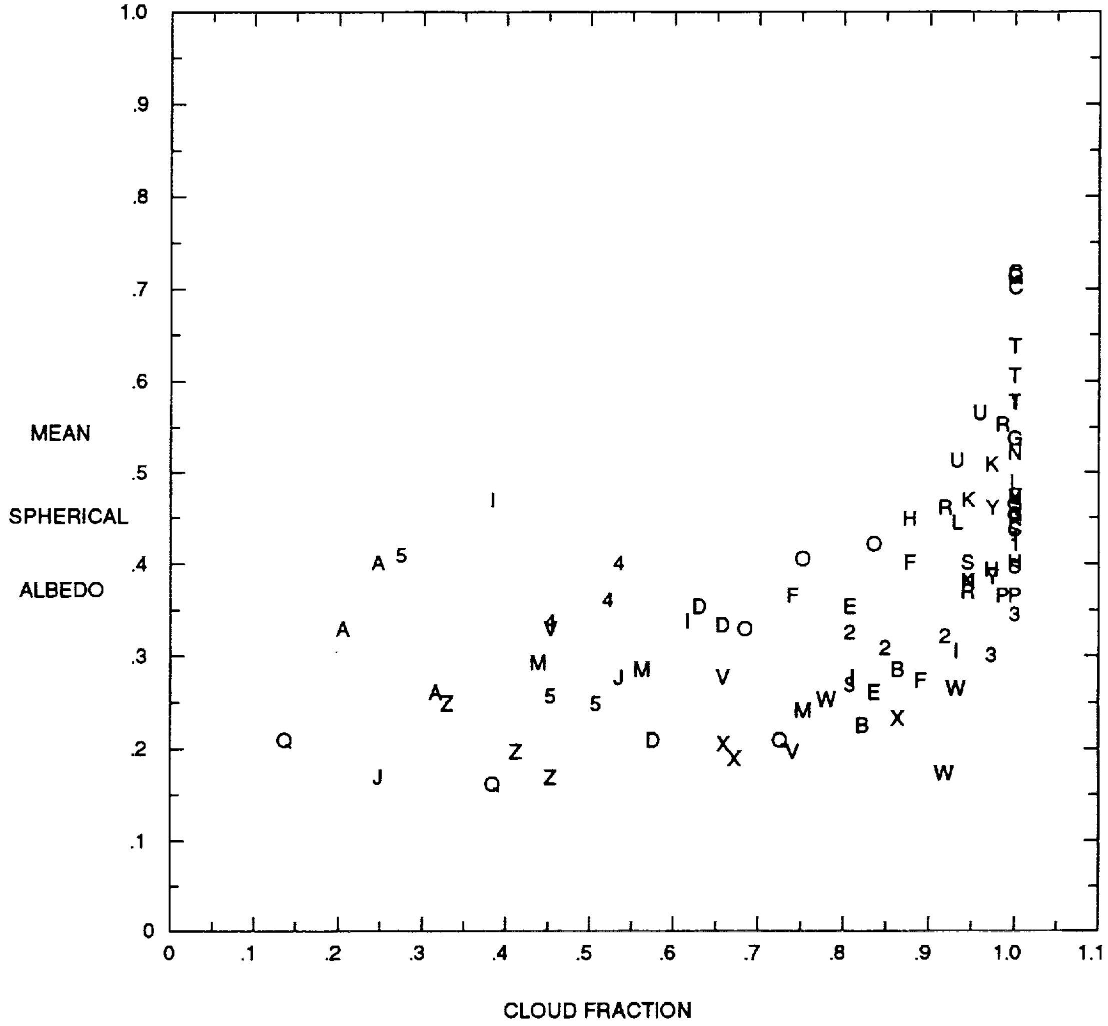

Figure 6.3 July 1987 mean spherical albedo versus cloud fraction for the first tropical box located at 5° N to 7.5° N and 98° W to 100.5° W. The box is four boxes west of box B and directly southwest of box C.

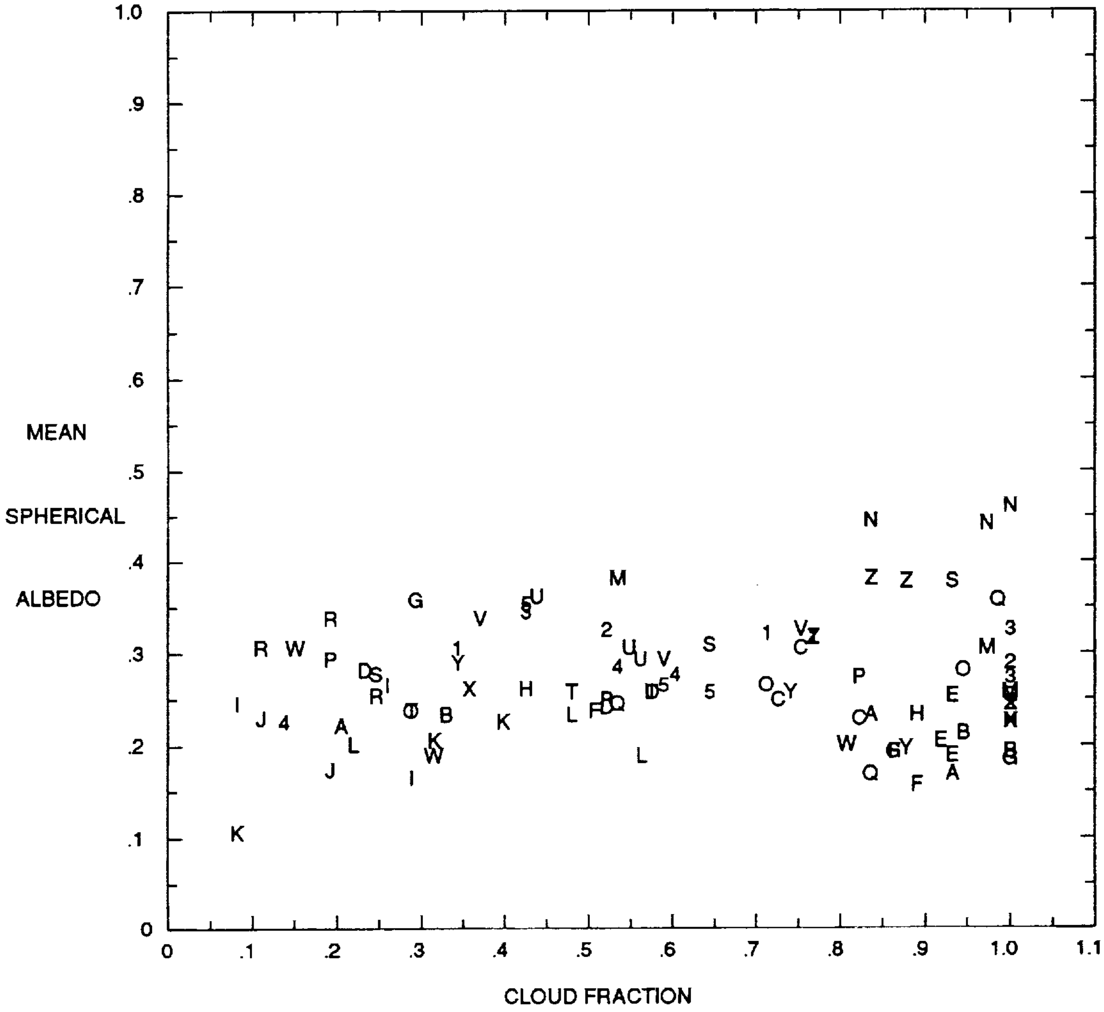

Figure 6.4 Mean spherical albedo versus cloud fraction for tropical box A, July 1987.

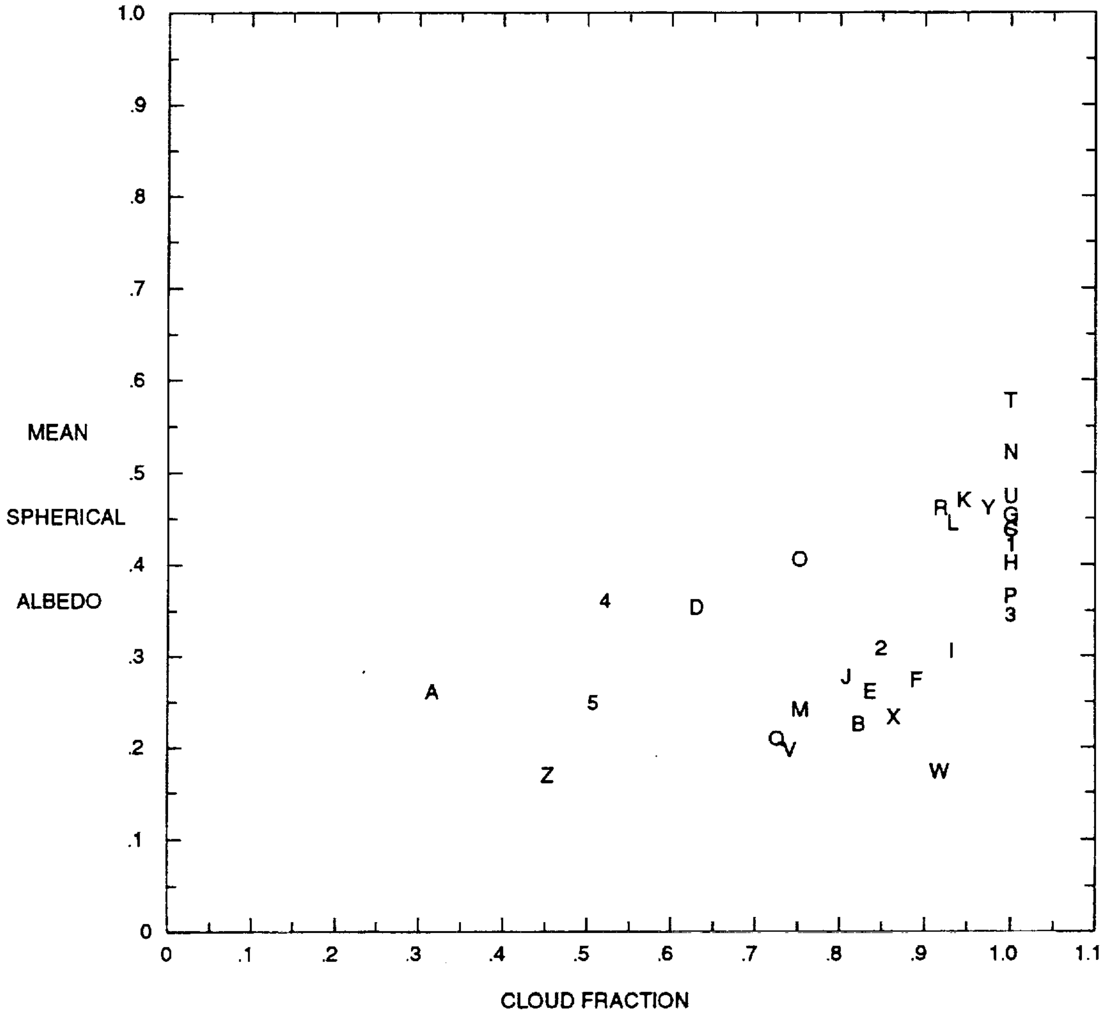

Figure 6.5 Mean spherical albedo versus cloud fraction for the first tropical box, July 1987 at 1200 UTC.

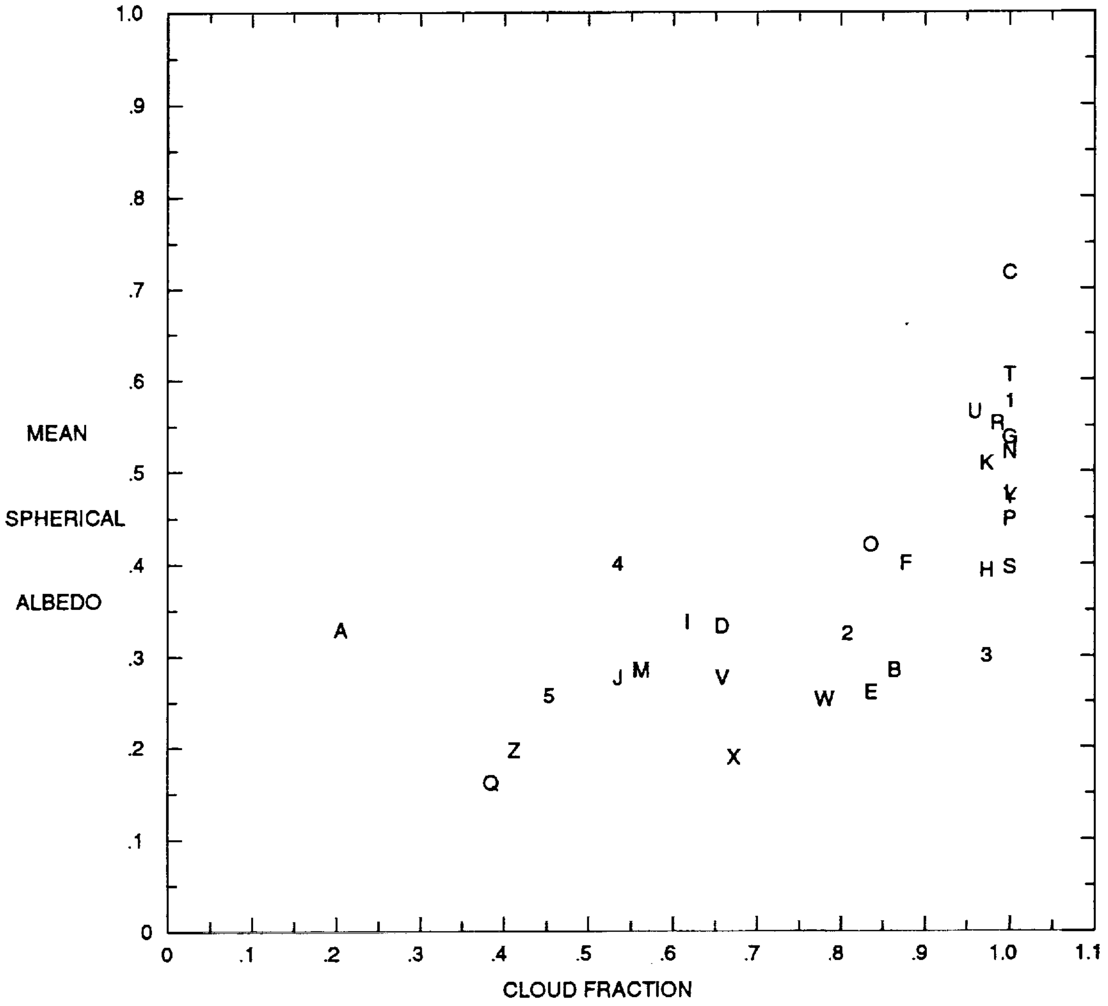

Figure 6.6 Mean spherical albedo versus cloud fraction for the first tropical box, July 1987 at 1500 UTC.

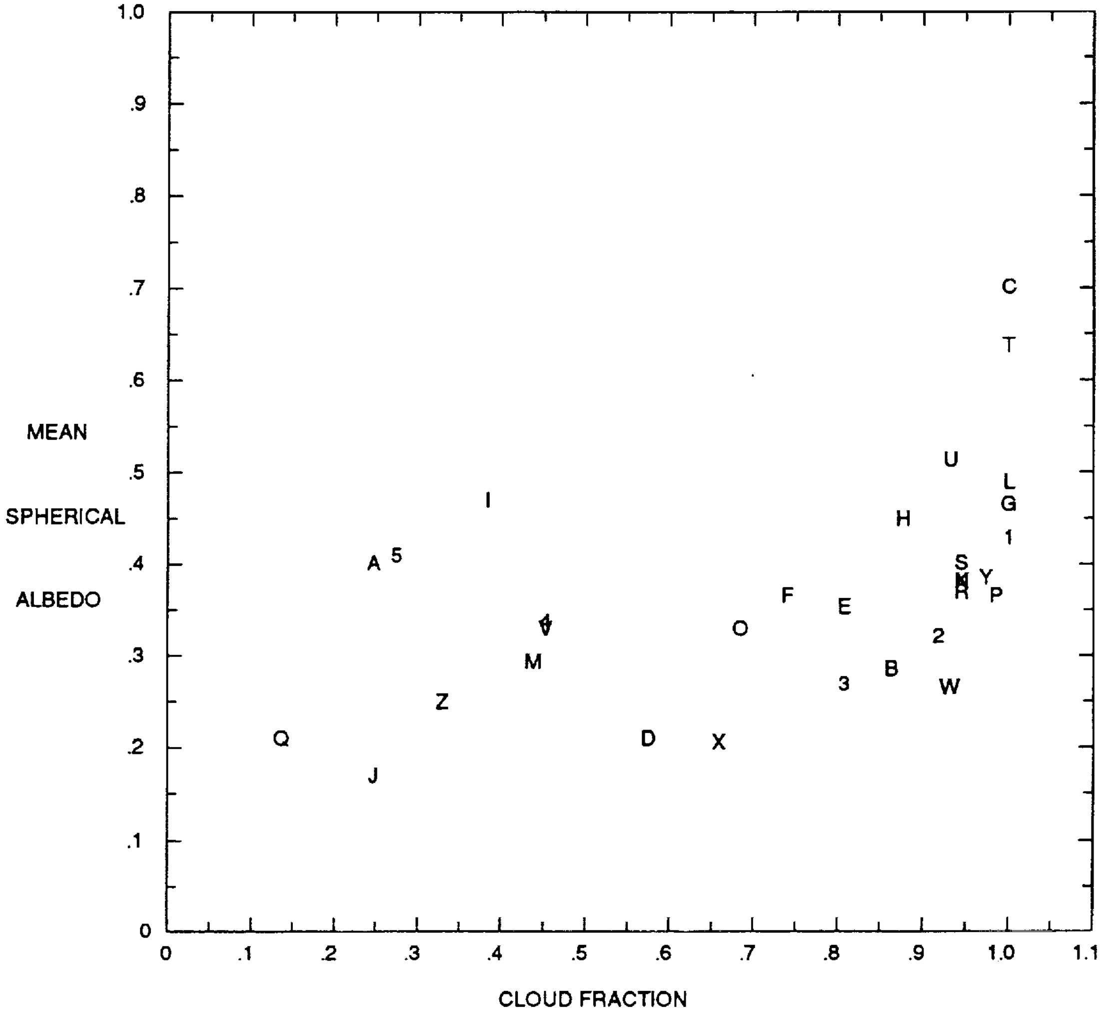

Figure 6.7 Mean spherical albedo versus cloud fraction for the first tropical box, July 1987 at 1800 UTC.

7. MARINE STRATOCUMULUS RESULTS AND DISCUSSION

The following results are discussed in terms of the cloudy mean spherical albedo. For completeness, the grid mean albedos for July 1987 and 1988 are provided by the ERBE scanner data in Figures 7.1 and 7.2. As a formal definition, cloudy albedo is defined as:

$$\sum_{\text{gridbox}} \frac{E_{\text{reflec}}(x,y)}{E_{\text{incident}}(x,y)} \delta(x,y), \text{ where } \delta = \begin{cases} 1 \text{ cloudy} \\ 0 \text{ clear} \end{cases} \tag{4}$$

The grid mean albedo is defined in the same manner except that δ is equal to one for both clear and cloudy conditions. As expected, higher grid box albedos are in the northwest quadrant (40° to 45° N) of the study area and are associated with the north Pacific storm track. The southeast quadrant (125° to 135° W, 22.5° to 30° N) is the dominant marine stratocumulus region. The southwest quadrant is a the transition zone to a broken cumulus layer.

The spatial averaging of the ISCCP data initiates with box X and extends outward in five concentric rings. After spatial averages are presented, probability distribution functions, PDF, for the mean optical depth, TAU, provide insight concerning the liquid water path, LWP, interpretations.

Spatial Averages

To put the spatial averaging into perspective, we first examine a few individual boxes in the region. On Figure 7.1, these boxes are labeled A, B, and X. Box A is identical to box A from Harshvardhan et al. (1993) while box B is similar to Harshvardhan's box B except that it is the next box west. Visible satellite imagery (Kloesel et al. 1988) guided the selection of boxes A and B. All boxes contain over 100 individual time periods or scenes. Box A is at the edge of the stratus region with broken clouds and partly cloudy conditions prevailing throughout the month while box B is partly cloudy or completely overcast during this period. However, box B contains one clear period. Box X is approximately in the center of the stratus area with an extensive layer of clouds on some days and broken clouds on other days. Broken cloudiness is not as prevalent as in box A.

Mean Cloudy Albedo Versus Grid Box Albedo

Since the following results display mean cloudy albedo versus cloud fraction, an idealized plot of cloudy albedo versus cloud fraction over a black surface is depicted in Figure 7.3 for reference. The initial rise in slope represents the transition from thin clouds (optical depth < 1.0) to some medium thickness (1.0 < optical depth < 25.0) appropriate for synoptic conditions. The horizontal portion with constant albedo illustrates that clouds of the same optical thickness are present. The increasing cloud fraction means there is a progressively larger percentage of the box covered with clouds with the same optical thickness. Once the cloud fraction reaches 100%, it can no longer increase. However, optical thickness can continue to increase, causing further increases in albedo. Ordinarily, for GCM calculations, the cloudy albedo is not a known quantity. Rather, it is the grid box or net albedo including both clear and cloudy albedos that is known.

Also for reference, Figure 7.4 displays an idealized plot of grid box albedo versus cloud fraction over a black surface. There is a constant rise in slope for this scenario. As clouds continue to form or grow, the optical thickness may or may not increase. Since the clouds now occupy once clear areas, the grid box albedo must increase. As in the mean cloudy albedo graph, once the cloud fraction reaches 100%, only the albedo can increase.

Individual Boxes

July 1987

The mean cloudy albedo plot for box A, Figure 7.5, shows that an increase in cloud fraction does not correspond to a substantial change in the range (0.20 to 0.45) of albedo values. The mean reflectance is independent of the cloud fraction. This plot corresponds to the horizontal position of the idealized cloudy albedo versus cloud fraction graph in Figure 7.3. Only clouds of similar optical thickness are present and increasing in areal coverage. However, there would be an increase in the grid box albedo. By using the above information and modeling box A, a cloud fraction of 40% yields a mean reflectance of approximately 0.35. A cloud fraction of 80% again yields a 0.35 reflectance. With the same albedo, both cases have the same optical thickness, TAU, and hence the same LWP for identical drop distributions. Therefore, the grid box total liquid volume for 80% cloud fraction is twice that for 40% cloud fraction. This is a consequence of LWP being independent of cloud fraction.

Turning to box B in Figure 7.6, the trend is slightly different. The lower albedo values represent clear or partly cloudy conditions while the higher albedos corresponding to the middle of the month, letters J through Q, have cloud fractions generally greater than

90%. The horizontal and vertical characteristics of Figure 7.3 are displayed in box B. Similarly to box A, box B albedos are independent of cloud fraction for cloud fractions less than 85%. For cloud fractions greater than 85%, the optical depth and hence cloudy albedo increase.

It is a little more difficult to determine the relationship for albedo and cloud fraction in box X, Figure 7.7. The range of albedo values between 10% and 95% cloud fraction is relatively wide at 0.4. Thus, only the vertical portion of Figure 7.3 is clearly defined at approximately 95% cloud fraction for box X.

July 1988

While the three boxes detailed above are for July 1987, the same three boxes for July 1988 show similar characteristics especially boxes A and B (figures not shown). The 1988 box A has a slightly wider spread of albedo values going, from 0.20 to 0.60, rather than 0.20 to 0.45. Both the 1987 and 1988 box B are very similar except that the 1988 box has more completely overcast scenes. For box X, the 1988 box has only seven completely overcast scenes while the 1987 box has twenty overcast scenes. Essentially, the 1988 box X illustrates all three parts of the mean cloudy albedo graph of Figure 7.3 while the 1987 version depicted only the vertical portion.

Interpretation of Boxes A and B

Another way to visualize the results of boxes A and B is to borrow an idea from Coakley (1991), (see Figure 1.2). For cloud fractions between 20% and 80%, the box contains small clouds with 1 km cores of high liquid water concentration and large droplets. Surrounding the cores are edges about 100 m wide with low liquid water concentrations and small droplets. The higher the cloud fraction, the greater the number of cores. For cloud fractions greater than 80%, the clouds become packed together and start to form uniform layers comprised of these cores and edges. These scenes, in general, contain thicker clouds. Coakley used 0.63 μm and 3.7 μm reflectance to infer liquid water amounts and droplet size. The above ISCCP results suggest albedo is independent of cloud fractions for cloud fractions 20% to 80%, thus implying liquid water amount as the more critical variable.

Box Groups

July 1987

The spatial average for groups of boxes is the next step performed. Figures 7.8 through 7.11 are for July 1987. Figure 7.8 illustrates the first ring average around box X (box X inclusive). This average includes 8 boxes with 102 time periods none of which are clear. The graph indicates that both the cloud fraction and the albedo range decreases in comparison to the single box X. The average has not incorporated the edges of the stratus region or the near coastal marine stratocumulus. Figure 7.9 depicts the second ring spatial average around box X. For this graph, the number of data points drops 20% to 81 realizations due to considerable missing data. Any missing data within a particular box causes the entire scene for all boxes to be discarded. This average begins to incorporate the edge of the stratus region, coastal marine stratocumulus and the southern boundary of the Pacific storm track. These features combined with the areal extent of the average further condenses the cloud fraction range to between 50% and 100%. By the third ring,

Figure 7.10, an almost linear relationship between cloud fraction and cloudy albedo is discernible, but it flattens out between 50% and 60% cloud fraction. One more step in the averaging process, Figure 7.11 defines this linear relationship more clearly by the following regression line,

$$\mathrm{ALB} = 0.295\ \mathrm{CF} + 0.207, \tag{5}$$

where ALB equals the albedo value and CF is the cloud fraction . The fact that this line fails to pass through the point (0,0) indicates it is only valid for cloud fractions between 55% and 100%.

There are two reasons for this limited range and the observed slope across it. First, as a more extensive area of the stratus region is included in the average, the likelihood of clear or partly cloudy (cloud fractions less than 50%) scenes is greatly reduced. Therefore, spatial averages across a marine stratocumulus regime rarely depict scenes with a cloud fraction of 50% or less. Secondly, the spatially averaged plot of cloudy albedo has a similar appearance to that of the one box grid mean albedo of Figure 7.4. However, the two linear dependencies are distinctly different. As the regional cloud fraction increases, the number of completely saturated scenes increases as more boxes are included in the spatial average. This means individual boxes scenes with high cloud fractions and high albedo values are averaged with other individual boxes with high cloud fractions and high albedos.

For example, consider an average consisting of four boxes with cloud fractions of 50%, 40%, 60% and 50%. From the idealized scenario of Figure 7.3 and the results of boxes A, B and X, (Figures 7.5, 7.6, and 7.7), albedo tends to be independent of cloud fraction over a range of 20% to 90% cloud fraction. So for this example, let the albedo value be 0.35 for each box. The average cloud fraction is 50%, while the average albedo is 0.35. Compare this result to four boxes that have cloud fractions of 100%, 100%, 80% and 70%. From Figure 7.3, a cloud fraction of 100% may have a variety of albedo values associated with it. So let the respective albedo values be 0.80, 0.60, 0.35 and 0.35. The average cloud fraction is 87.5%, while the average albedo is 0.53. Therefore, the observed slope in the spatial averages is a result of numerous completely overcast scenes. On the other hand, the slope of the grid box albedo is caused when clear scenes are incorporated into the average. That is, for two boxes with identical clear properties and identical cloudy properties, albedo will higher for the box with a greater cloud fraction.

Furthermore, it can be stated that Coakley's theory does not apply to the spatial averages around box X. For his theory, albedos are independent of cloud fraction. Since the spatial averages include completely overcast scenes where the albedos are not independent of cloud fraction, Coakley's theory of large and small clouds fails. Further averaging does not change the range of cloud fraction or albedo values. Thus, the stratus area as an ensemble is well represented by equation (5). By comparing the three individual boxes discussed previously with the end result of the spatial average, it is clear that a GCM must account for the areal extent over which it resolves clouds and determines cloud fraction in order to model clouds appropriately (Xu and Randall 1992). Since this spatial average is equivalent to a low resolution GCM model grid, again cloud fractions less than 50% rarely occur.

July 1988

Figures 7.12 through 7.15 detail box X and the spatial averages for July 1988. As mentioned previously, the 1988 box X is different than the 1987 version in that there is a greater number of partly cloudy (cloud fractions less than 50%) scenes and the highest albedo value occurs at a cloud fraction of 90% rather than 100%. The 1988 box X generally has thicker clouds when the cloud fraction is over 80%. The cloud fractions in box X tend to fall within three clusters, low cloud fractions, (< 30%), middle cloud fractions, (30% to 60%), and higher cloud fractions, (60% to 100%). These three groups are more apparent in the first ring average, Figure 7.13. The albedo now has a range of only 0.20 to 0.50 for all cloud fractions. There is a slight linear trend (slope < 0.5) for this level of spatial averaging. However, it is not as strong as 1987, Figure 7.8, where a trend forms at the higher cloud fractions. The two low cloud fraction groups collapse into one group by the second level average, Figure 7.14, but the trend is still different as compared to 1987, Figure 7.9. There are no completely overcast scenes and the linear relationship for the second ring has a slope of .091 for 1988 in comparison to 0.316 for 1987. Jumping ahead to the fourth level average, Figure 7.15, both 1987 and 1988 cover approximately the same albedo range, but 1988 depicts a different trend as indicated by the following regression line:

$$\mathrm{ALB} = 0.121\ \mathrm{CF} + 0.352. \qquad (6)$$

Although the slopes and intercept values are different for both years, the range of cloud fraction and albedo values over which both lines are valid is approximately the same, 55% to 100% cloud fraction. In order to determine which regression is more appropriate, the fourth level average for 1986 is presented in Figure 7.16. The regression line is:

$$\mathrm{ALB} = 0.205\ \mathrm{CF} + 0.232 \qquad (7)$$

The 1986 line matches the 1987 results better than the 1988 regression. The reason for this will be apparent upon evaluating the probability distribution functions described in the next section. Examining a greater number of years would also confirm whether the 1987 or 1988 regression is more representative of the stratus regime.

Probability Distribution Functions

In order to gain insight about the liquid water path distribution, the number of pixels within the different mean TAU categories mentioned in Chapter 4 is determined for every tenth of a cloud fraction. This TAU value represents contributions from cloudy areas only. Figure 7.17 depicts the result for box X. Since a higher cloud fraction means there are a greater number of cloudy pixels, it is only natural that this graph is skewed towards the higher cloud fractions. The skewness towards the center TAU category, 3.55 to 9.38, is indicative of the cloud type and liquid water distribution that is discussed in later sections. Besides the skewness towards higher cloud fractions, the total number of cloudy pixels over an entire month is variable. Therefore, in order to compare individual boxes and spatial regions, two methods for normalizing the number of pixels are presented.

Normalization Procedures

The first normalization procedure involves taking the number of pixels in each TAU-cloud fraction square and dividing by the total number of pixels in all 50 TAU-cloud fraction categories. The base ten logarithm is then taken for improved visualization of the data. By this normalization process, the sum of all 50 bars equals one. Figure 7.18 displays the results for the July 1987 box X in the center of the stratus region. The height of the bars indicates the probability of occurrences of a particular cloud fraction and TAU category. Since this method of normalization does not allow for the cloud fraction category to be independent, the influence of the higher cloud fractions is still clearly visible. This type of graph is convenient for comparing many boxes to each other because it normalizes across both cloud fraction and TAU. Thus, for box A at the western edge of the stratus region, it is expected that the height of the bars will shift towards lower cloud fractions and lower TAU categories. Figure 7.19 depicts the above phenomenon for box A, July 1987. For both box X and A , the middle TAU category is the most probable. However, for modeling purposes, it is easier to treat cloud fraction as an independent quantity.

The second normalization procedure treats the cloud fraction groups as independent by taking the number of pixels in each TAU-cloud fraction category and dividing by the total number of pixels within a particular cloud fraction division. The sum of the bars within a cloud fraction category equals one. Fig 7.20 displays the results for box X. For cloud fractions less than 10%, the probability is zero; likewise the three TAU categories between 10% and 20% and the two TAU categories between 20% and 30% are also zero probability. Looking at the 20% cloud fraction division and the 9.38 to 22.63 TAU category, the probability is 0.87, much greater than the 0.000948 when compared against all cloud fractions in Figure 7.18.

Individual Boxes

For box A on the edge of the stratus, Figure 7.21, the distribution tends to cluster around the middle TAU category mentioned above. This confirms Coakley's model mentioned earlier for explaining the cloudy albedo results of Figure 7.5. Here, it is the mean TAU value that is independent of cloud fraction and hence is given by the following relationship

$$\mathrm{LWP} = \frac{2}{3}\tau r_e, \qquad (8)$$

where LWP equals liquid water path, τ equals mean cloudy optical depth, and r_e equals the effective particle radius (Stephens 1984; Harshvardhan et al. 1993). The LWP is independent of cloud fraction.

The result for box B on the eastern side of the stratus area, Figure 7.22, displays a bimodal peak. Lower cloud fractions tend to have thinner clouds, while higher cloud fractions have thicker clouds. Thus, Coakley's model is not as applicable to box B. This coincides with findings from the spatial averaging section.

For the year 1988, boxes X, A, and B, have less identifiable features. Box X, Figure 7.23, tends to have thinner clouds dominating the scene. As in 1987, the 1988 box A (figure not shown) clusters towards the center TAU category for cloud fractions 30% to 90%. Again, Coakley's model seems to fit well for this box A. The results for the 1988 box B (figure not shown) are highly variable with no discernible trend.

Before discussing the impacts of the above observations, two other boxes are examined to determine the distribution from north to south. Box C is on the northern edge of the stratus region and the southern edge of the north Pacific storm track. Box D covers the southern edge of the stratus region where the cloud type is transitory in nature, changing from layer stratus to broken stratus to broken cumulus elements during the month. Because of box C's location, Figure 7.24, higher cloud fractions dominate for 1987. The noticeable spike between 20% and 30% cloud fraction is associated with one scene of thick clouds. The other cloud fractions below 60% indicate zero probability because all scenes are completely overcast or the three-hour time sampling did not capture any broken cloudiness. Also, at least one out of four possible scenes tended to be missing each day for this box. Thus, when the box may have had less cloud coverage for brief periods of time, it is rarely seen by the satellite. As with boxes A, B, and X, TAU values of 3.55 to 9.38 are the most prevalent. Figure 7.25 displays box D. For all five locations, partly cloudy (cloud fraction < 50%) scenes have varying optical thicknesses while higher cloud fractions have a consistent distribution of optical thickness with the same probability. Discount the lowest cloud fraction category because only one scene is represented.

The same two boxes for 1988 are displayed in Figures 7.26 and 7.27. Generally, the 1988 box C, Figure 7.26, looks like the 1987 box D, Figure 7.27, while the 1988 box D looks like the 1987 box C. One probable cause is a northward shift of the Pacific subtropical high pressure cell and a shift northward of the Pacific convection. Thus, while the 1988 box D looks like the 1987 box C, the forces creating each distribution are different. This observation helps to explain the differences found earlier in the 1987 and 1988 regression lines for spatial averages over the entire stratus region. Clustering towards the middle TAU category is still apparent.

Discussion

It is clear from the individual boxes of albedo versus cloud fraction graphs that for low-level single layer clouds mean cloudy albedo is invariant for cloud fractions of 20% to 80% or 90%. Since the mean cloudy albedo is a measure of the optical depth, the mean liquid water path for cloudy areas is also independent of cloud fraction according to equation (8). Therefore, the total volume of liquid in a box is a linear function of cloud fraction. Xu and Randall (1992) observed this relationship in a two dimensional cumulus ensemble model for the lowest model layer.

An important outcome of the above information is its applicability to cloud parameterizations following a scheme used in the modeling of surface hydrology in a

GCM (Harshvardhan et al. 1993). The problems involved with the parameterization of cloud radiative properties in a GCM parallel some the problems in parameterizing surface hydrology. Diagnostic or prognostic variables in GCMs are defined for the entire grid box which may be 100 km on a side. Thus, the liquid water amount or precipitation rate computed at any time step is an average value over the entire grid box. As Harshvardhan and Randall (1985) have pointed out, the radiative properties of a grid box, such as albedo and emittance, depend on the distribution of the liquid water path, not just on the area averaged value. Similarly, the precipitation rate for a grid box also depends on the local precipitation rate. Interception, infiltration and run-off are all non-linear functions of this local rate (Entekhabi and Eagleson, 1989). Thus, a first-order approximation to the subgrid scale variability is obtained by estimating the cloud fraction (wetted area for rainfall) and mean cloud properties (mean precipitation rate) of the cloudy (precipitating) area.

The above idea is illustrated by Kedem, et al. (1990), who concluded that a linear relationship exists in a statistical sense between area-averaged rain rate (i.e., volume per unit area) and the fractional area of rain in convective systems. Figure 7.4, the grid mean albedo versus cloud fraction graph, is the radiation equivalent. For rainfall, the above argument requires a minimum rain rate over the fractional area and it can not be raining over the entire area at one time. Since the precipitation rate of the rainy area must maintain a certain threshold, so to must the mean cloud properties of a cloudy area O(100 km). This is represented by the horizontal portion of the cloudy albedo versus cloud fraction graph of Figure 7.3. Also, just as it is not allowed to be raining over the entire area, the 100% cloud fraction (vertical portion) of Figure 7.3 is not allowed to occur. The mean rainfall rate (cloud properties) where it is raining (cloudy) is then unique to the rainfall (cloud fraction) climatology of the location. Eltahir and Bras (1993) used this idea to estimate the fractional coverage of rainfall within a GCM grid box by using station data for the local mean rain rate and GCM output of grid-mean rain rate.

Thus, the study of individual boxes implies there may be a local mean liquid water path associated with partly cloudy areas of O (100 km). Following the convention Kedem, et al. outlined for convective rainfall, it appears that the instantaneous value of LWP of the cloudy area is the average of a population that does not change with change in cloud fraction. Thus, for an area the size of a GCM grid box, there is a distribution of LWP which does not change appreciably. The probability distribution function (PDF) graph of the 1987 box A with its peak at the central TAU category is a good example. As mentioned previously, this scenario idealizes Coakley's (1991) model of uniform and broken layered clouds. The individual cells within a layer contain different LWP distributions. Over the box, the distribution may be modeled by an exponential form (Wielicki and Welch 1986). However, the distribution of mean TAU values by ISCCP does not provide an easy method to determine the mean TAU values and hence LWP for a box. Determining an average reflectance and using the ISCCP look up table for corresponding TAU values is one way to calculate the optical depth. Table 4.2 represents this idea. Then by knowing the mean LWP within the cloudy portion of a box, an estimate of the cloud fraction can be derived in the following manner.

In a GCM, the grid mean LWP is determined. From the observations of box A, a mean cloudy albedo is known. By equation (8) a mean cloudy LWP is calculated. Then by assuming only the cloudy portion of the grid box influences the LWP, the following relationship determines the cloud fraction (CF):

$$100\%(\mathrm{LWP}_{\mathrm{grid}}) = (\mathrm{CF})(\mathrm{LWP}_{\mathrm{cloudy}}) + (1 - \mathrm{CF})0\% \qquad (9)$$

In practice, this idea is more difficult to implement than determining the wetted area for rainfall (cloud fraction). Station data provides a history of the local mean rain rate. However, there is no corresponding information regarding cloud LWP observations. The probability distribution graphs indicate that there is some median value that can be used to calculate the LWP and verify the exponential form. To make this calculation, either a cloud scale model or an empirical relationship between cloud LWP's under different meteorological conditions is required. Such a calculation may reduce the need for GCM's to treat marine stratocumulus clouds as plane parallel and use unrealistic LWP to determine realistic albedos (Harshvardhan and Randall 1985).

For an individual grid box O (100 km), the computation of a cloud fraction independent of the GCM liquid water computation will introduce a degree of flexibility not yet incorporated in current models. For example, when open-cell and closed-cell convection occurs, it may be possible to differentiate between their different grid mean properties that occur under different climatological conditions (Agee 1987).

For the spatially averaged grid boxes, the mean cloudy albedo shows a dependence on cloud fraction for a limited range. Therefore, for GCM's with larger grid boxes on the O (1000 km), the climatic region must be treated differently than a GCM with grid boxes on the O (100 km). Also, Kedem, et al.'s ideas mentioned above do not apply. There are several reasons. First, further averaging would ultimately cause the data points to converge to one value in which no trend would be discernible. Secondly, there is a bias towards overcast skies. That is, the 100% cloudy vertical portion of Figure 7.4 is included. For Kedem, et al.'s ideas of rainfall to apply, this scenario is never reached. And finally, with averaging extending to the edges of the stratus region, clouds of different types (i.e., cumulus) are incorporated. Armed with the above information, a climate change experiment could then include a cloud fraction feedback mechanism. Now the question is how these conclusions fit with the tropical results presented next.

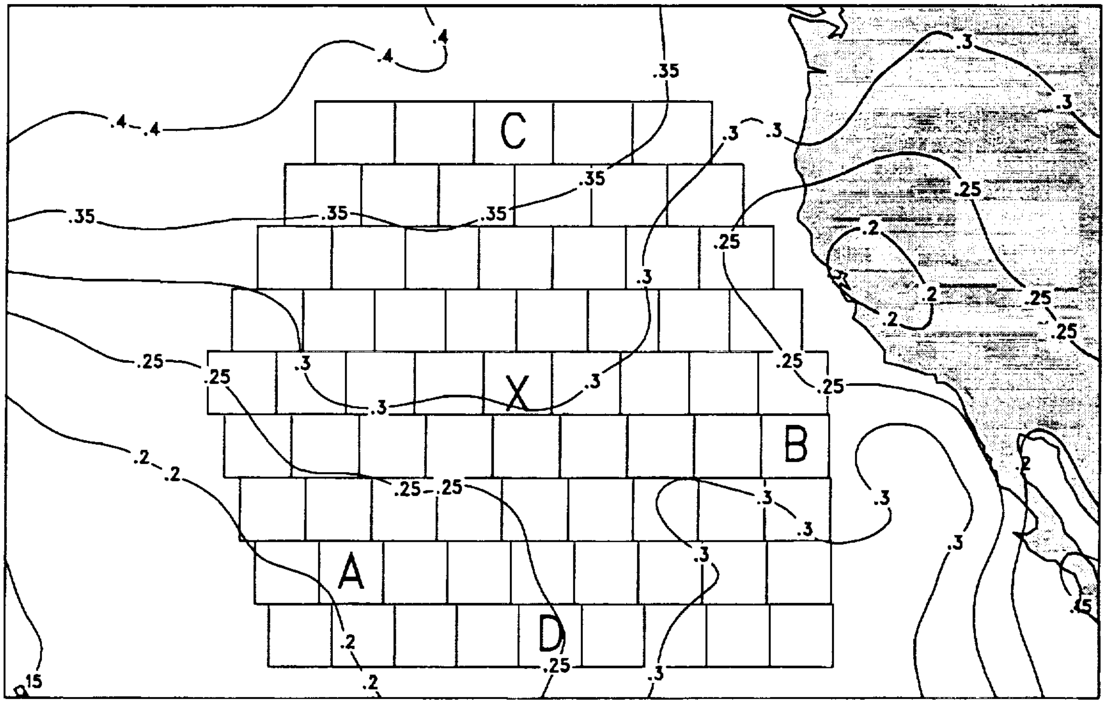

Figure 7.1 ERBE July 1987 monthly mean spherical albedo and the location of individual boxes of study.

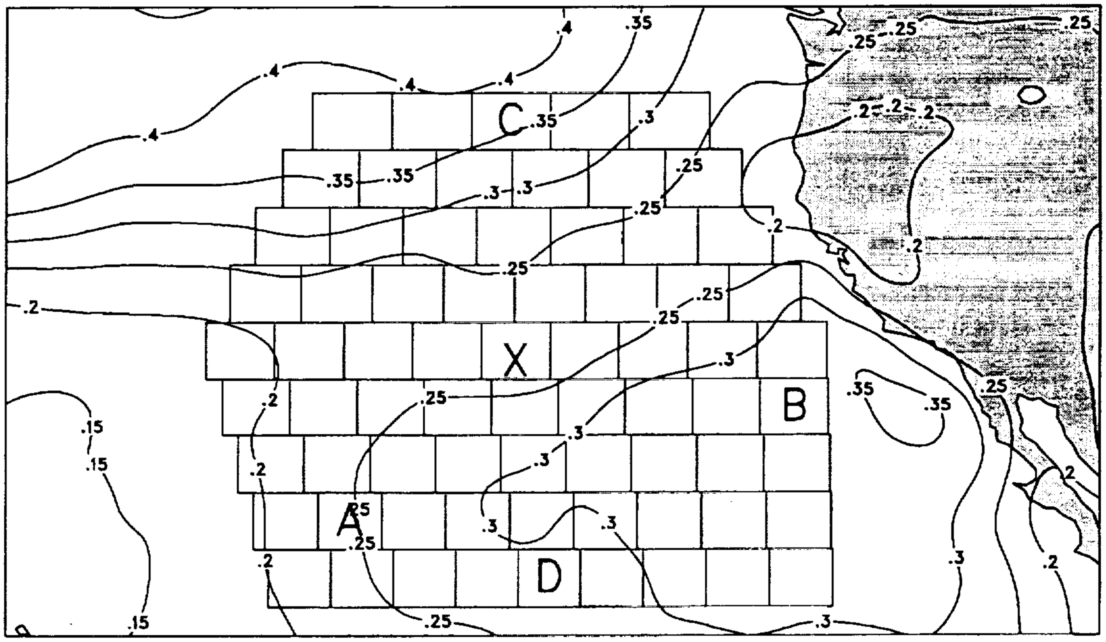

Figure 7.2 ERBE July 1988 monthly mean spherical albedo and the location of individual boxes of study.

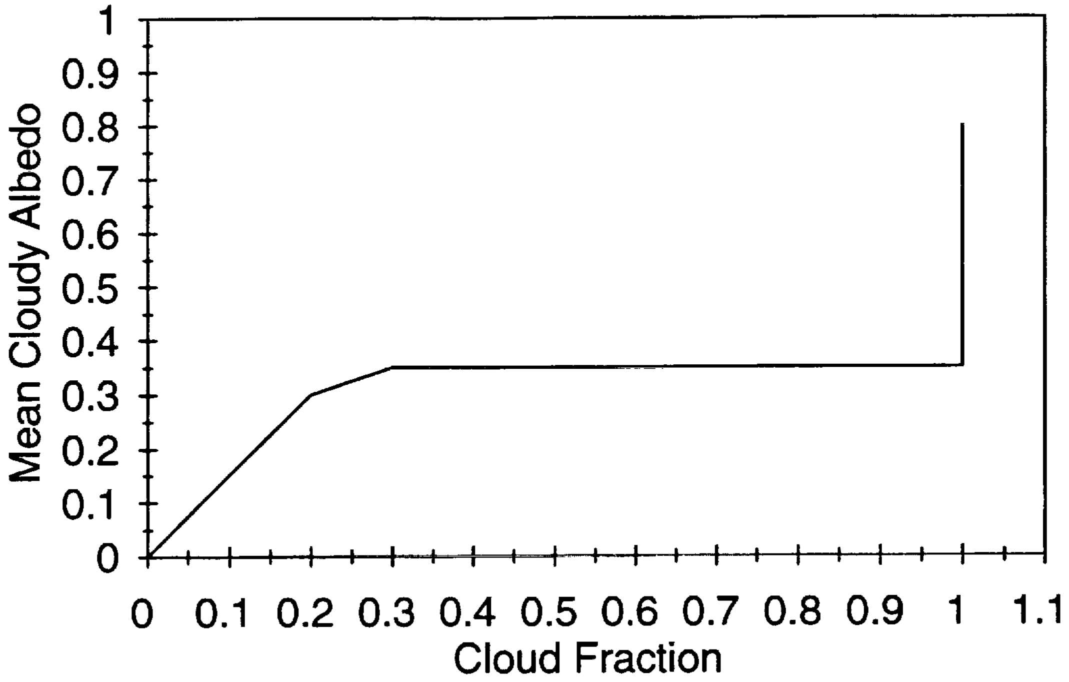

Figure 7.3 An idealized plot of mean cloudy albedo versus cloud fraction over a black surface.

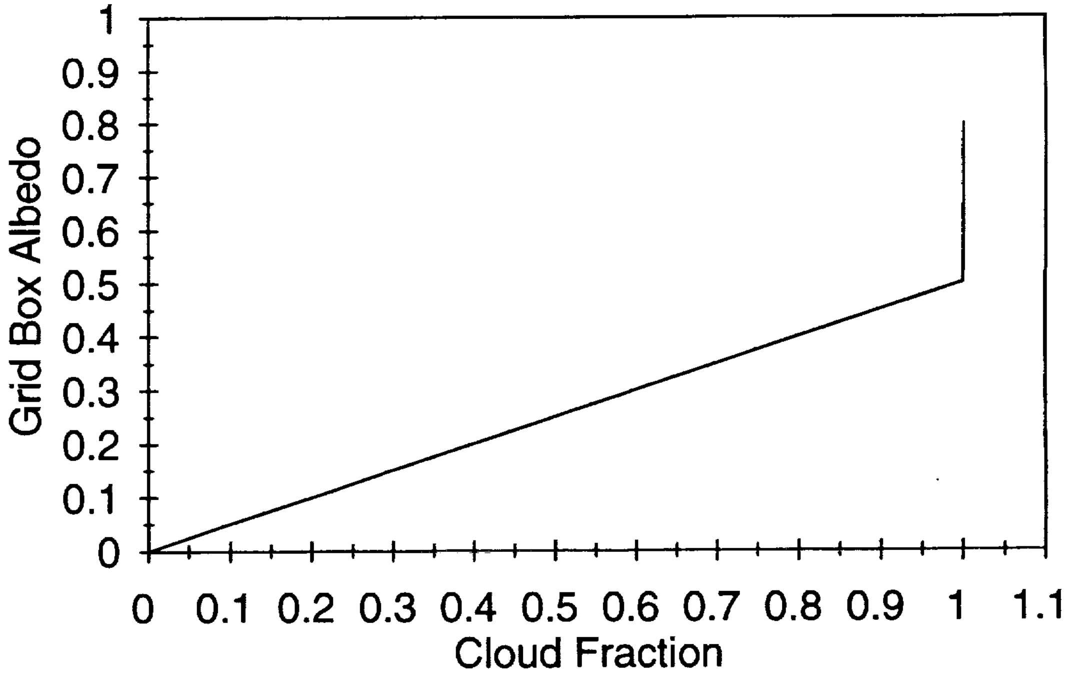

Figure 7.4 An idealized plot of grid box albedo versus cloud fraction over a black surface.

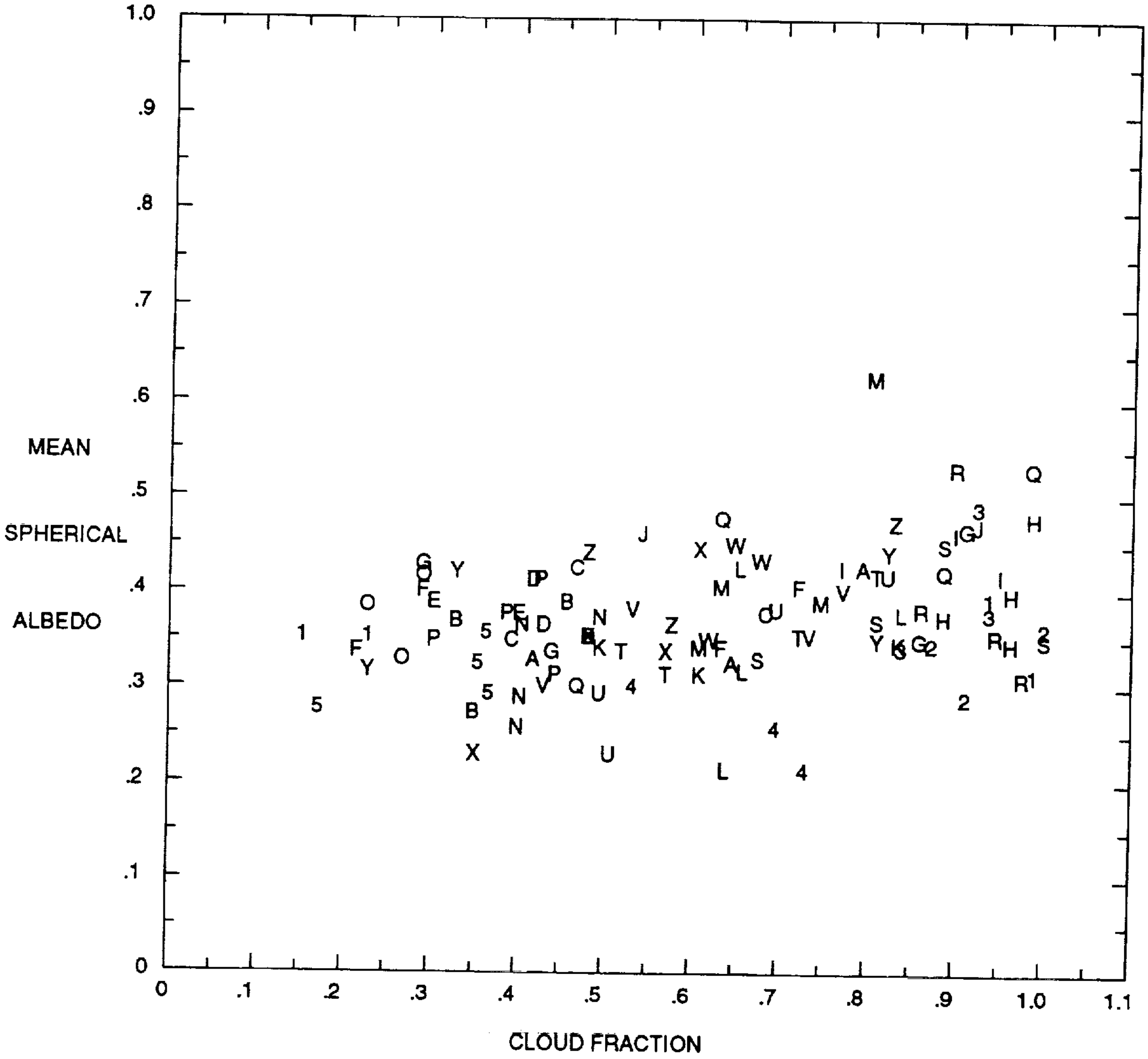

Figure 7.5 July 1987 mean spherical albedo versus cloud fraction for box A.

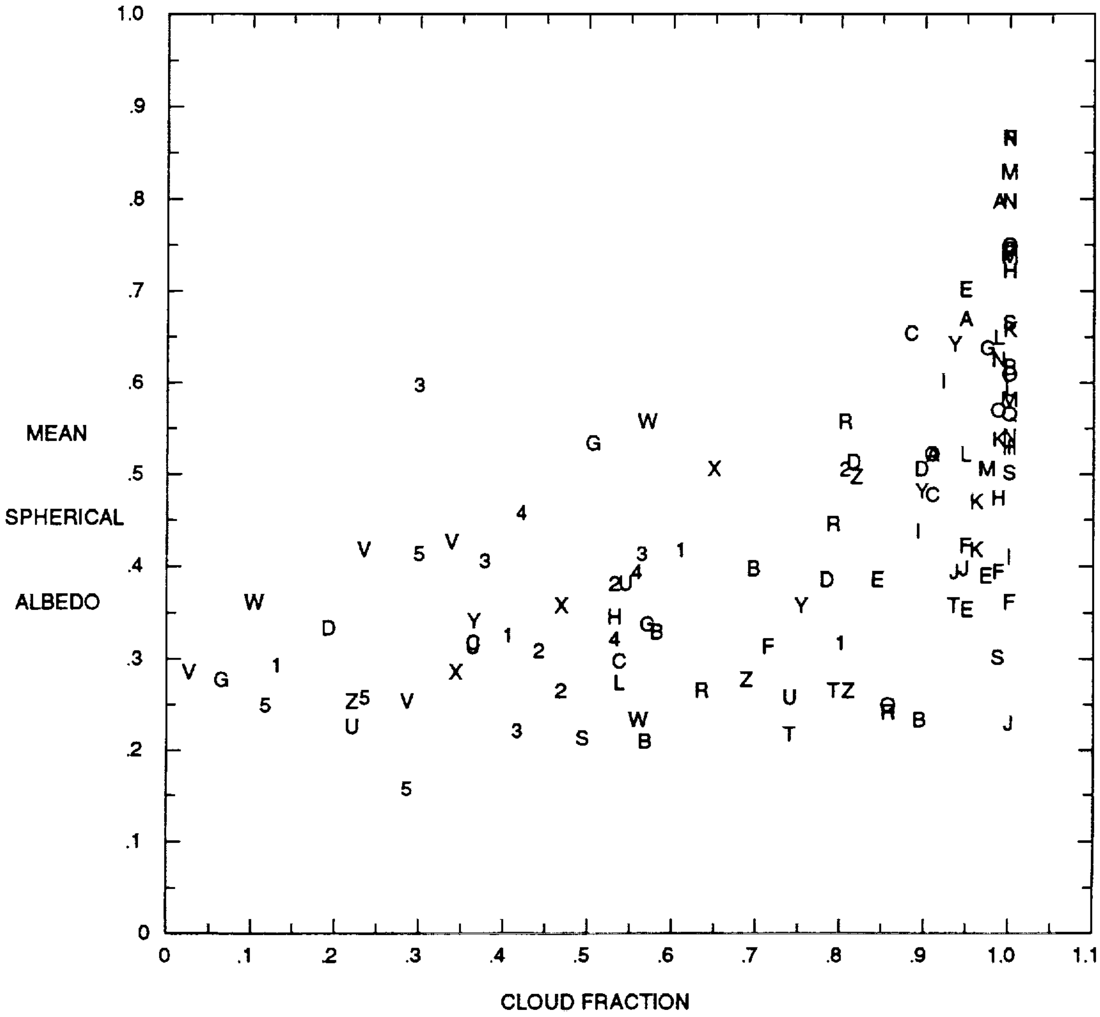

Figure 7.6 As in Fig 7.5, except for box B.

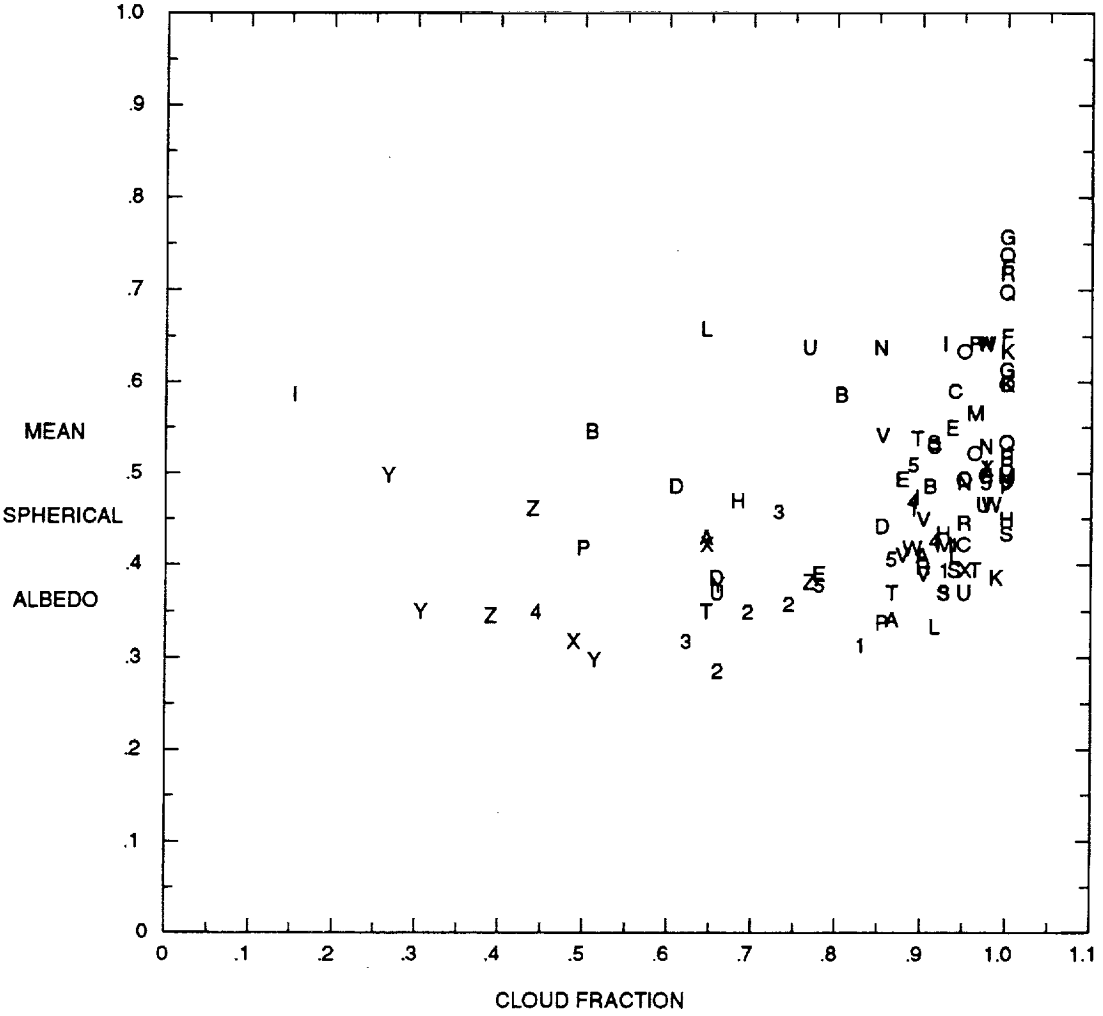

Figure 7.7 As in Fig 7.5, except for box X.

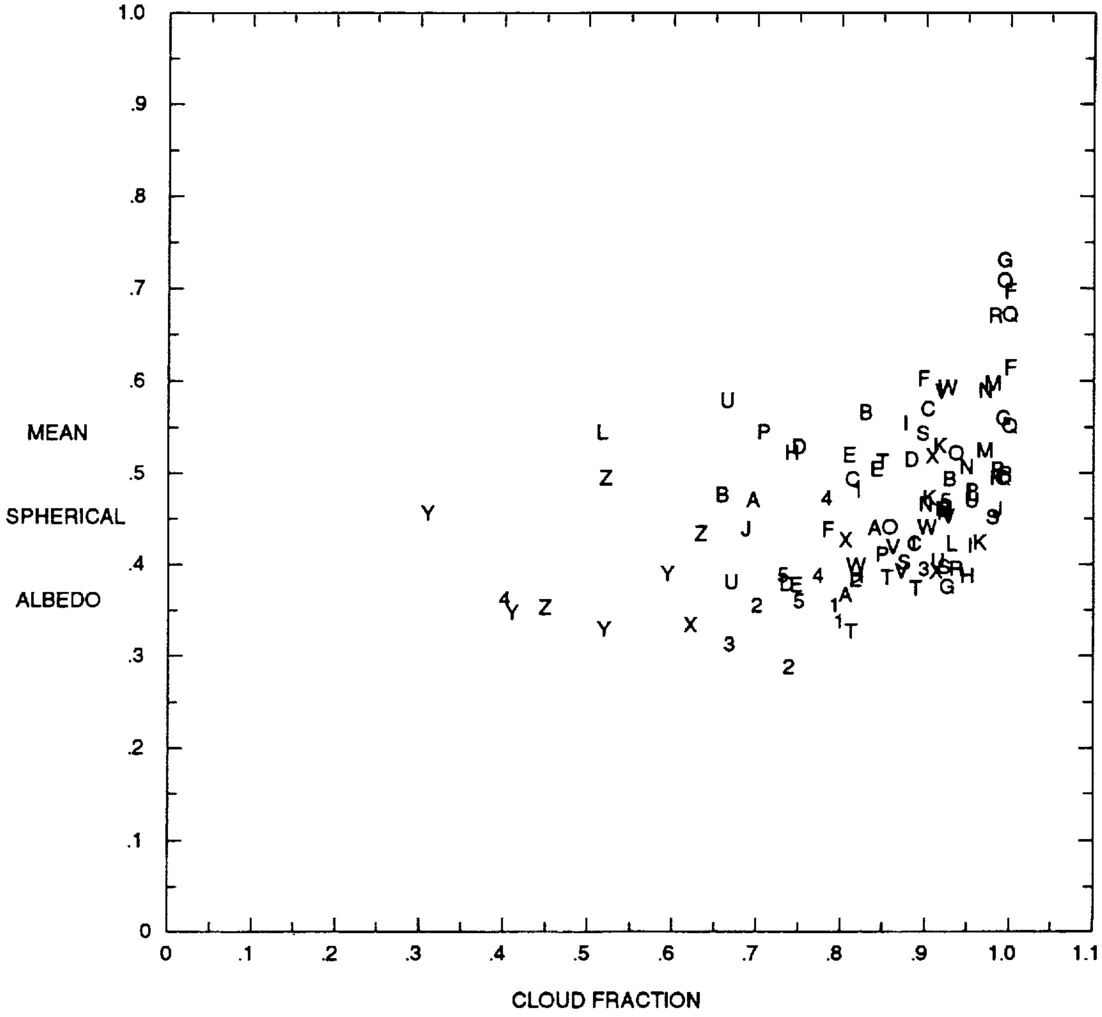

Figure 7.8 July 1987 mean spherical albedo versus cloud fraction for the first ring around box X.

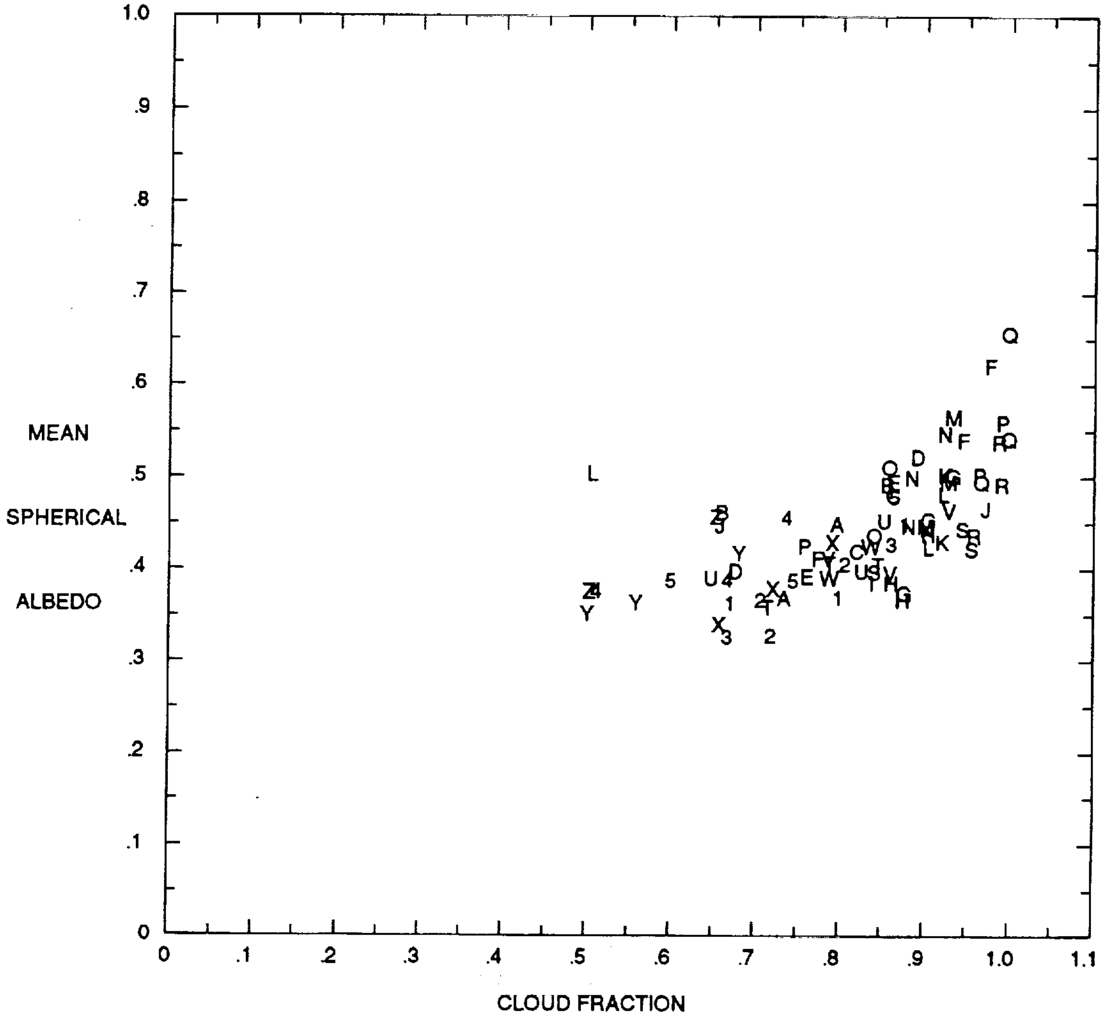

Figure 7.9 As in Fig. 7.8, except for the second ring around box X.

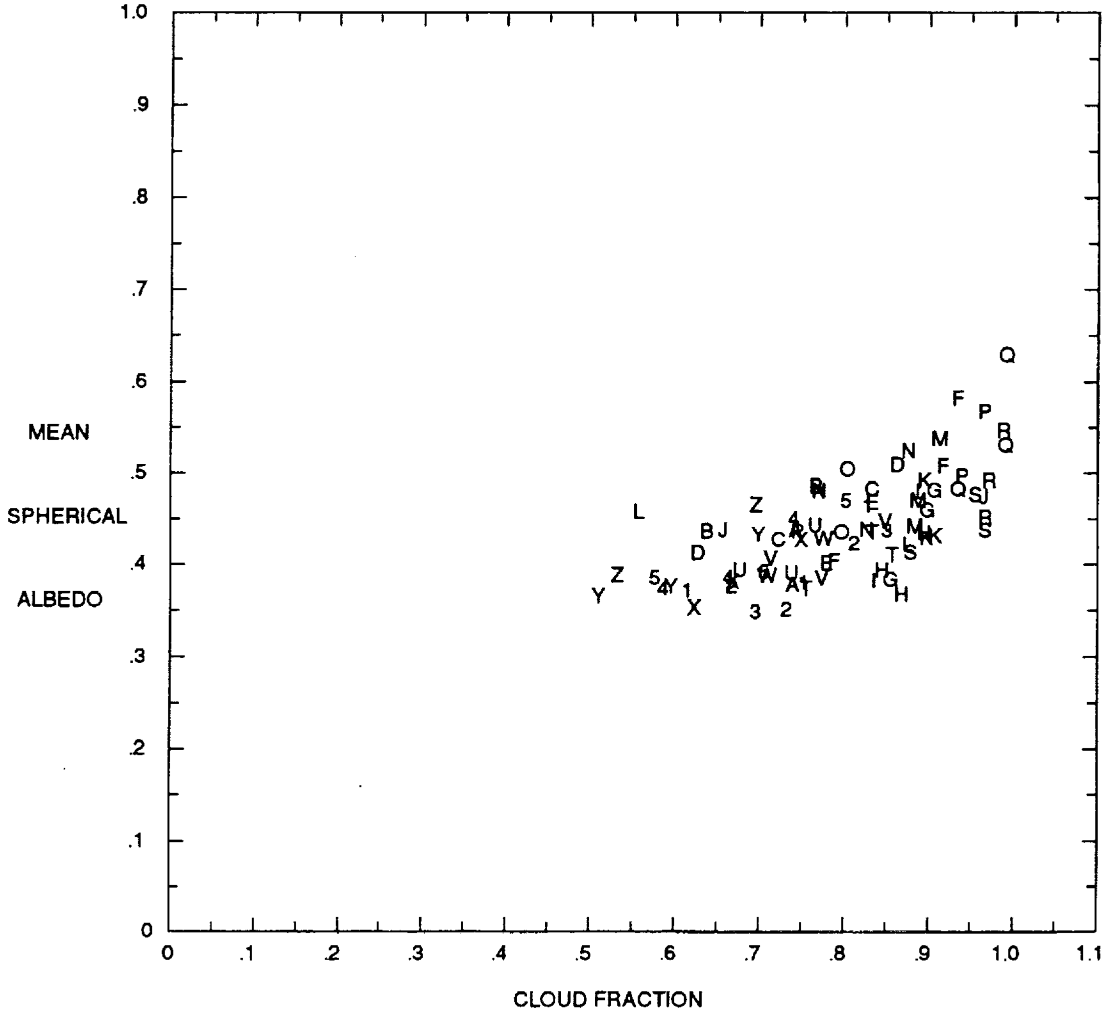

Figure 7.10 As in Fig. 7.8, except for the third ring around box X.

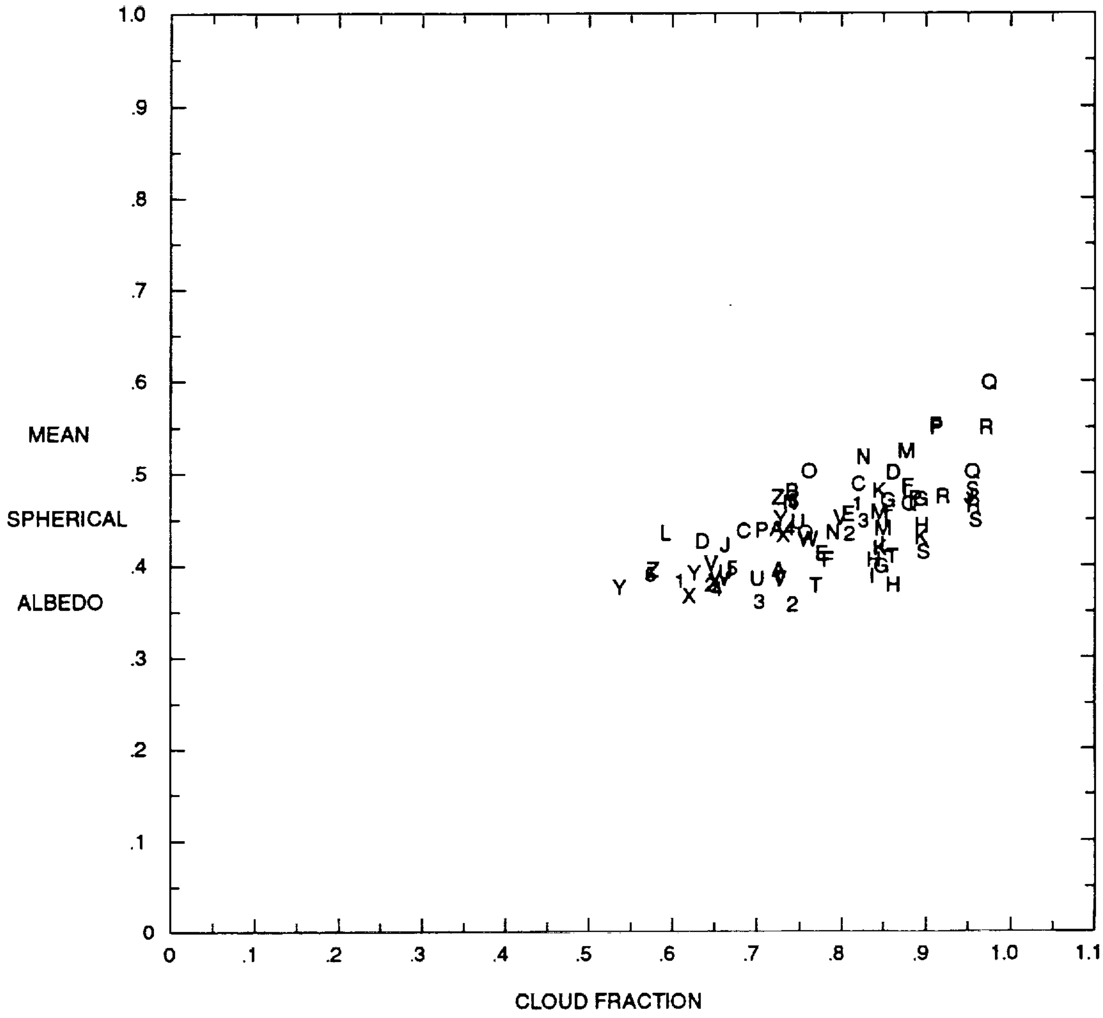

Figure 7.11 As in Fig. 7.8, except for the fourth ring around box X.

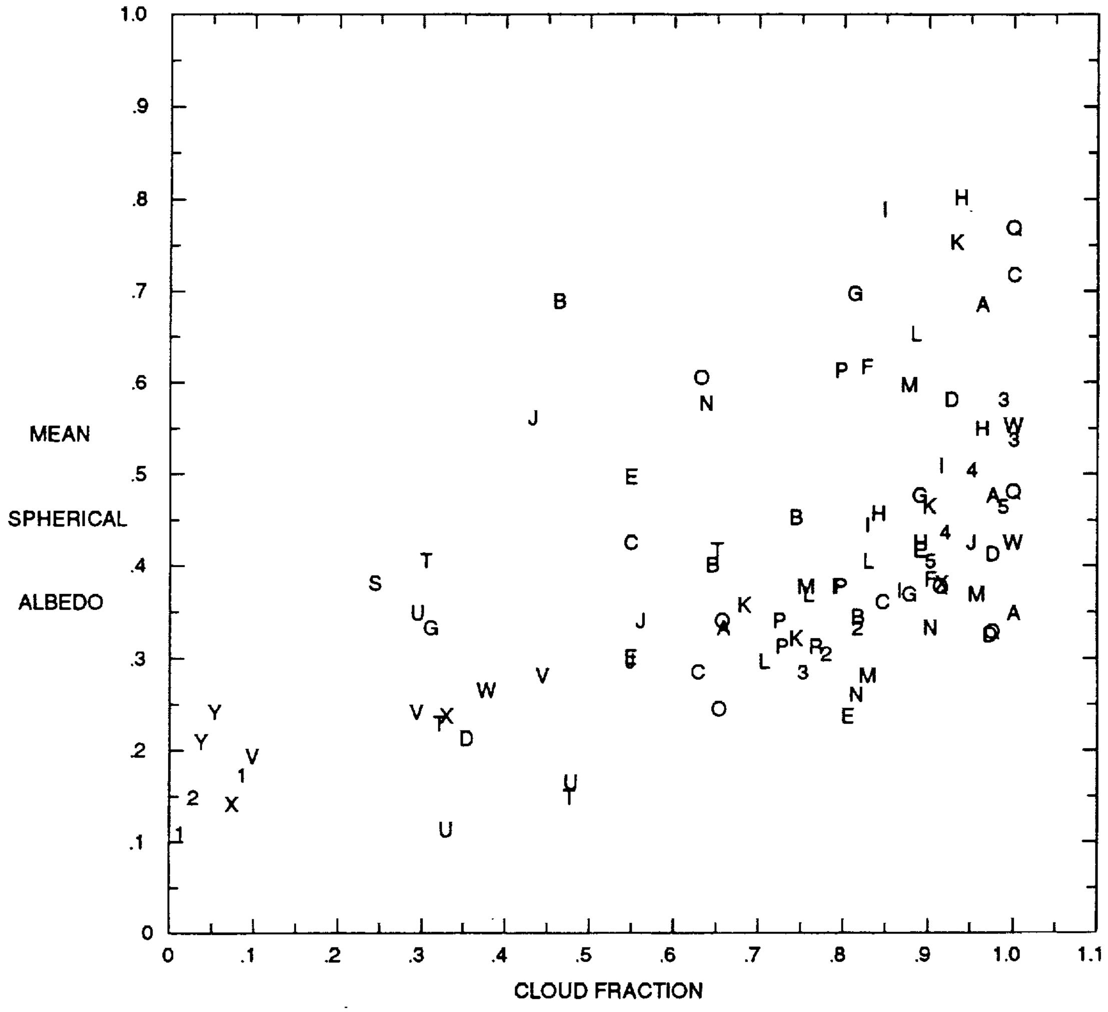

Figure 7.12 July 1988 mean spherical albedo versus cloud fraction for box X.

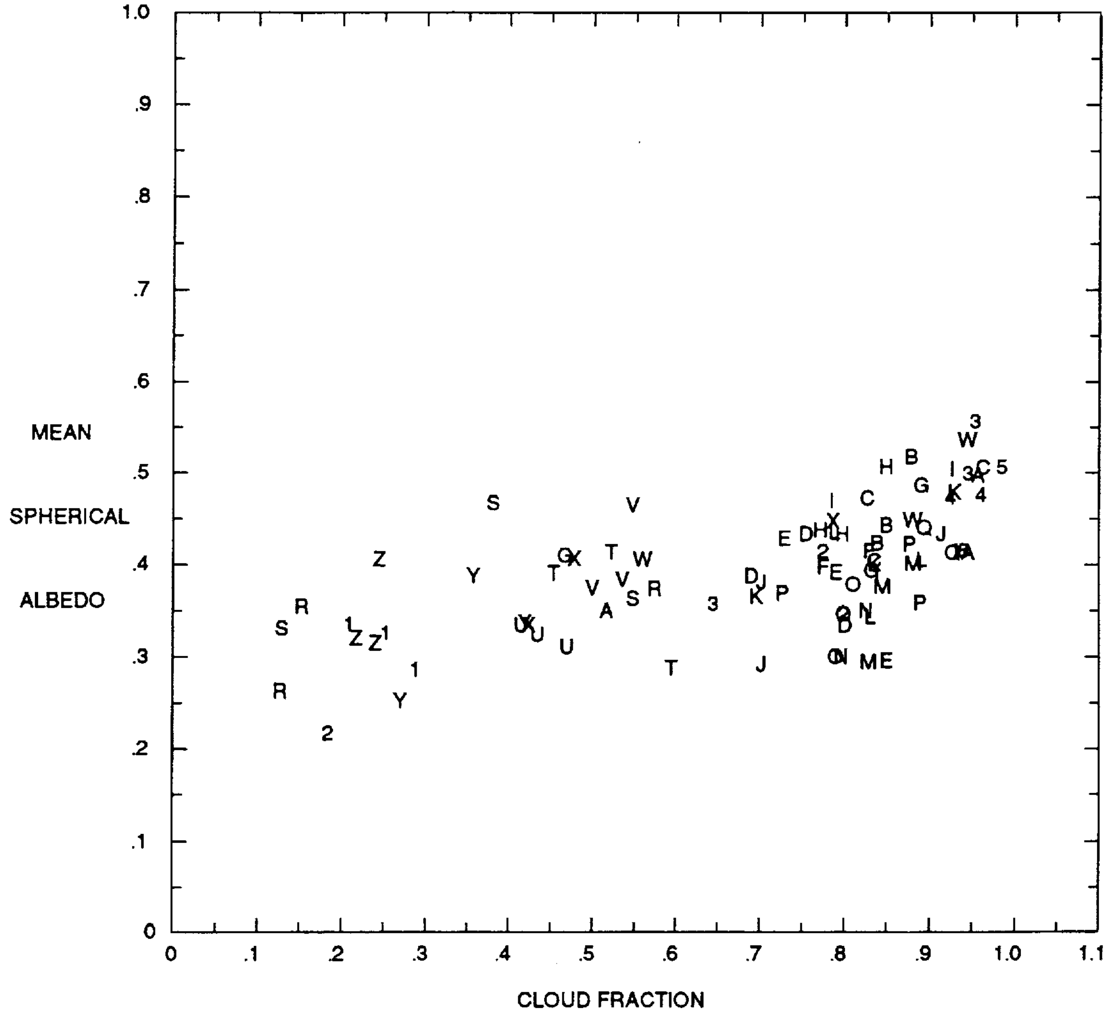

Figure 7.13 July 1988 mean spherical albedo versus cloud fraction for the first ring around box X.

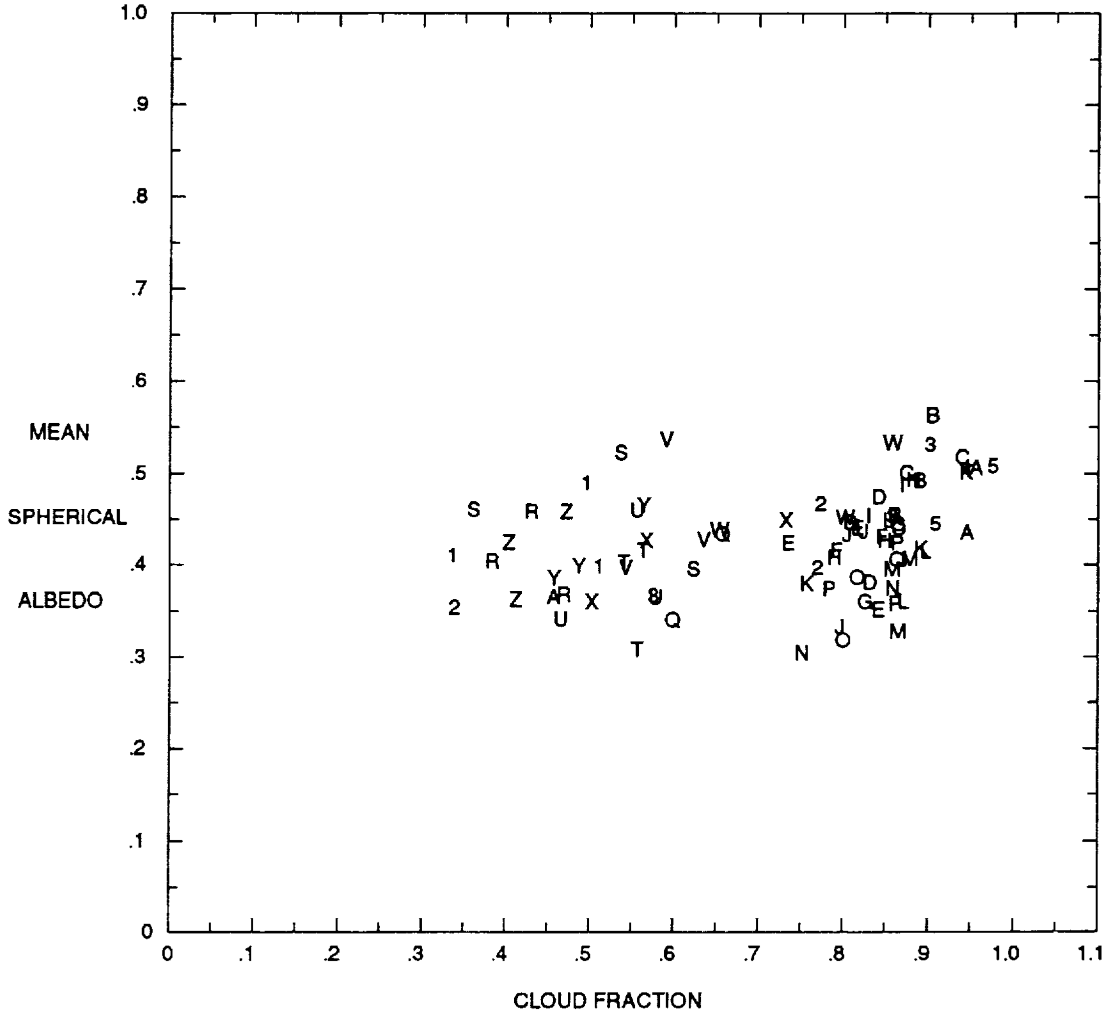

Figure 7.14 As in Fig. 7.13, except for the second ring around box X.

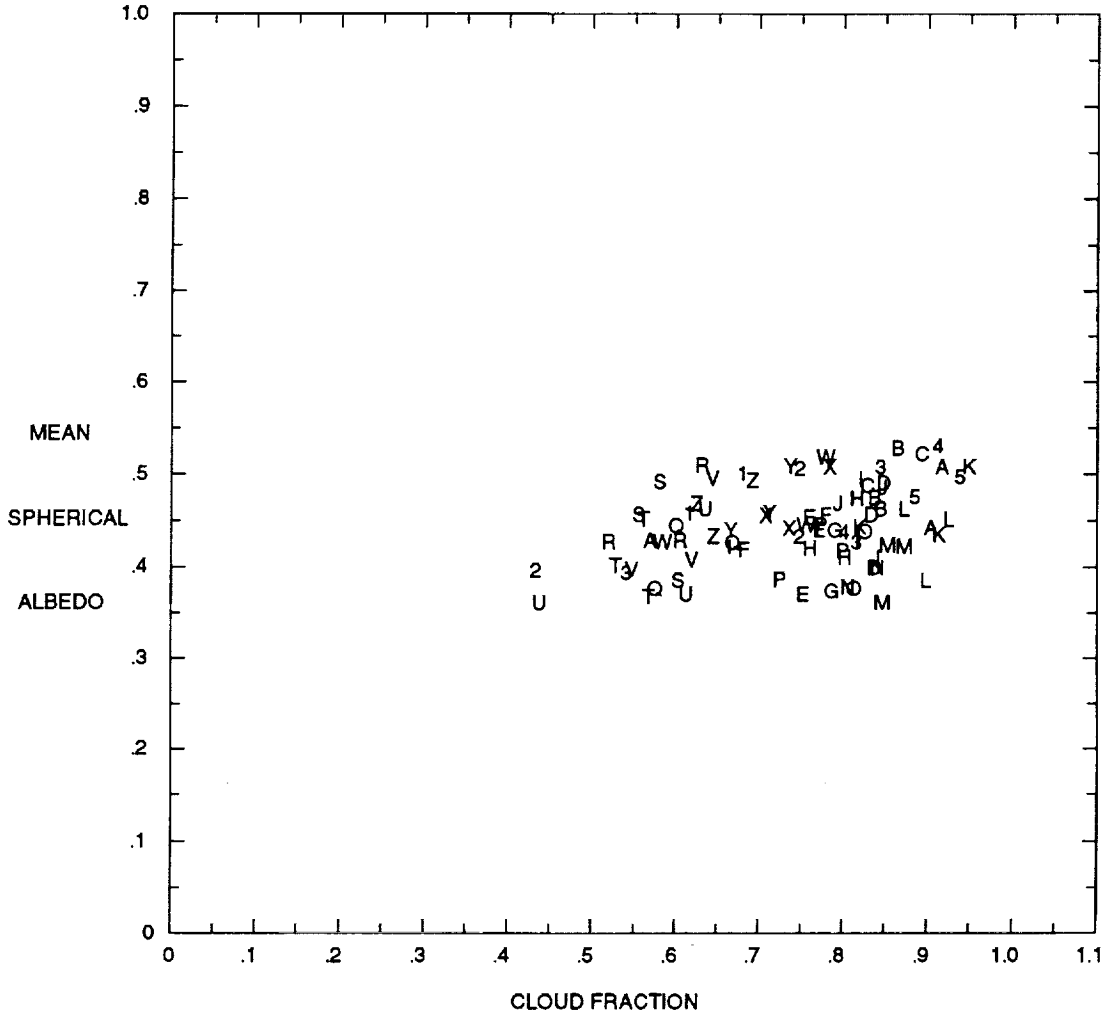

Figure 7.15 As in Fig. 7.13, except for the fourth ring around box X.

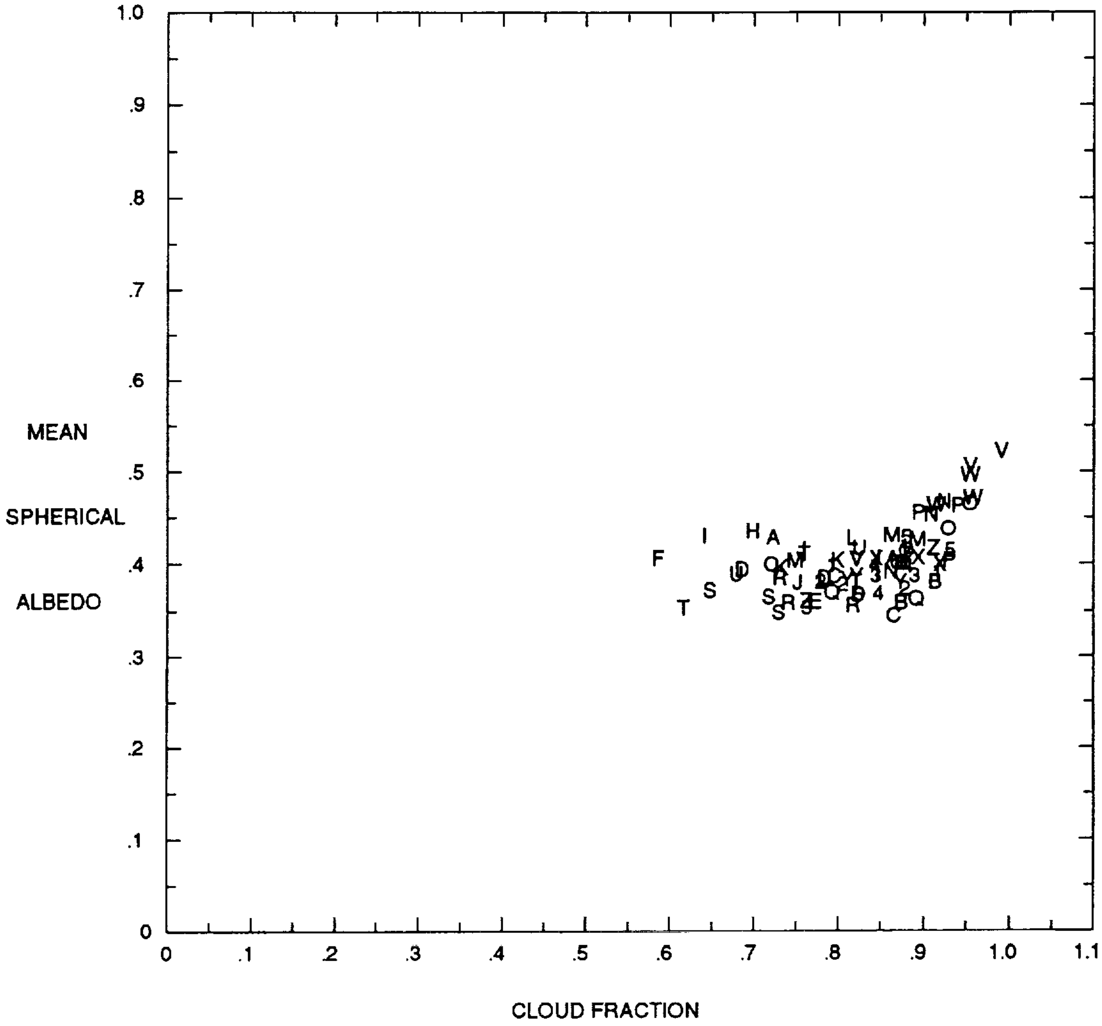

Figure 7.16 July 1986 mean spherical albedo versus cloud fraction for the fourth ring around box X.

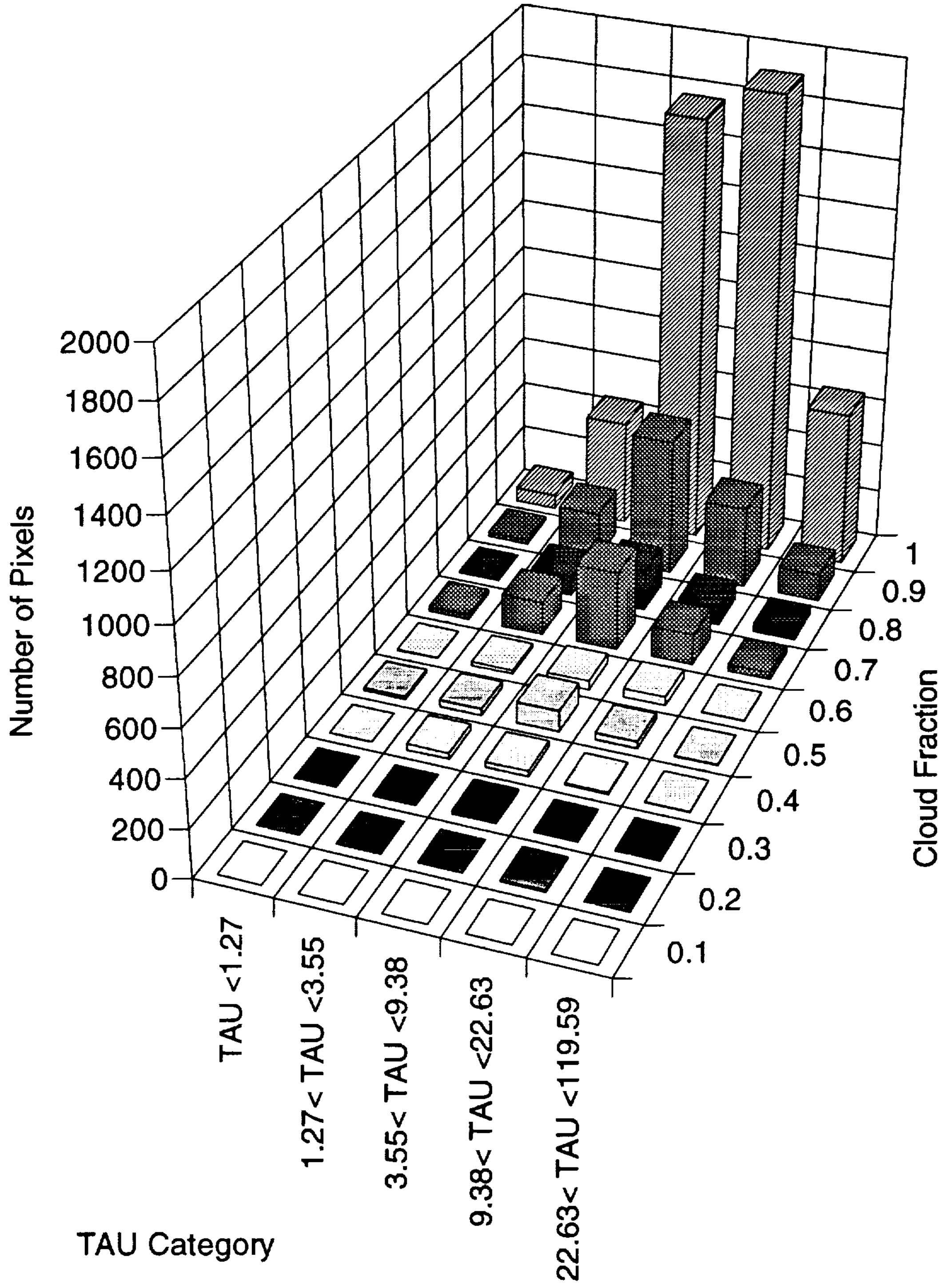

Figure 7.17 Number of cloudy pixels per TAU category versus cloud fraction for box X, July 1987.

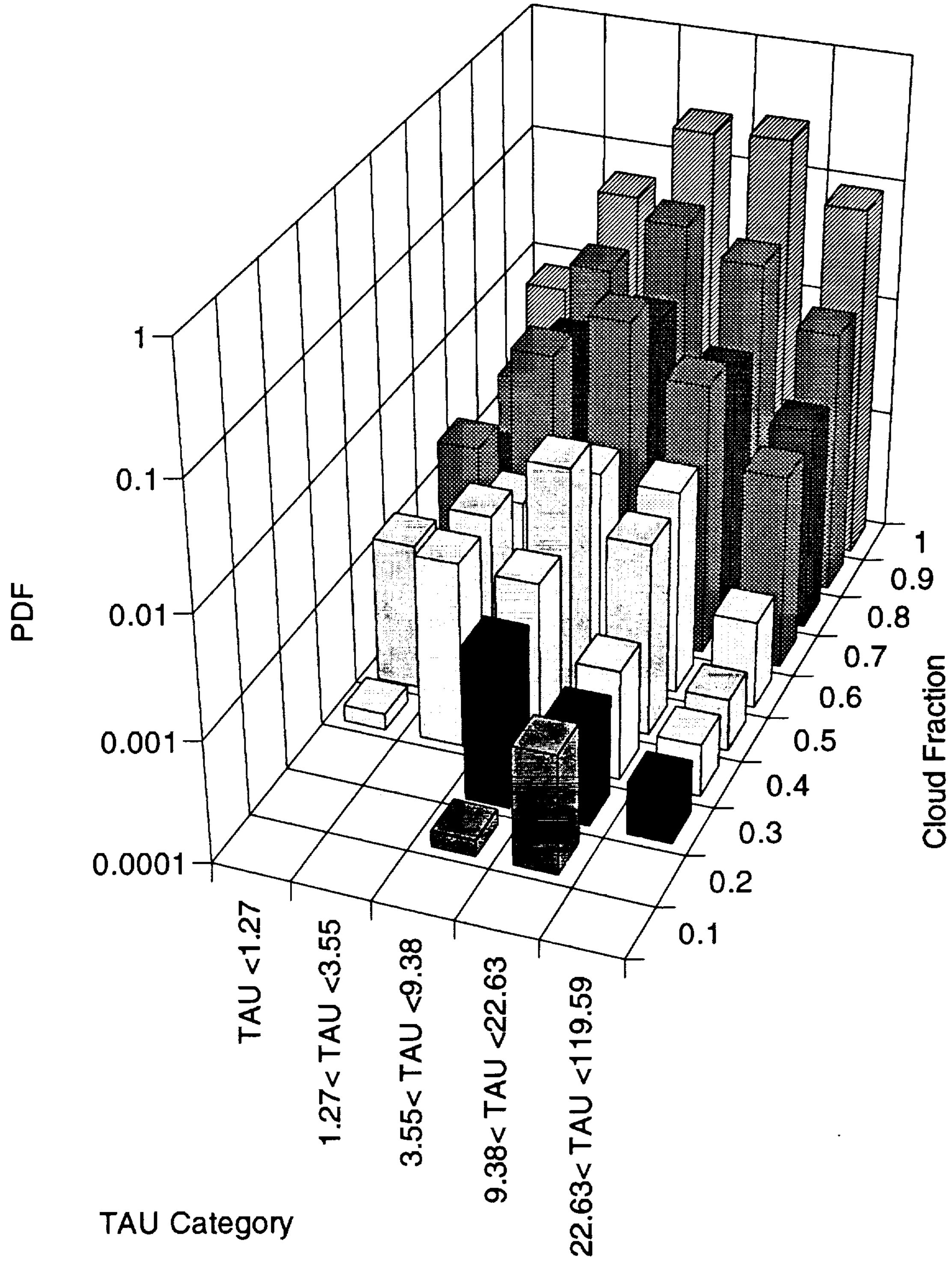

Figure 7.18 The base ten logarithm of the probability distribution function (PDF) with respect to cloud fraction and TAU category for box X, July 1987.

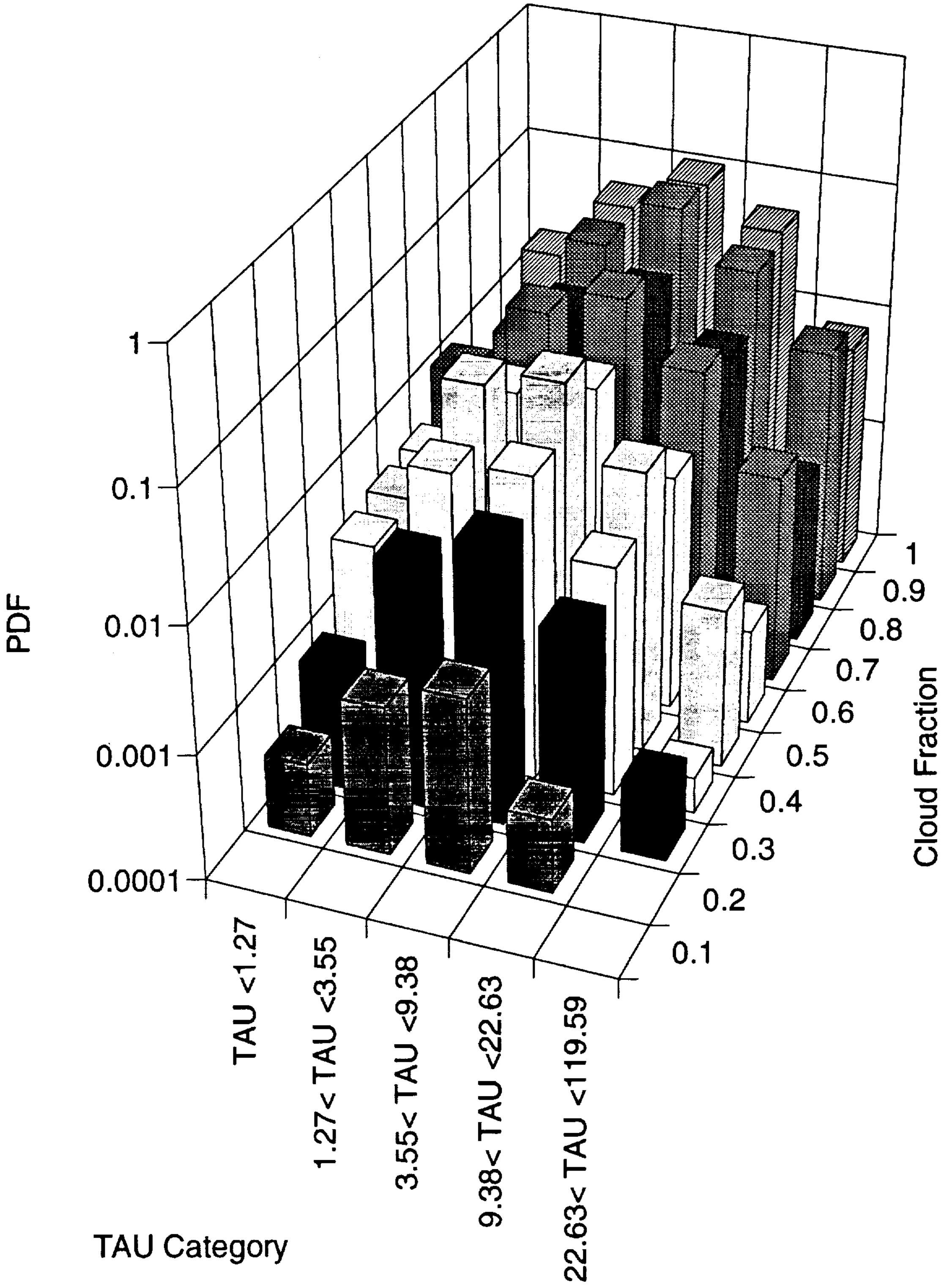

Figure 7.19 As in Fig. 7.18, except for box A.

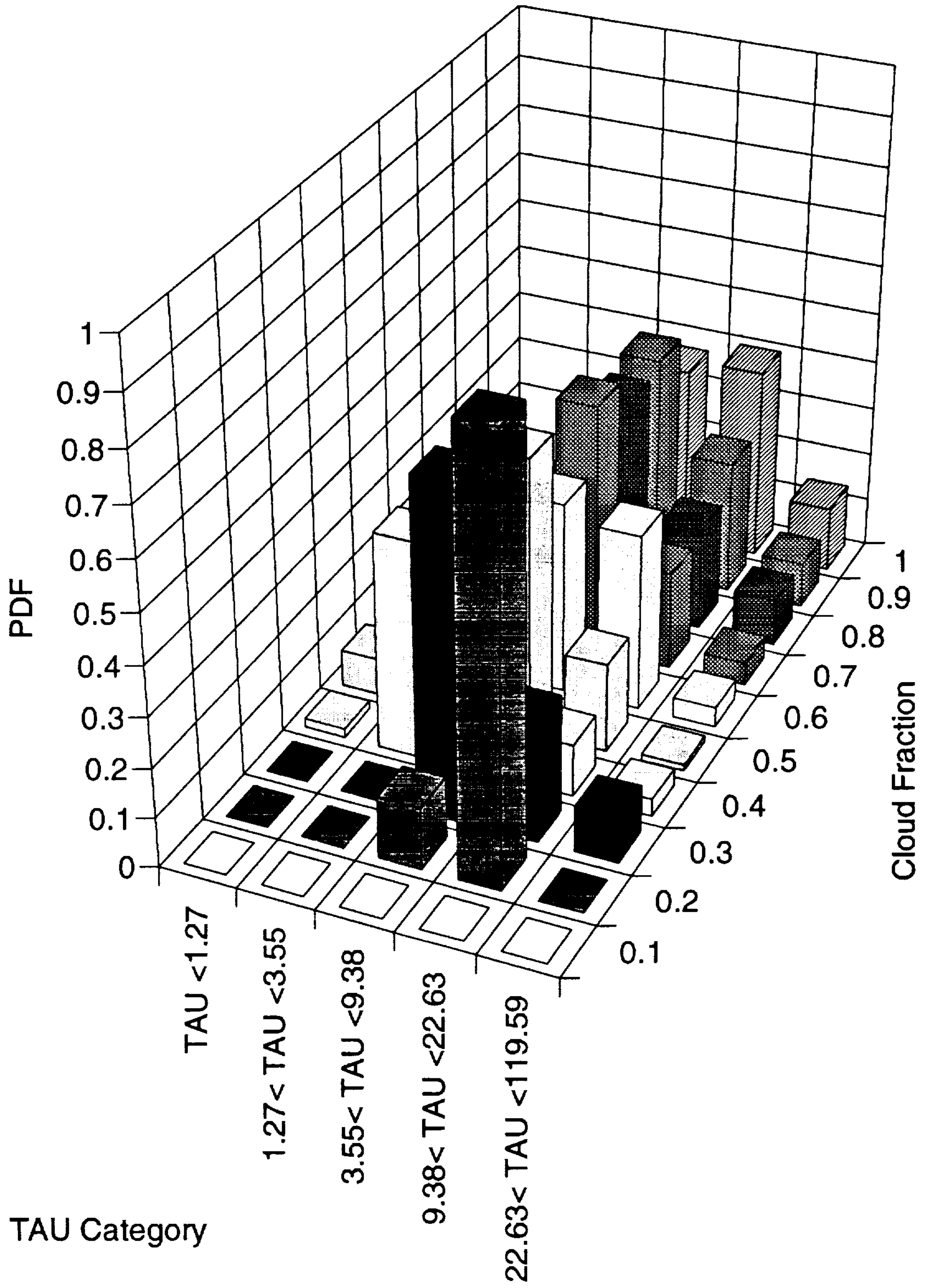

Figure 7.20 The probability distribution function (PDF) with respect to cloud fraction for box X, July 1987.

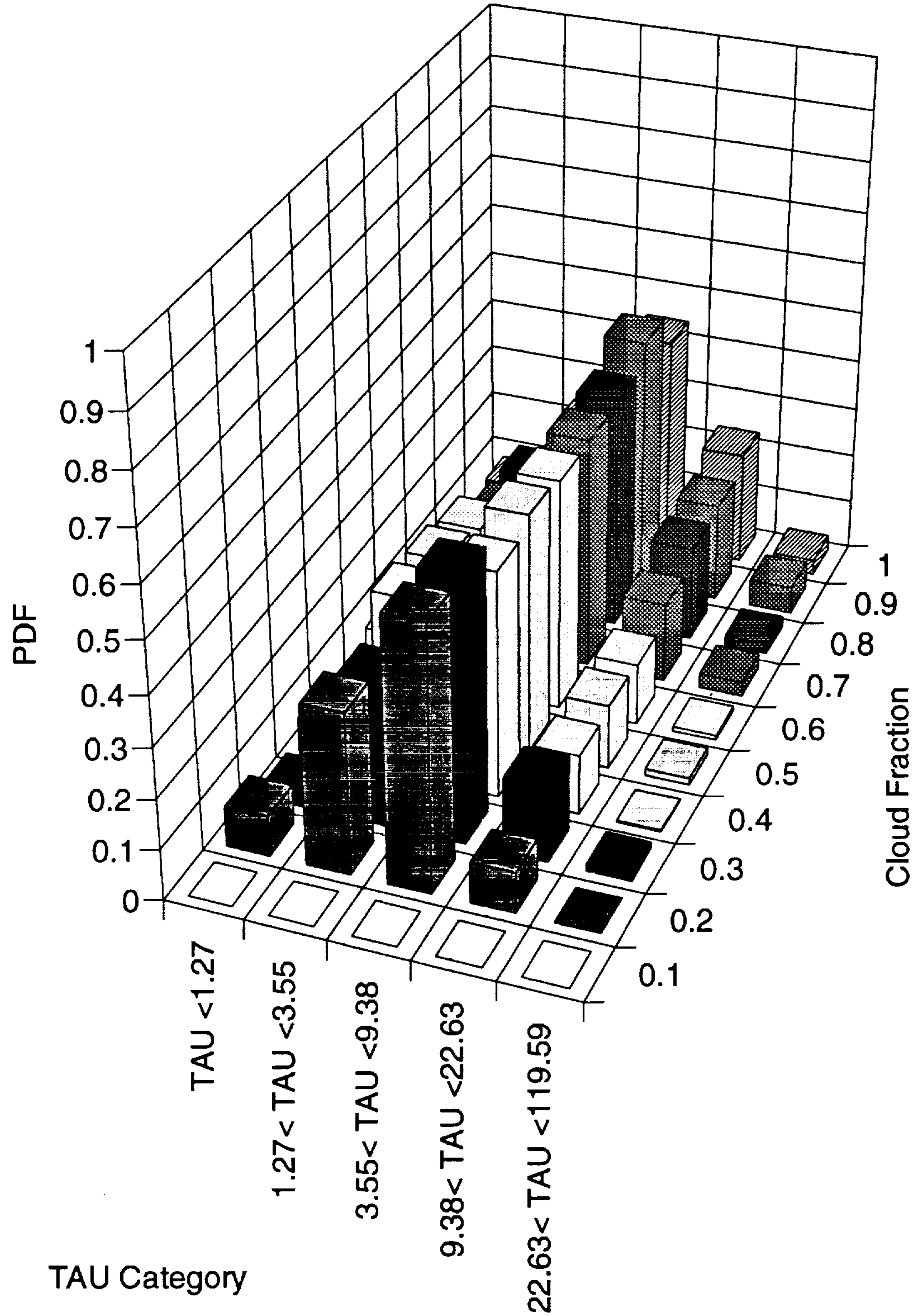

Figure 7.21 As in Fig. 7.20, except for box A.

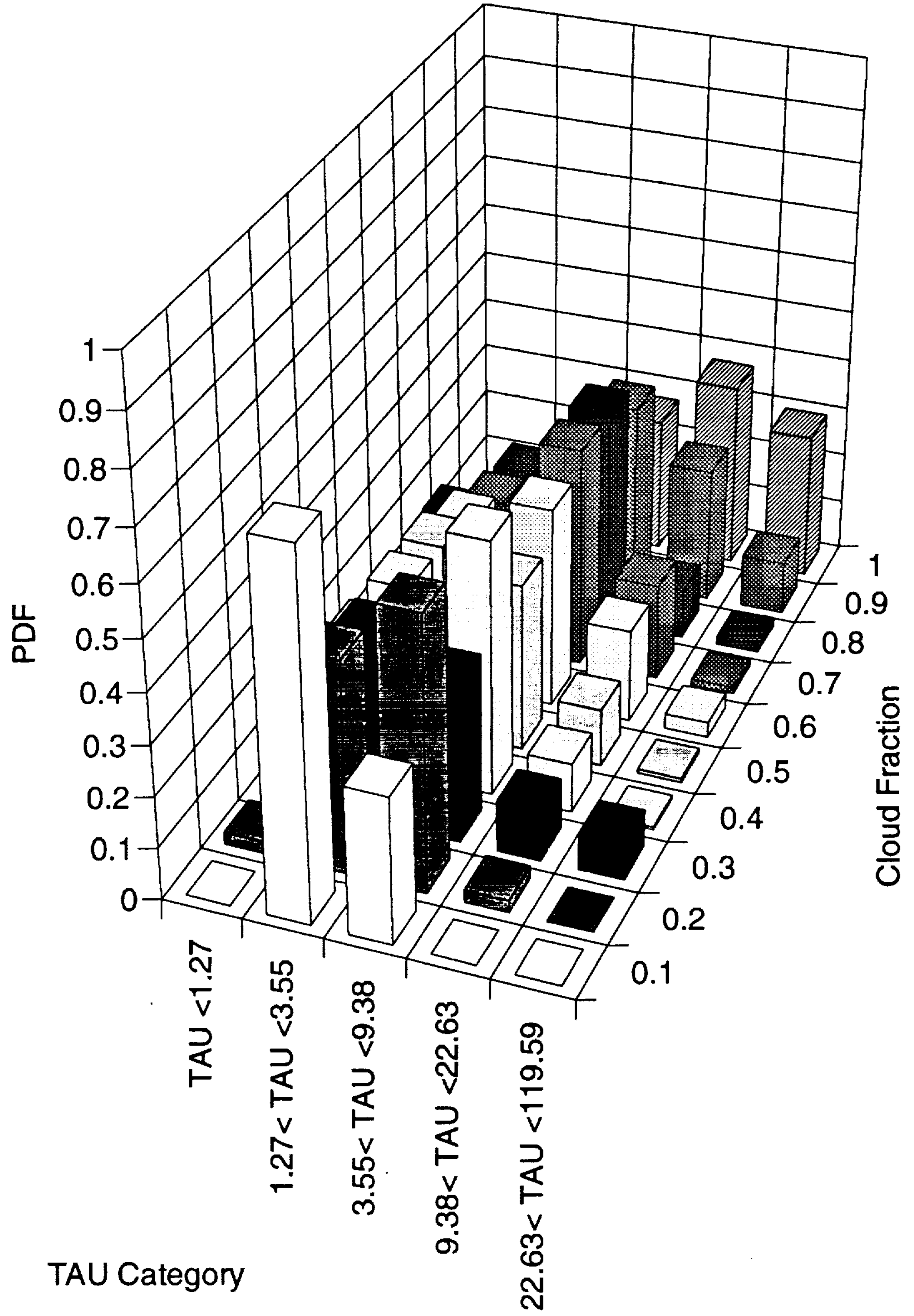

Figure 7.22 As in Fig. 7.20, except for box B.

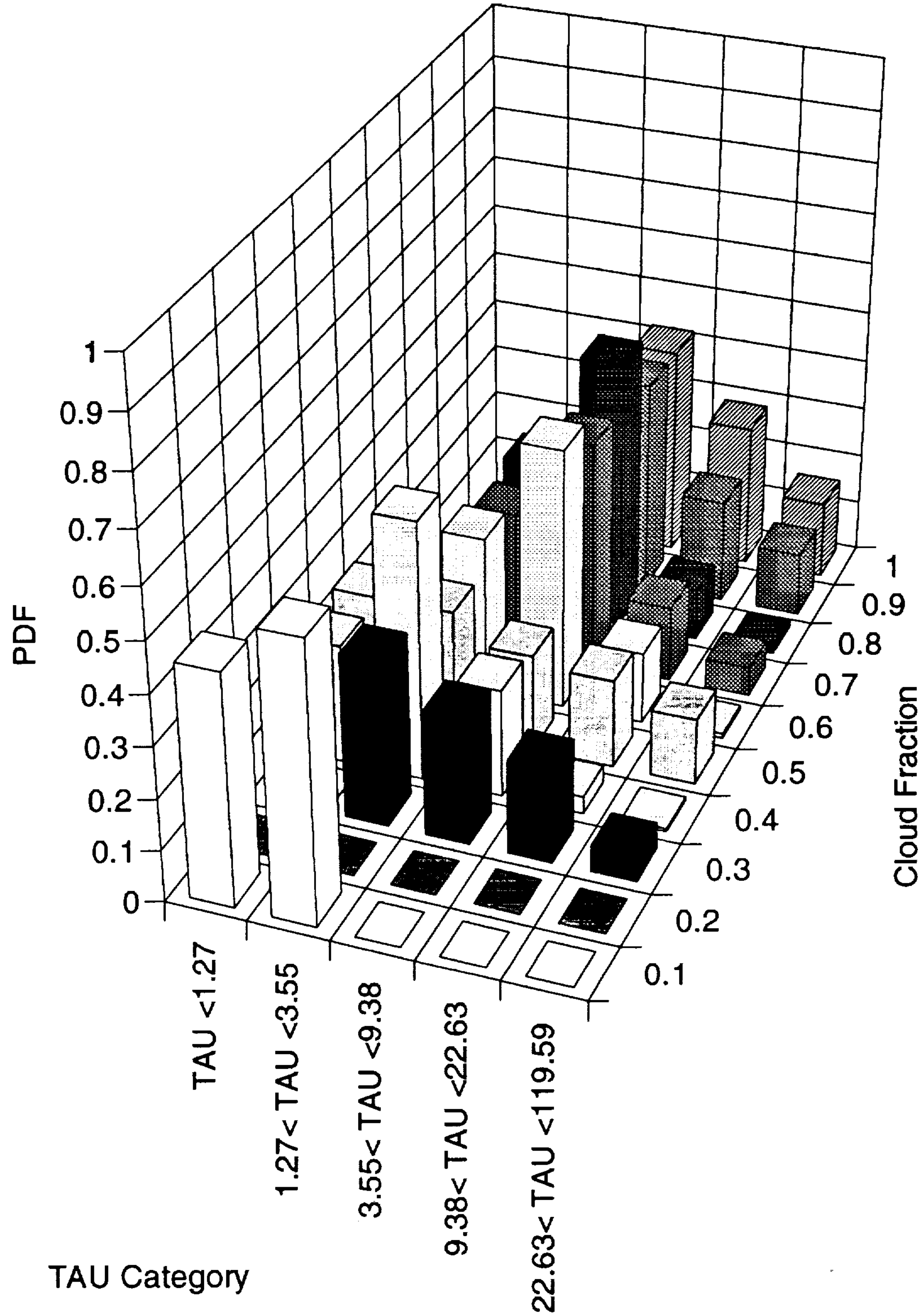

Figure 7.23 The probability distribution function (PDF) with respect to cloud fraction for box X, July 1988.

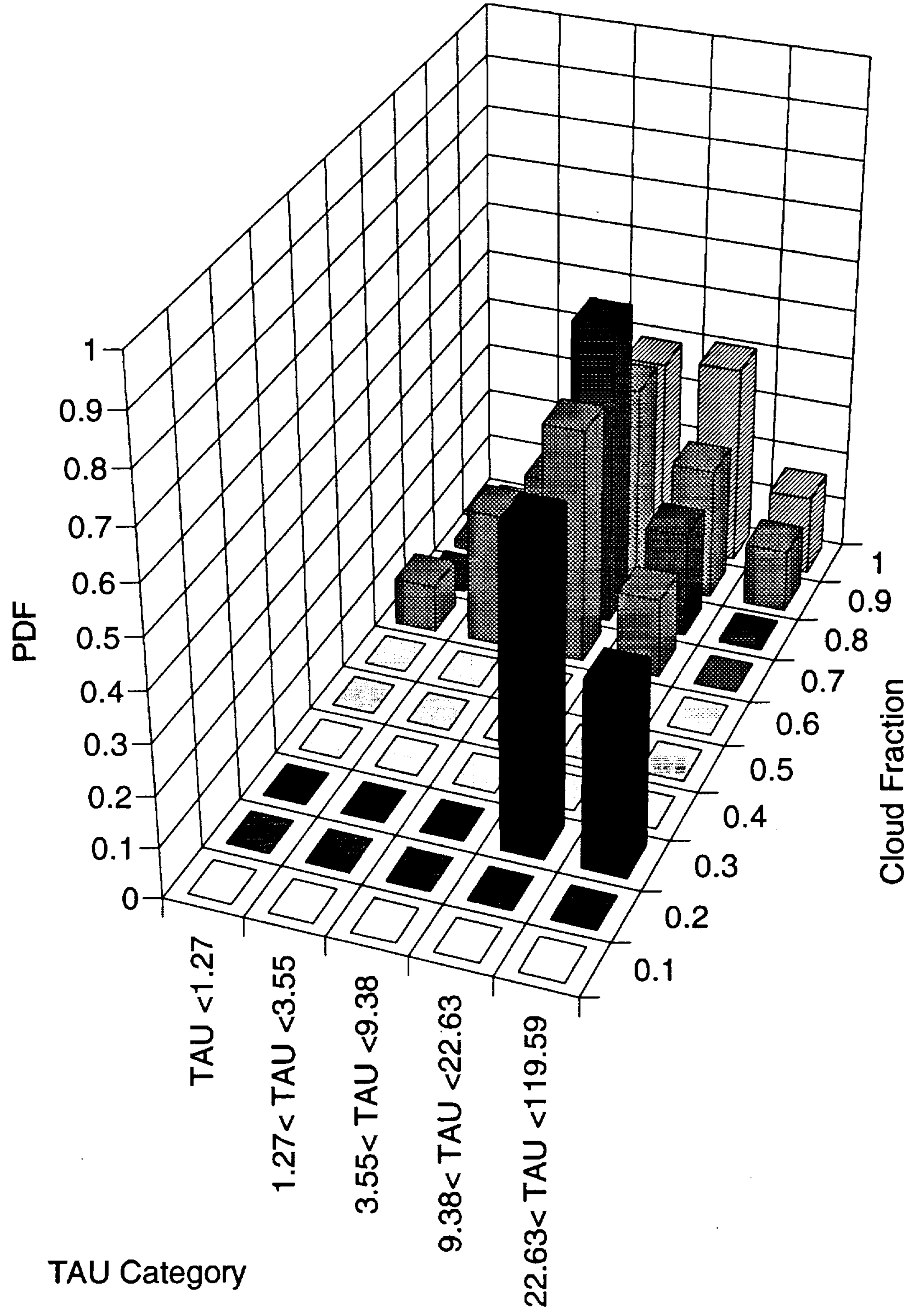

Figure 7.24 As in Fig. 7.20, except for box C.

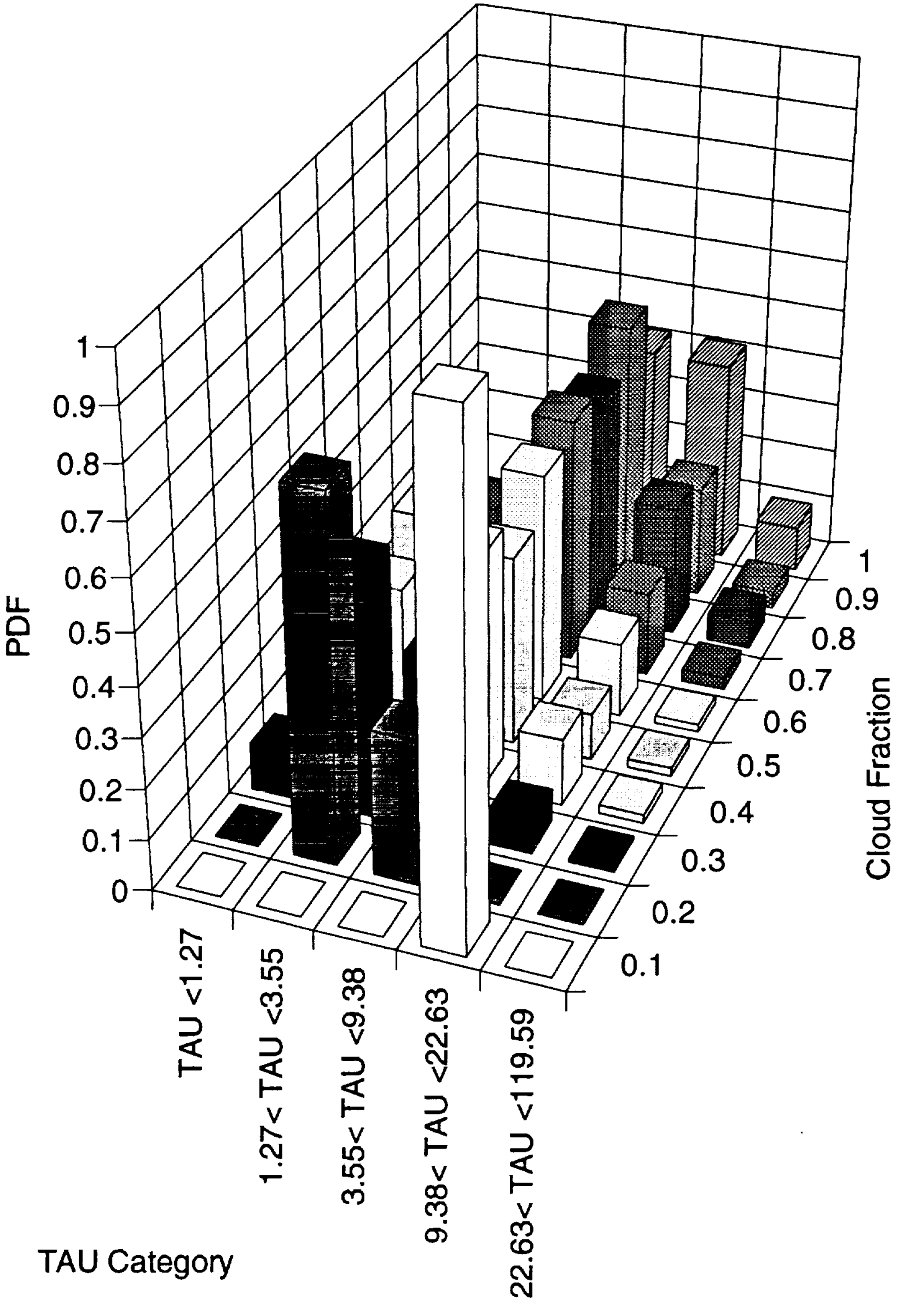

Figure 7.25 As in Fig. 7.20, except for box D.

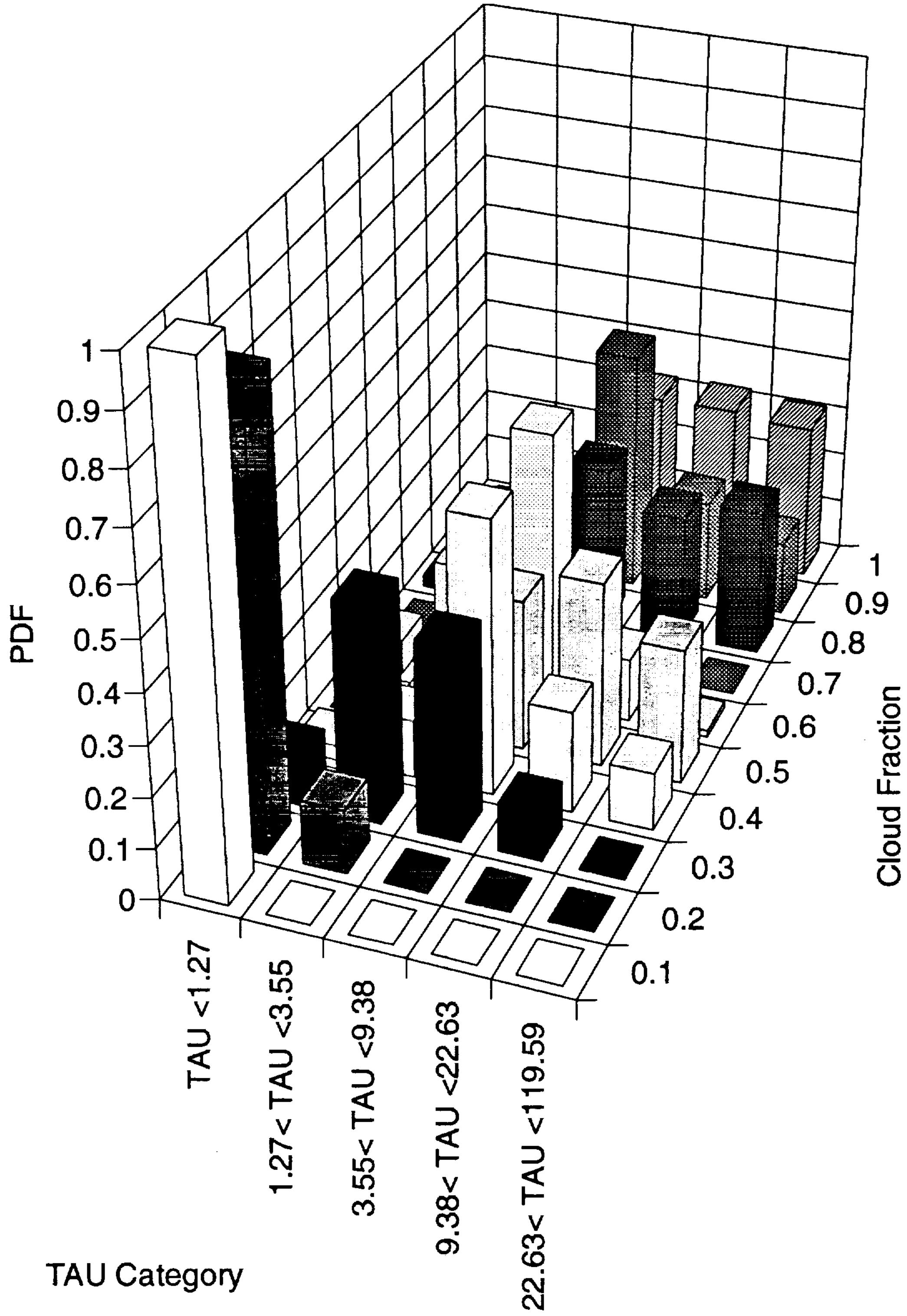

Figure 7.26 The probability distribution function (PDF) with respect to cloud fraction for box C, July1988.

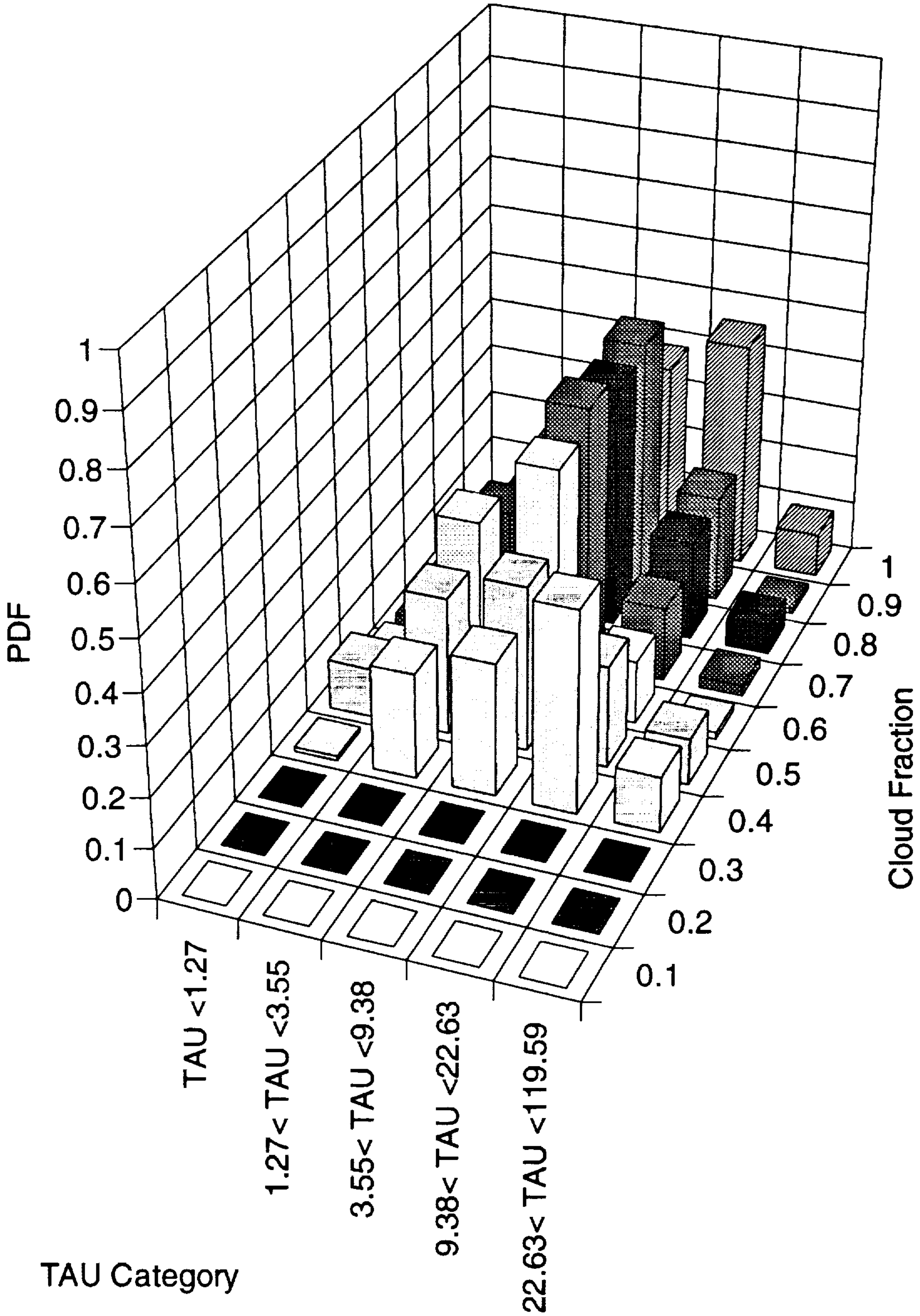

Figure 7.27 As in Fig. 7.26, except for box D.

8. TROPICAL RESULTS AND DISCUSSION

Paralleling Chapter 7, the monthly mean grid albedo values for July 1987 and 1988 are provided by the ERBE scanner data in Figures 8.1 and 8.2. The location of the boxes of individual study are also displayed on this map. As added information, the ERBE monthly mean outgoing long wave radiation (OLR) is provided to clearly identify the Intertropical Convergence Zone (ITCZ) in Figures 8.3 and 8.4. Again, the spatial averages of mean cloudy albedo are presented first followed by the probability distribution functions (PDF).

Spatial Averages

Area 1

Starting with the 1987 box A, just north of the ITCZ, it is evident from Figure 8.5 that mean cloud spherical albedo is independent of cloud fraction. This graph looks similar to box A on the western edge of the Pacific stratus region, Figure 7.5, except that here the albedo ranges from 0.10 to 0.37 rather than 0.20 to 0.45. The majority of cloudiness in both boxes includes broken cumulus type clouds with more numerous observations of lower cloud fractions in the tropical box. In the tropical box when cloud fraction exceeds 80%, albedo values are lower than the stratus area. The lower tropical albedo range may result from different microphysical properties like cloud droplet size and shape, but it is more probable that it results from the macrophysical influences of cloud geometry (Stephens and Greenwald 1991). Geometric influences are considered to range from a few kilometers to the resolution of the data. The geometric effect on albedo is stronger than it is on long wave radiation (Stephens and Greenwald 1991). The effect of microphysical properties is greatest when ice anvils are present at the higher cloud fractions.

Figures 8.6 through 8.8 profile the first, second and third level spatial averages around box A, (see Figure 5.3 for the included boxes). Figure 8.8 is the third ring average and continues to illustrate a lack of albedo dependence on cloud fraction for a cloud fraction range of 30% to 85%. The cloud fraction range condenses for the same reason as the cloud fraction range shrank for the stratus region. A single box, Figure 8.5, has a higher probability of extreme, high and low, cloud fractions occurring at any one time than does a large, regional average, Figure 8.8. By the third average, Figure 8.8, the albedo range condenses from a first level range of 0.15 to 0.40 to a range of 0.20 to 0.37. The changes in the lower and upper bounds can be explained in terms of a probability distribution. A mean albedo is associated with a region. A single box within the region is a representative sample and contains albedo values scattered about the mean. As more samples (boxes) are averaged together, the albedo values tend to cluster towards the actual mean albedo of the region. Since the averaging area around box A consists of about half and half of ITCZ and non-ITCZ boxes, the above explanation of albedo is functional. The lack of albedo dependence after a spatial average is in contrast to the relationship found for the stratus region box A. This observation implies that extreme albedo values of single boxes are well balanced by the opposite extreme. High albedos are averaged with low albedos for an essentially constant albedo range. In the atmosphere, one example is deep convective towers with high albedos being averaged with the surrounding environment where convection is inhibited.

The spatial averaging for the 1988 box A is depicted in Figures 8.9 through 8.12. The data follows the same trend as 1987 except that slightly thicker convective clouds are present in box A initially because of the higher albedos at 100% cloud fraction. As in the stratus region, further averaging beyond three levels does not change the range of albedo values appreciably.

Area 2

The second area under consideration is located in the heart of the ITCZ, (see Figure 5.4 for the boxes). For box B, Figure 8.13, the thick clouds of deep convection are easily distinguishable by the extremely high albedo values at 100% cloud fraction. When this box B is compared to the 1987 stratus region box B, Figure 7.6, the two graphs appear interchangeable. Thus, at visible wavelengths the cloudy albedo for this tropical and stratus box are the same in a statistical sense even though the dynamical forcing mechanisms are different between shallow stratus convection and deep tropical convection.

Figures 8.14 through 8.16 show the first, second and third level ring averages around box B. Notice how the albedo range shrinks before the cloud fraction range condenses. This is a result of the high variability in clouds across the ITCZ. Optically thick convective towers with high albedos are averaged with optically thin, low albedo, convective elements (detached anvils). Further averaging across the entire tropics' area, Figure 8.17, shrinks the cloud fraction range now more than the albedo range. This is caused by the influence of the less cloudy areas of the Atlantic subtropical high pressure cell being incorporated into the average. With an area this large, the probability of completely clear or partly cloudy scenes is low; thus, cloud fractions hover around 50%.

The same observation is visible for 1988. Figure 8.18 is the 1988 box B, while Figure 8.19 is the third ring average and 8.20 is the entire tropics' region. For the entire region graph, the cloud fraction averages 55% for 1987 and 58% for 1988, approximately the average global value for cloudiness. The mean cloudy albedo for both years averages to 0.32.

Probability Distribution Functions

Probability distribution functions (PDF) for the region provide further information on cloud properties.

July 1987

This time moving from a south to north direction, Figure 8.21 displays box B for 1987. Since this box is in the heart of the ITCZ, it is not surprising to have zero scenes with cloud fractions of 20% or less. This location is expected to have a bimodal distribution with the lower cloud fractions (30% to 60%) dominated by the lowest TAU categories and the higher cloud fractions dominated by the highest TAU categories. A bimodal peak does result for cloud fractions greater than 70%, but it is not as clear cut as expected. However, the thickest clouds occur with the highest cloud fraction. Previously, the albedo plot for this box appeared to match the stratus 1987 box B albedo plot in a statistical sense, (Figures 8.13 and 7.6). Comparing the PDF graphs, Figures 8.21 and 7.22, shows the dissimilarities of the two locations. The stratus area favors medium optically thick clouds across all cloud fractions while the tropics depicts both optically thick and thin clouds. It is no wonder then why GCM's (which assume plane parallel stratus clouds) lower albedo values to represent inhomogeneities in marine stratocumulus clouds (Cahalan et al. 1993).

Box C is still within the ITCZ, but it is at the edge of an area of strong, deep convection. Figure 8.22 illustrates a shift towards the middle TAU Category. Although the bars at 20% and 30% cloud fraction are the highest, this is a result of there being few scenes with cloud fractions that low. Again for all cloud fractions, there is an across the board increase in the probability of the two highest TAU categories.

Box D and box A are located just outside and ten degrees of latitude outside the ITCZ, respectively. Using the albedo graph, Figure 8.5, as a guide, all cloud fractions should shift towards the lower TAU values representing clear scenes, cumulus clouds or thunderstorm anvil blowoff. Figure 8.23 depicts box A and displays the expected shift towards the lower TAU categories while Figure 8.24 depicts box D and a continued shift towards the lowest TAU category.

July 1988

Figures 8.25 through 8.28 illustrate the same boxes from south to north for 1988. Box B, Figure 8.25, shows the bimodal peaks again for cloud fraction greater than 70%. The clustering in the low TAU category is probably due to thunderstorm anvils. Like box C from 1987, Figure 8.22, the 1988 box C, Figure 8.26, displays a shift towards the middle TAU category. The low cloud fractions are being influenced by a low number of scenes which makes the probability of a particular cloud fraction division and TAU category large. The thickest clouds still occur at the highest cloud fractions of 90% and

100%. The shift towards the two lowest TAU categories is not as strong for the 1988 box A, Figure 8.27, as it is for the 1987 box A, Figure 8.24. The 1988 box is located closer to the border of the ITCZ (using the 270 Kelvin contour) rather than just outside it. For box D, Figure 8.28, lower cloud fractions tend to have the thinnest clouds.

Discussion

While the results from the tropics are not easy to describe as a cohesive unit, there are parallels that can be made to the stratus region. For instance, the tropical 1987 box A, Figure 8.9, has similar characteristics to the stratus region box A, Figure 7.5. Both imply albedo is independent of cloud fraction. However, the PDF graphs, Figures 8.23 and 7.21 are different. The tropical box favors the second TAU category while the stratus box favors the middle TAU category. The lower average tropical albedo value of 0.26 compared to the stratus albedo value of 0.37 accounts for the different TAU distributions. If another box, say E (see Figure 8.1 for location), is chosen even further outside the ITCZ, a data trend similar to both A boxes is expected with lower cloud fraction being more numerous. In fact, this is the case, (see Figure 8.29). Thus, for locations outside the ITCZ, the principles of Coakley and Kedem, et al. mentioned in the marine stratocumulus discussion section apply for individual boxes.

For a location within the ITCZ, the tropical box B matches the stratus box B in a statistical sense. Both boxes capture optically thick clouds at 100% cloud fraction. The stratus box can be thought of as individual high liquid water cores growing into a layer of clouds and then forming an even larger core of liquid water. The tropical box encloses an area of strong and deep convection surrounded by weaker convection and or thunderstorm anvils. Since different dynamical forces are at work for both boxes, it is difficult to devise a method for determining subgrid scale variations. And, neither of the theories proposed by Coakley and by Kedem, et al. work well for these box B locations.

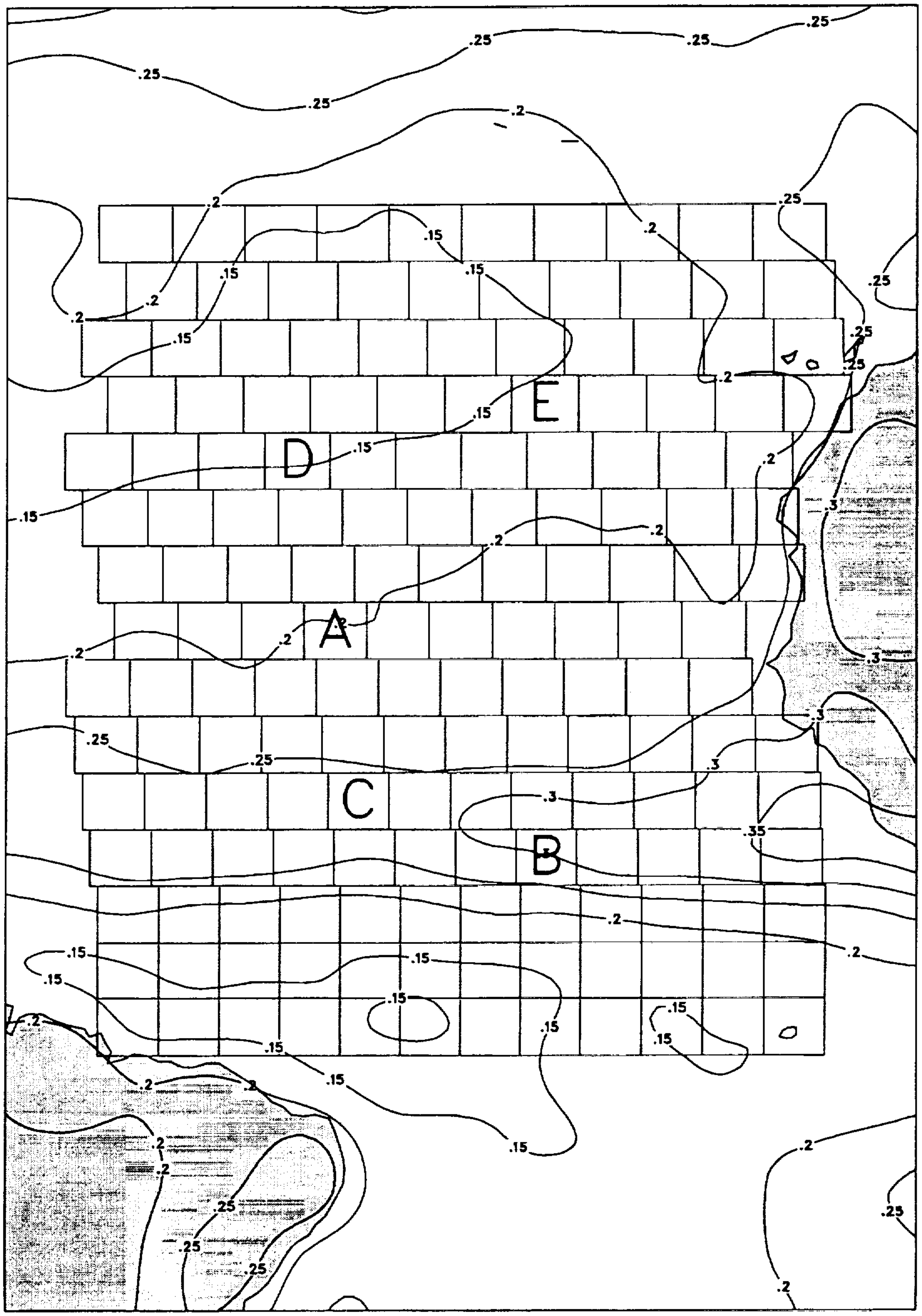

Figure 8.1 ERBE July 1987 monthly mean spherical albedo and the location of individual boxes of study.

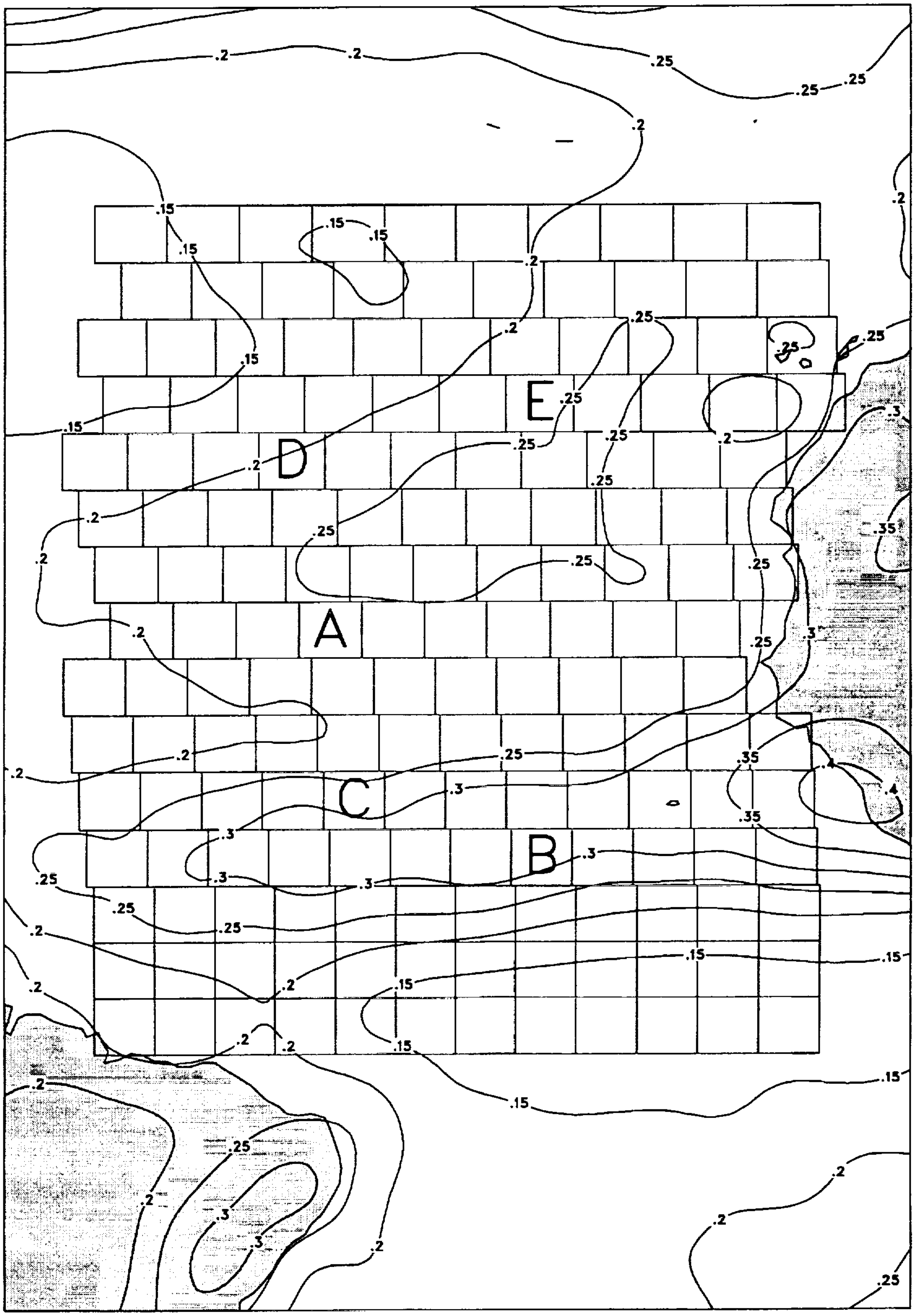

Figure 8.2 ERBE July 1988 monthly mean spherical albedo and the location of individual boxes of study.

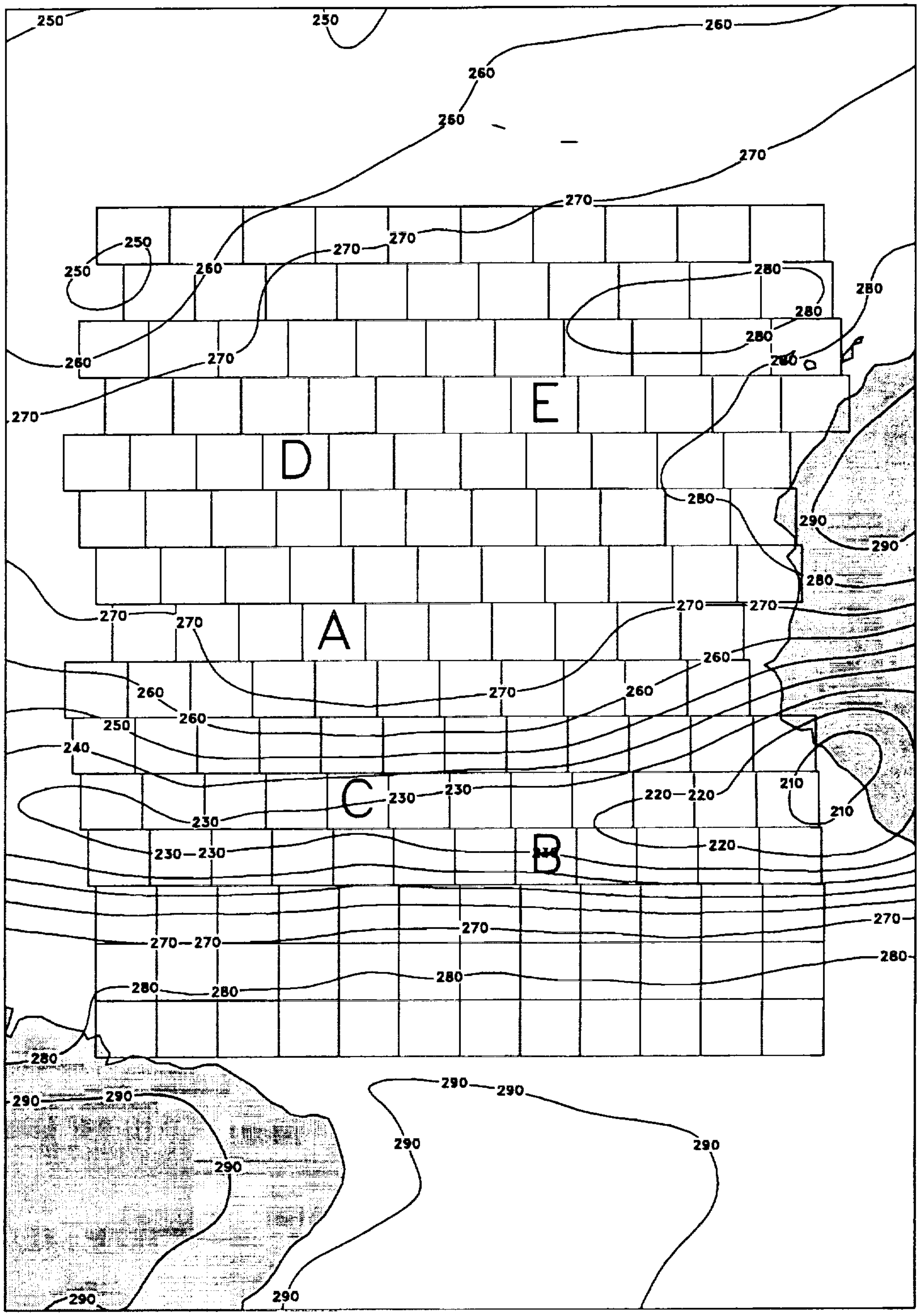

Figure 8.3 ERBE July 1987 monthly mean outgoing long wave radiation (OLR).

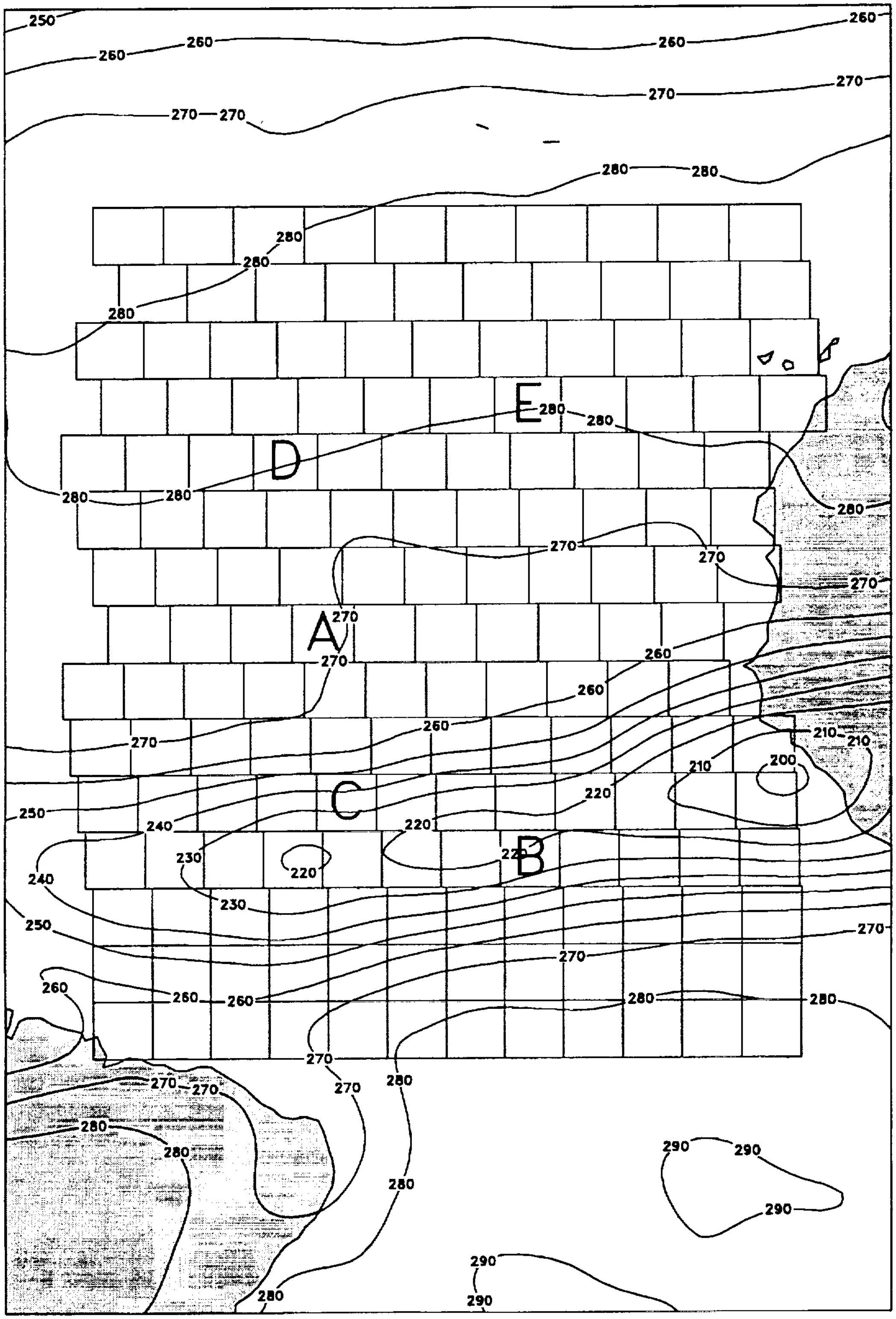

Figure 8.4 ERBE July 1988 monthly mean outgoing long wave radiation (OLR).

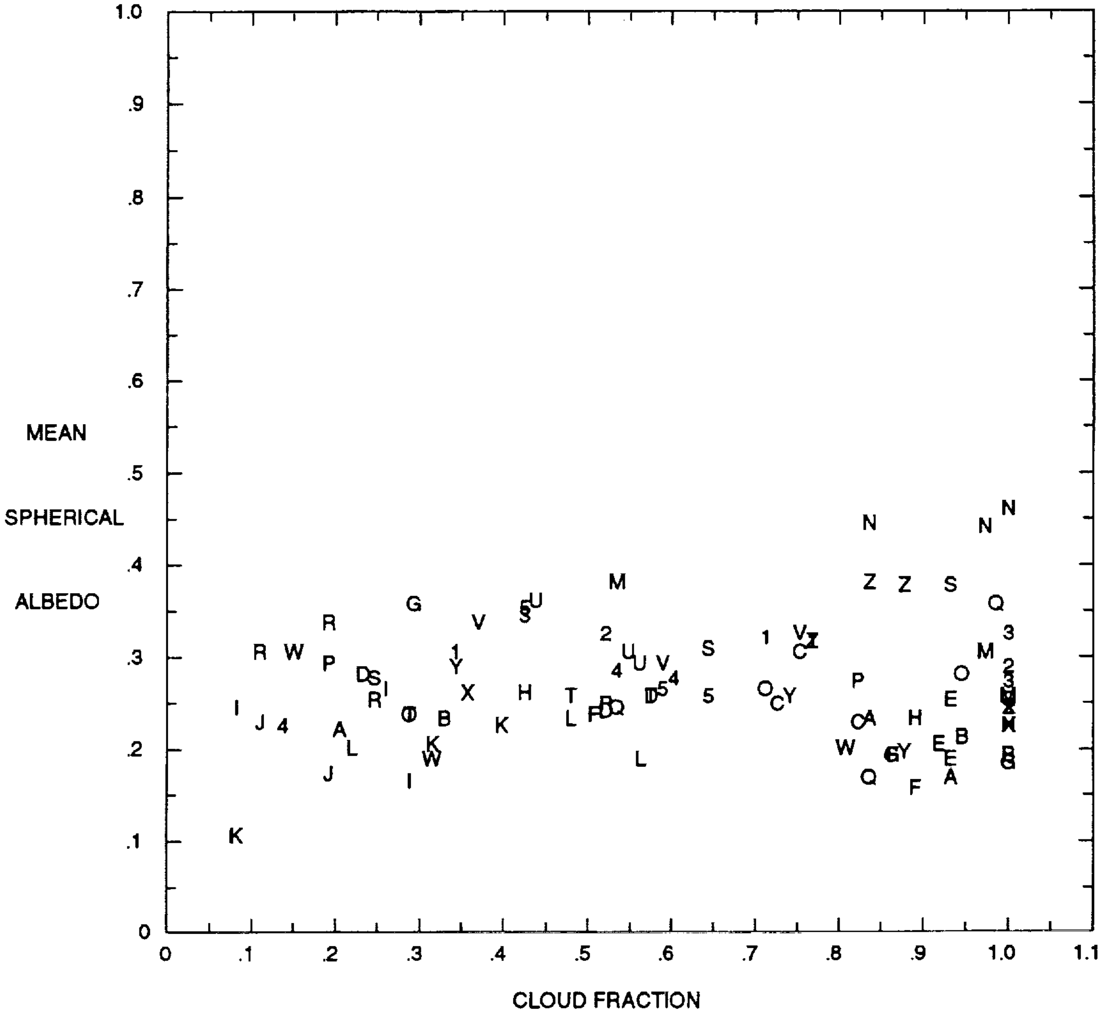

Figure 8.5 July 1987 mean spherical albedo versus cloud fraction for box A.

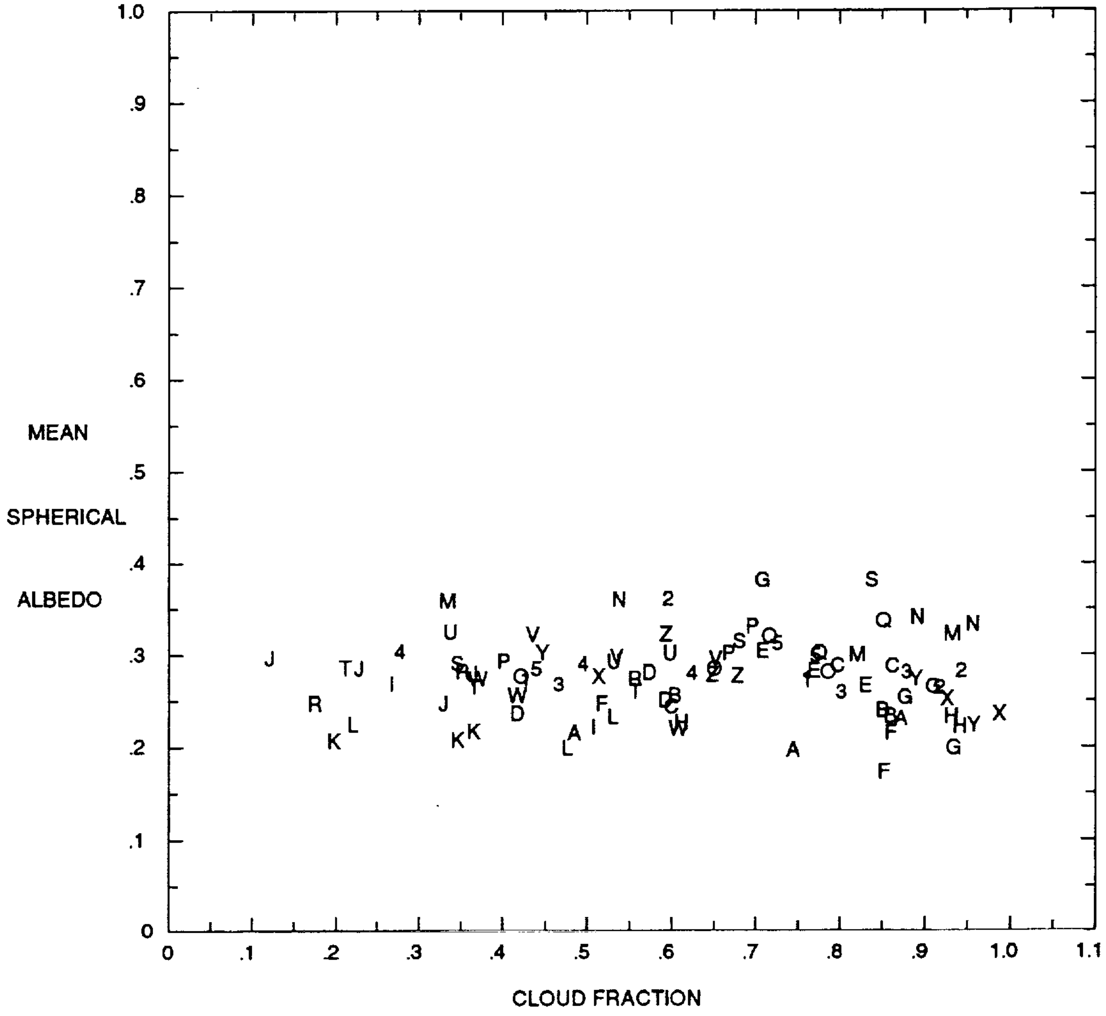

Figure 8.6 July 1987 mean spherical albedo versus cloud fraction for the first ring around box A.

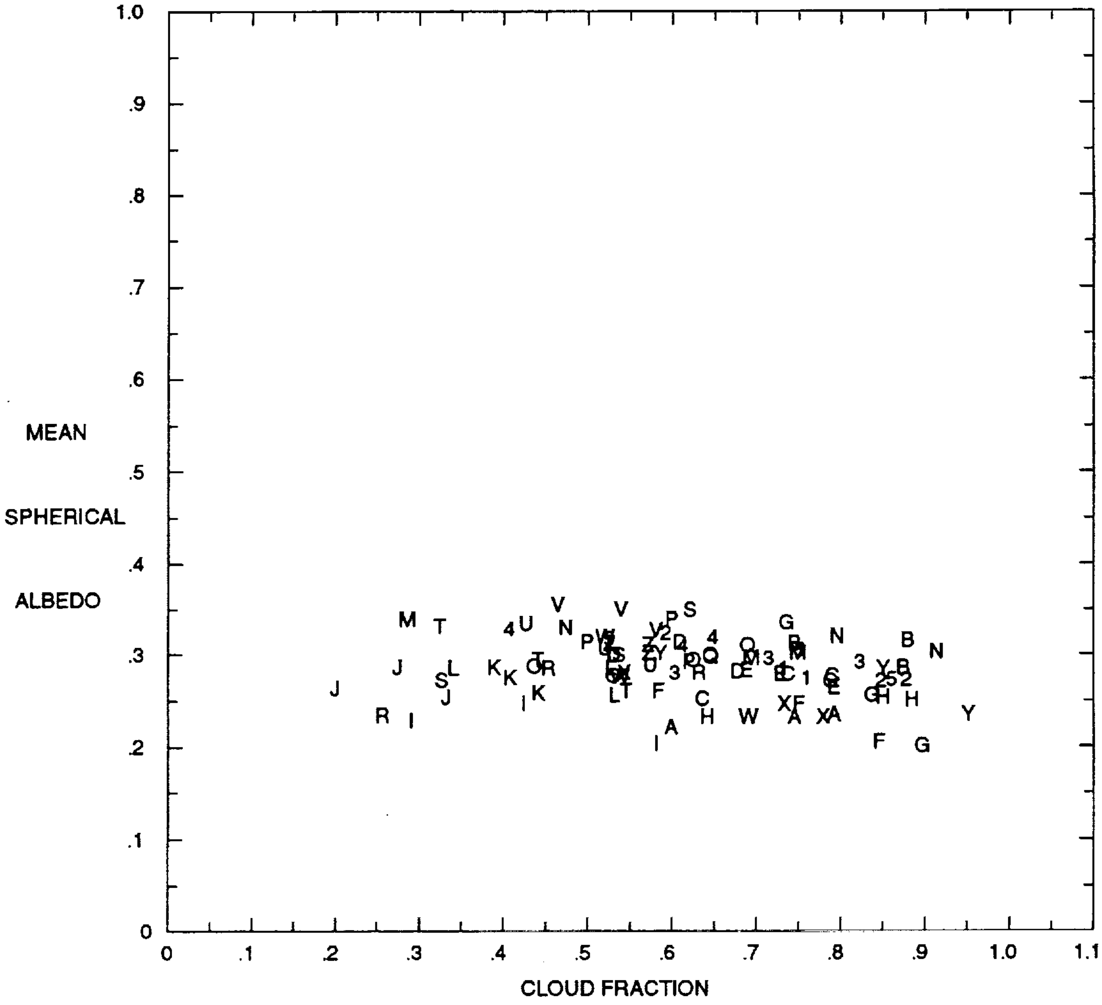

Figure 8.7 As in Fig. 8.6, except for the second ring around box A.

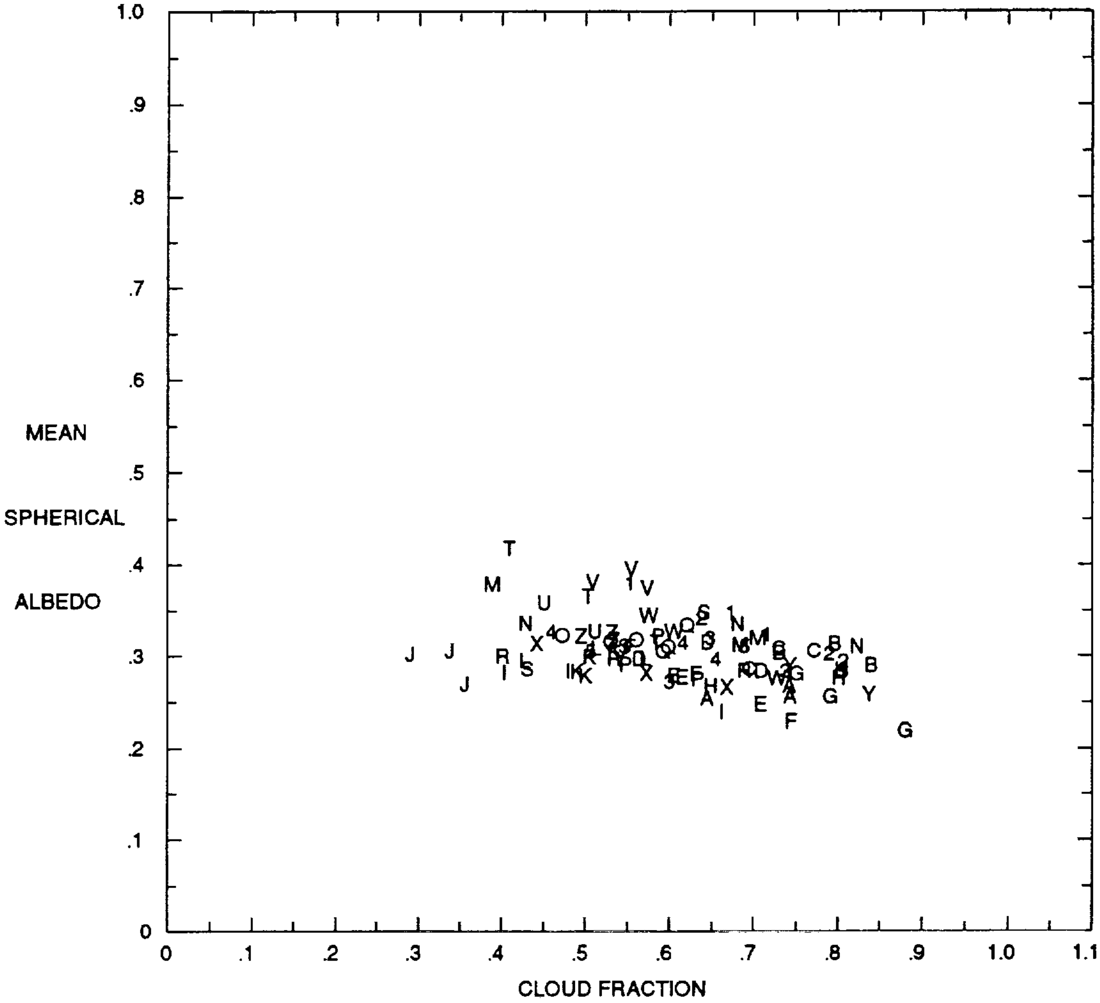

Figure 8.8 As in Fig. 8.6, except for the third ring around box A.

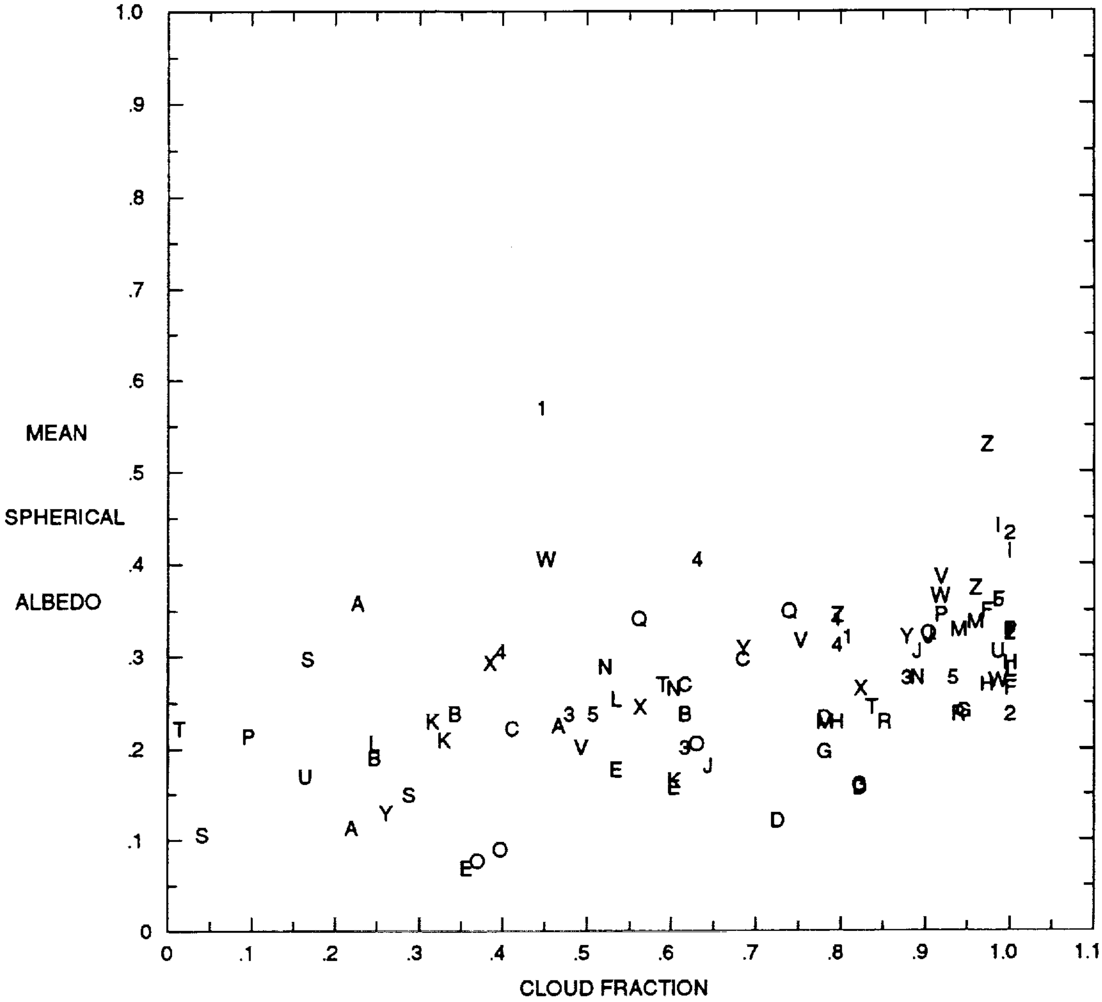

Figure 8.9 July 1988 mean spherical albedo versus cloud fraction for box A.

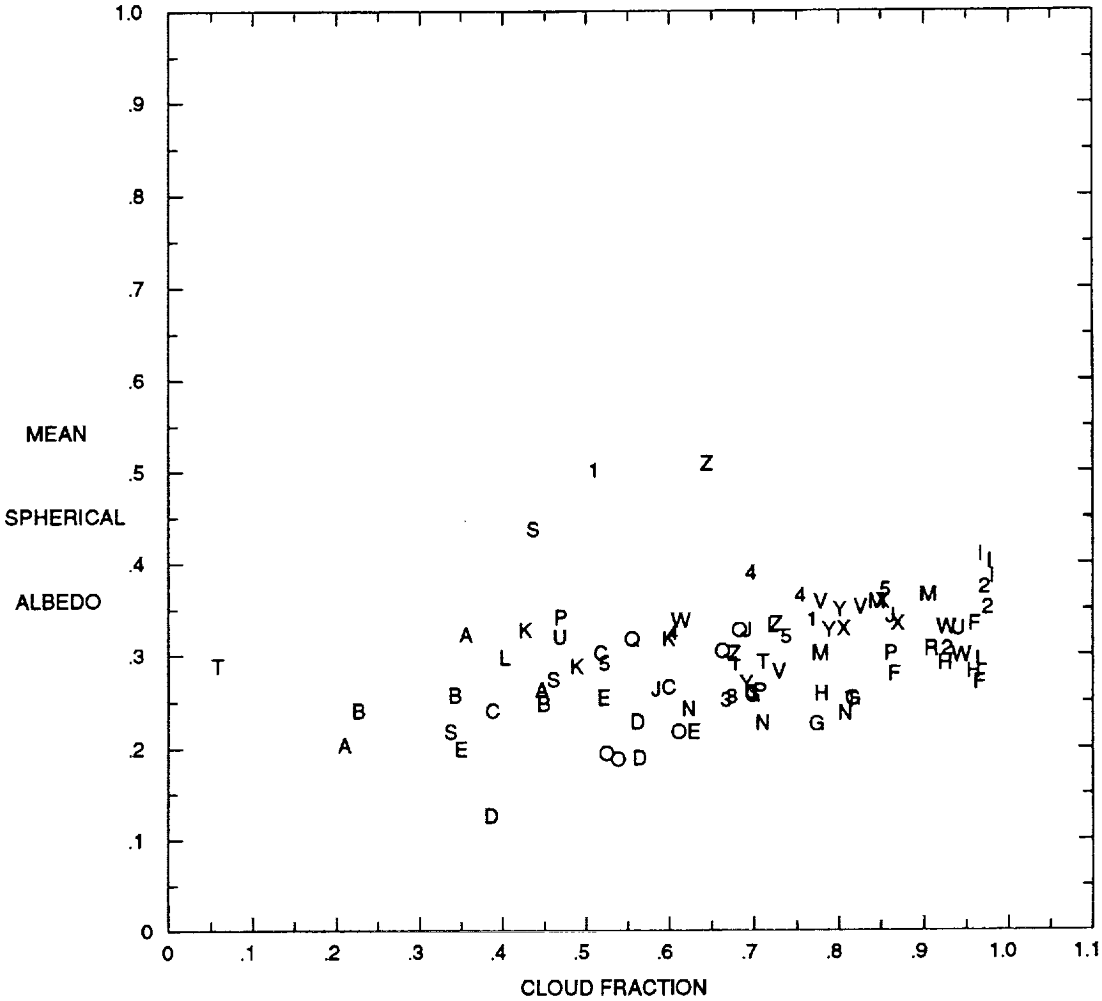

Figure 8.10 July 1988 mean spherical albedo versus cloud fraction for the first ring around box A.

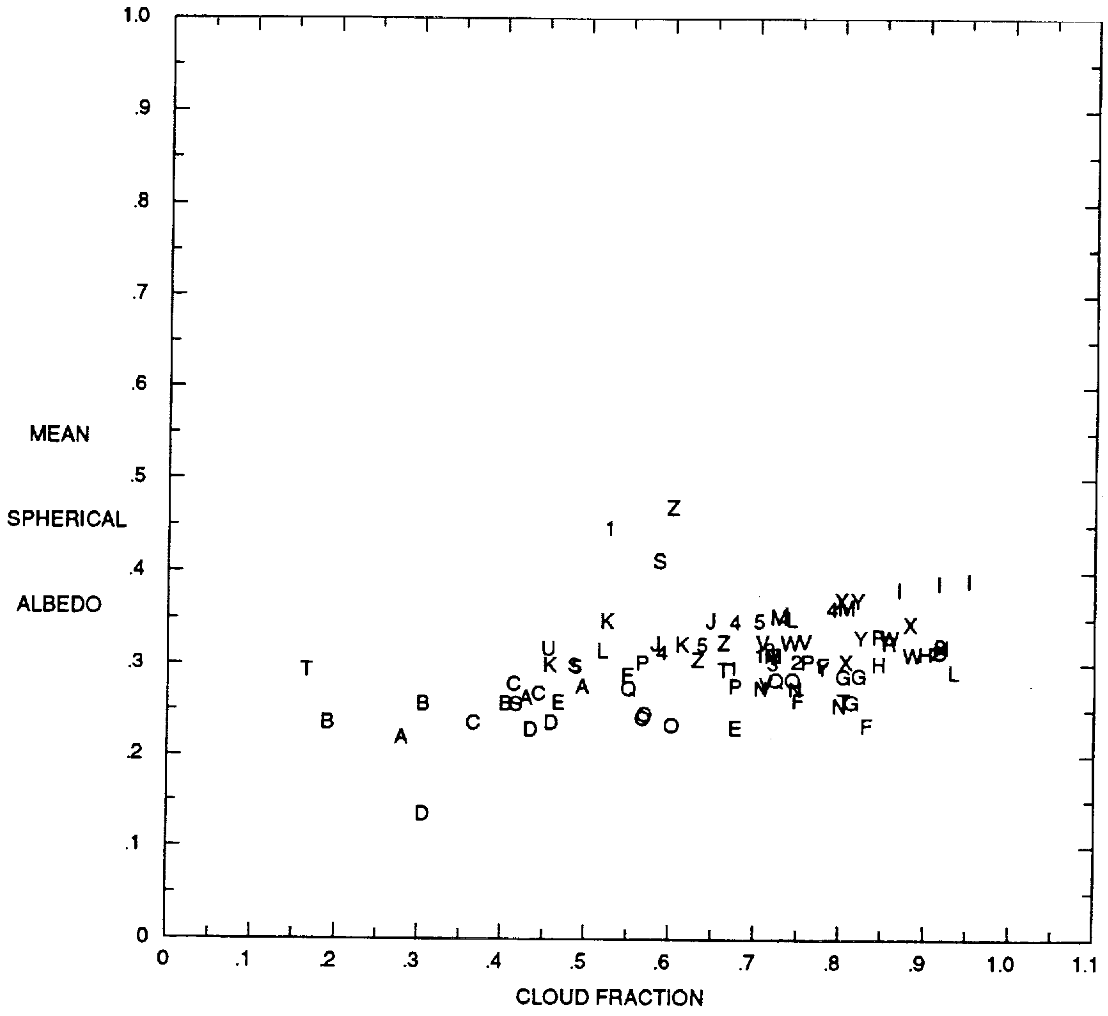

Figure 8.11 As in Fig. 8.10, except for the second ring around box A.

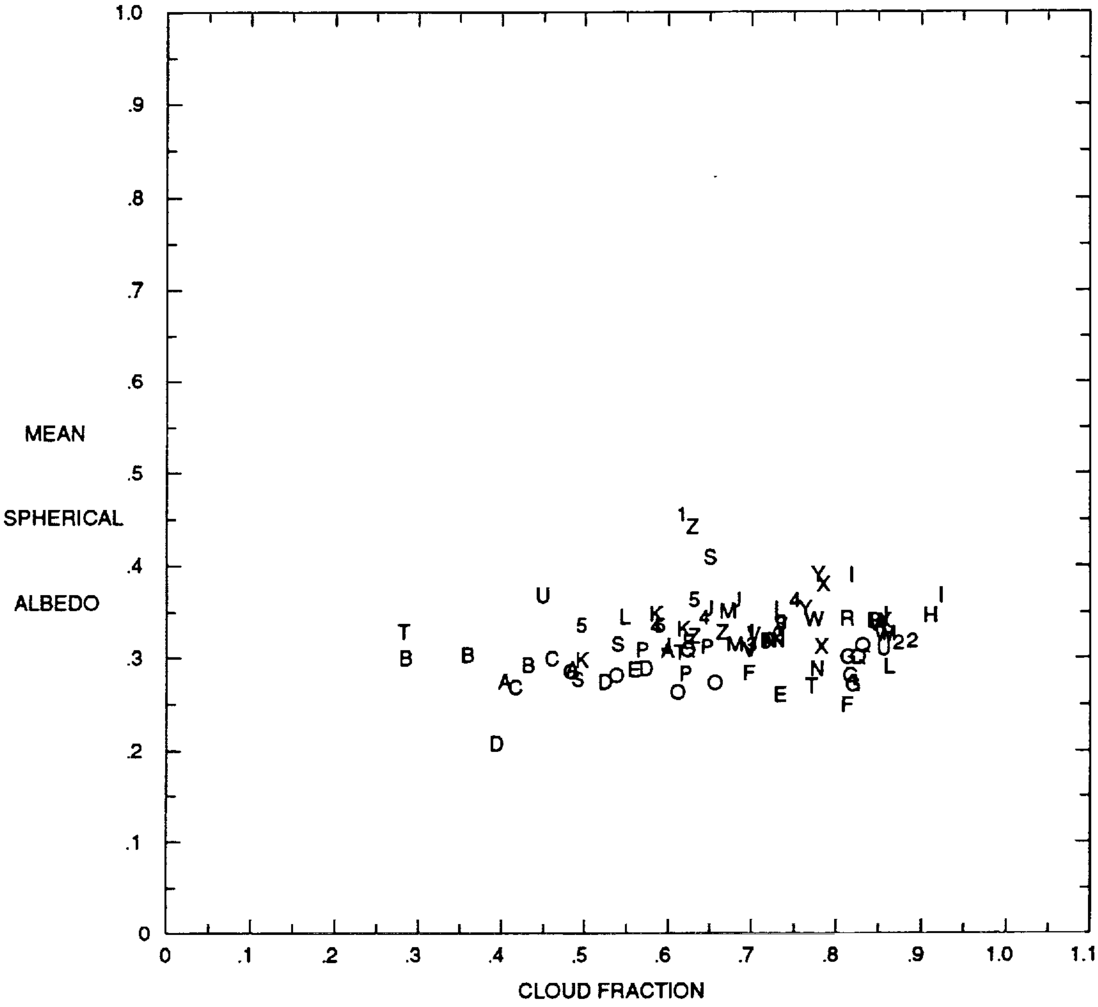

Figure 8.12 As in Fig. 8.10, except for the third ring around box A.

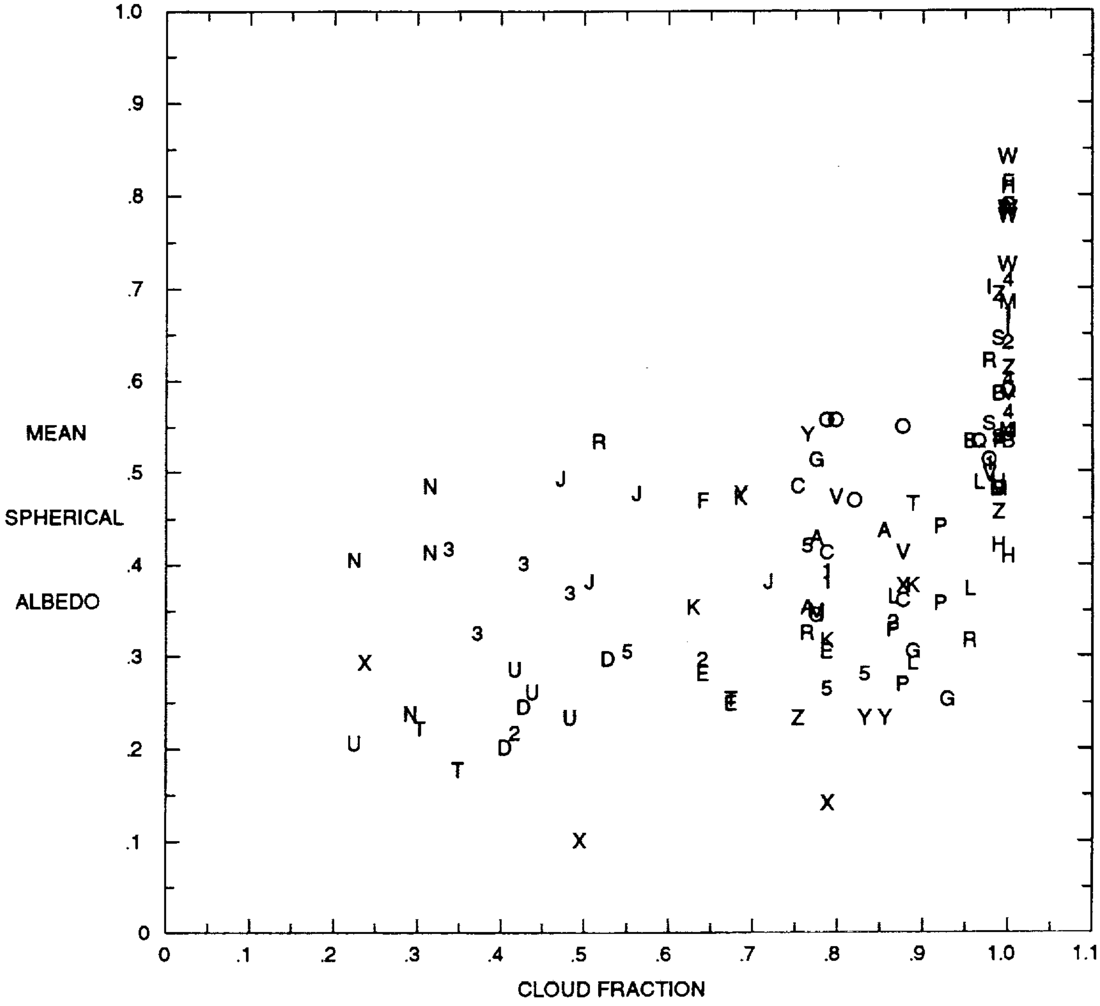

Figure 8.13 July 1987 mean spherical albedo versus cloud fraction for box B.

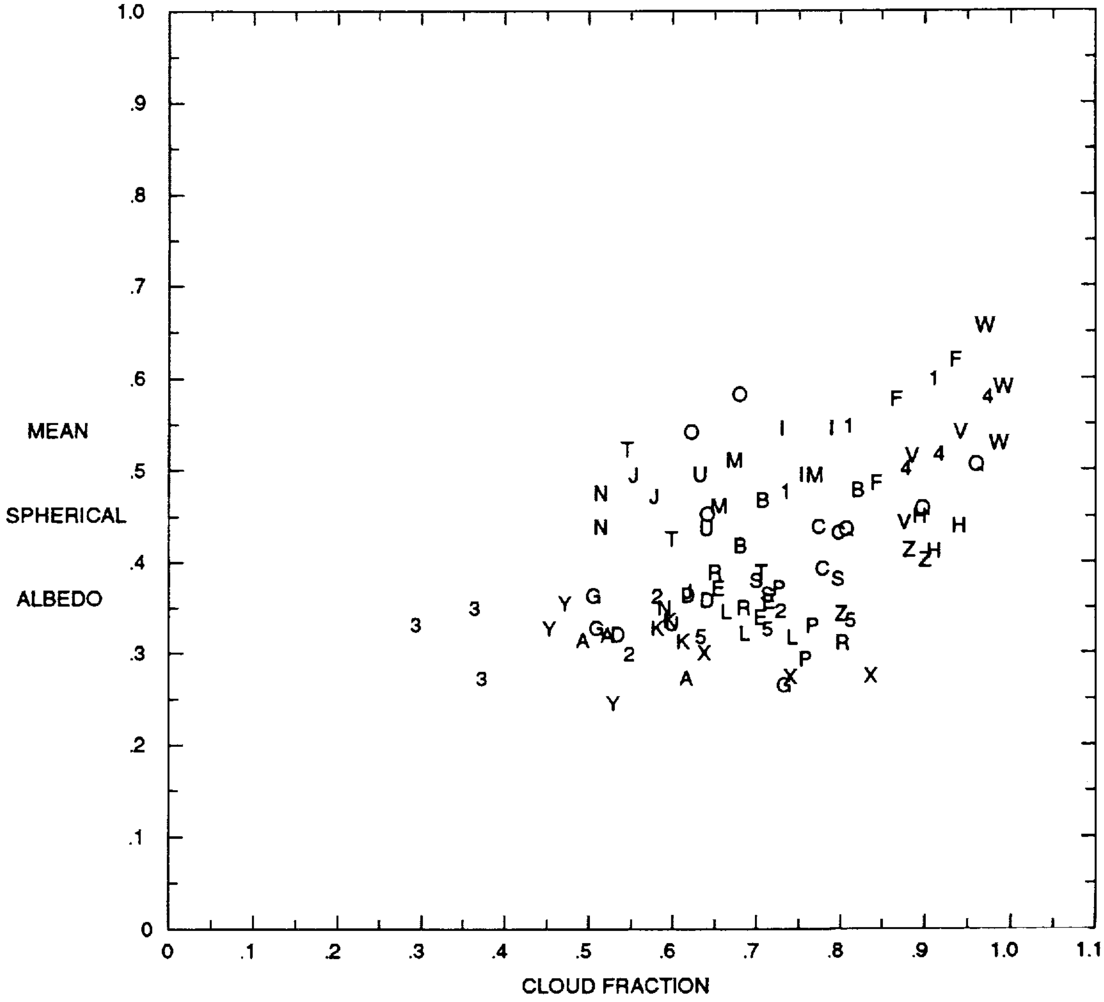

Figure 8.14 July 1987 mean spherical albedo versus cloud fraction for the first ring around box B.

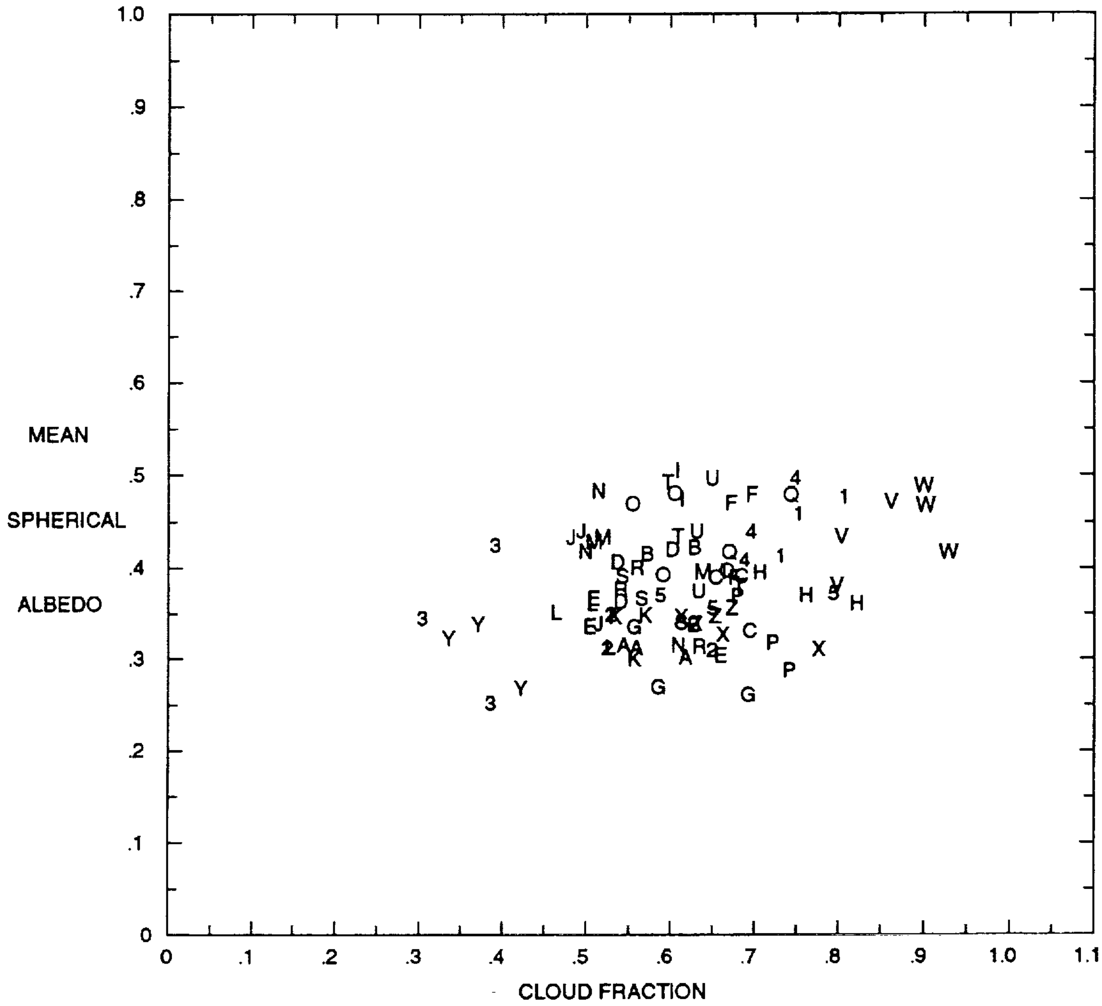

Figure 8.15 As in Fig. 8.14, except for the second ring around box B.

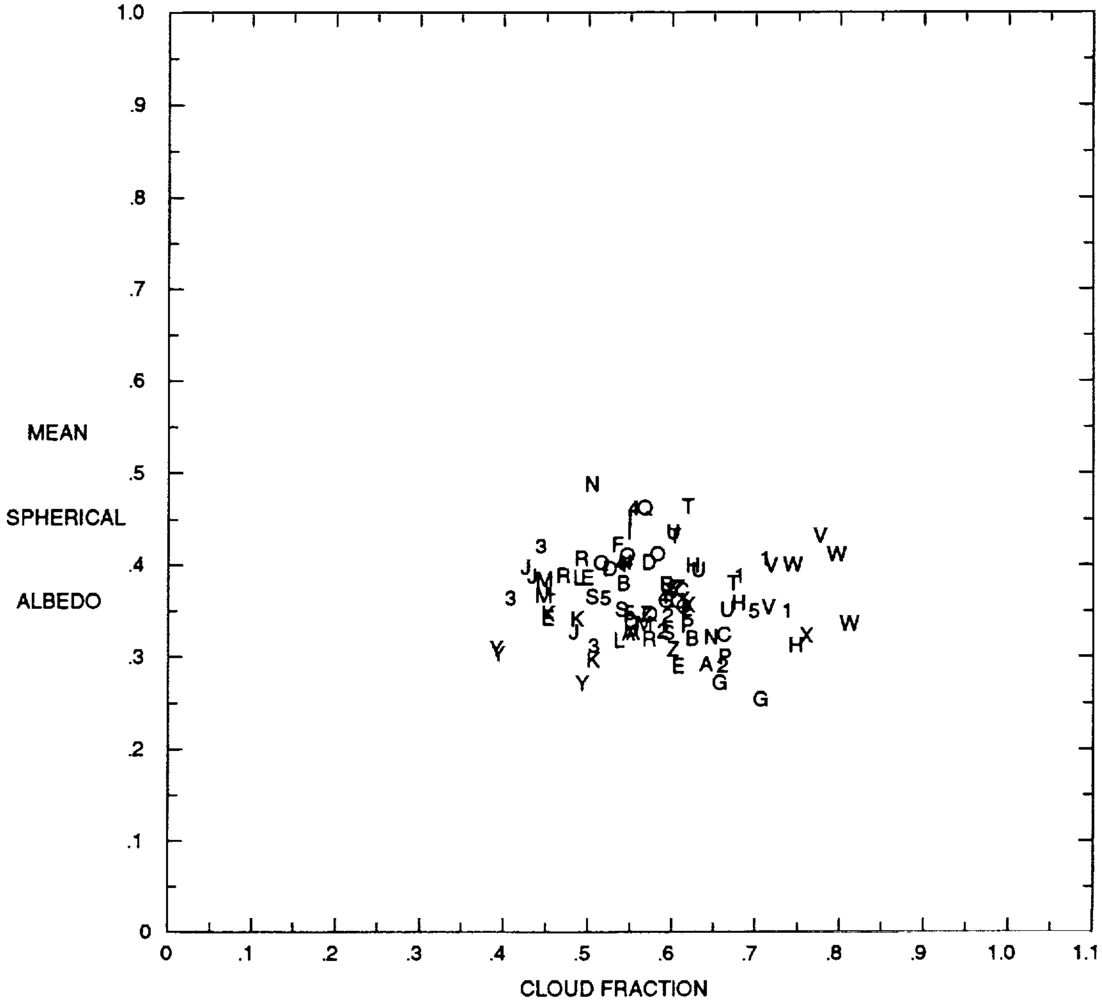

Figure 8.16 As in Fig. 8.14, except for the third ring around box B.

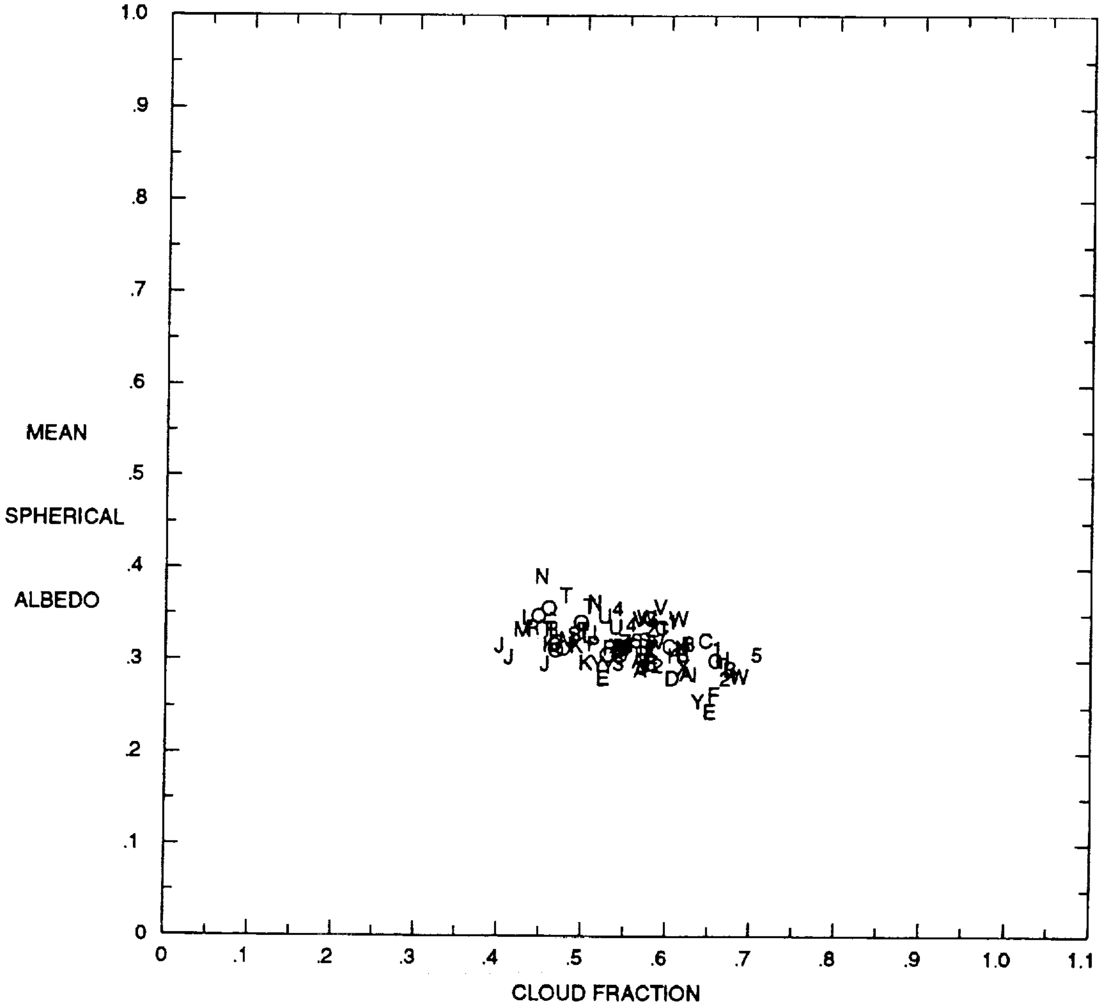

Figure 8.17 July 1987 mean spherical albedo versus cloud fraction for the entire tropic region.

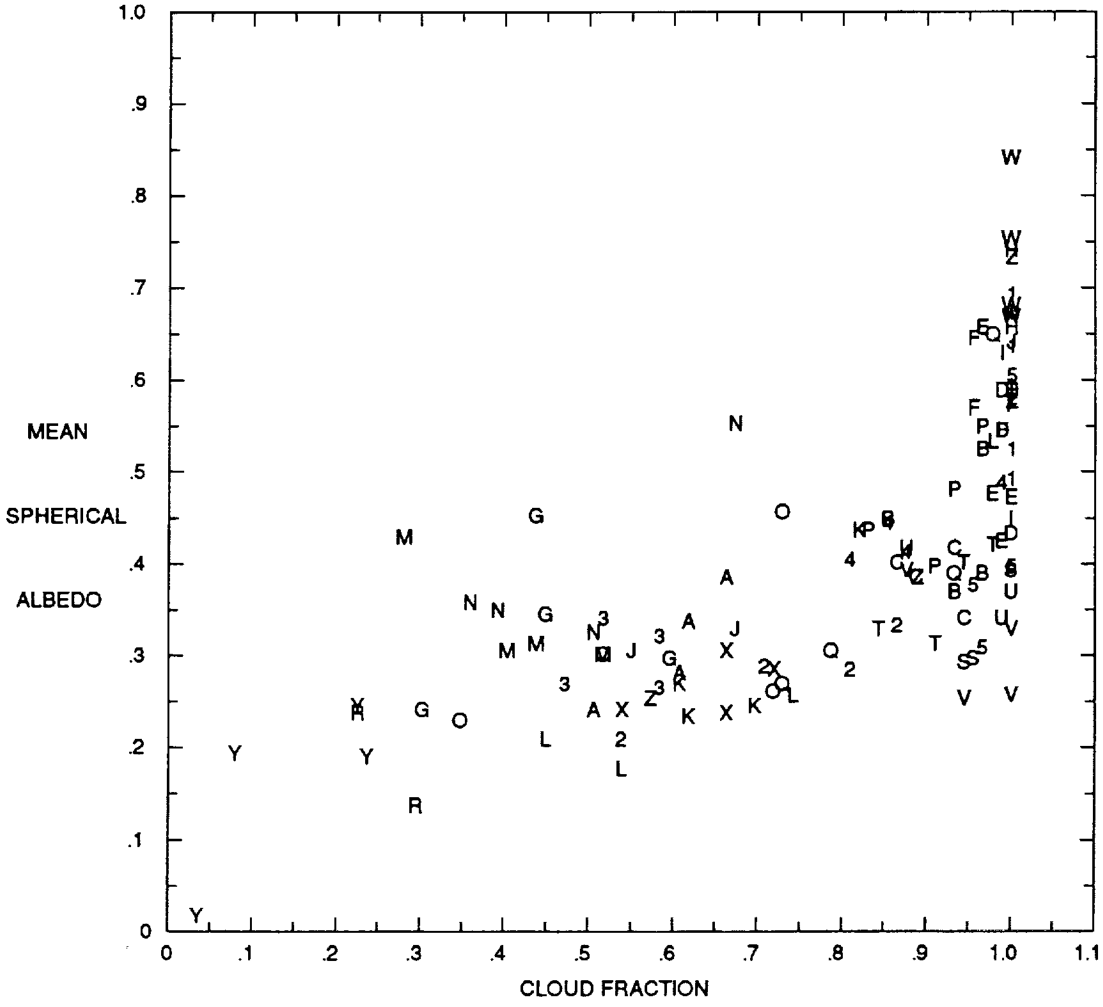

Figure 8.18 July 1988 mean spherical albedo versus cloud fraction for box B.

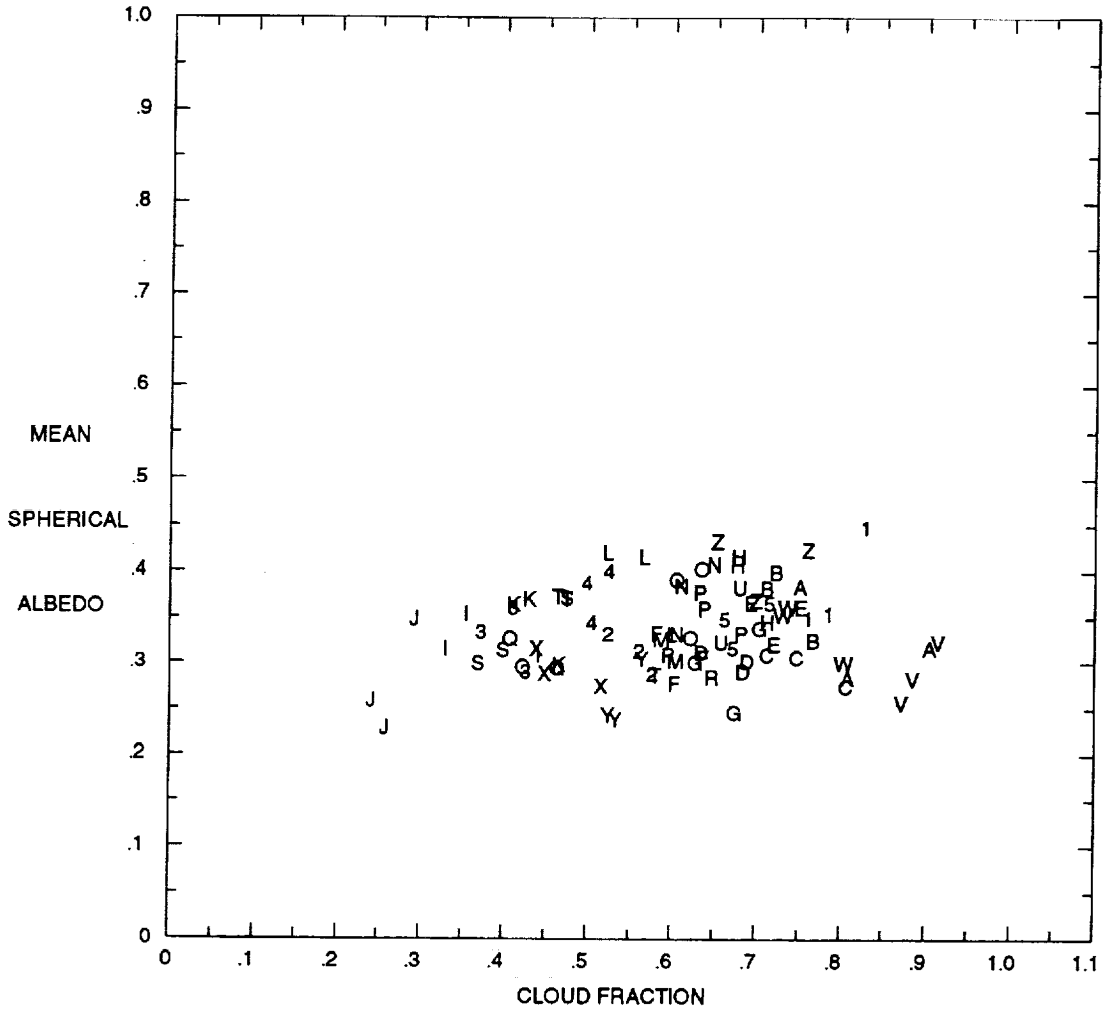

Figure 8.19 July 1988 mean spherical albedo versus cloud fraction for the third ring around box B.

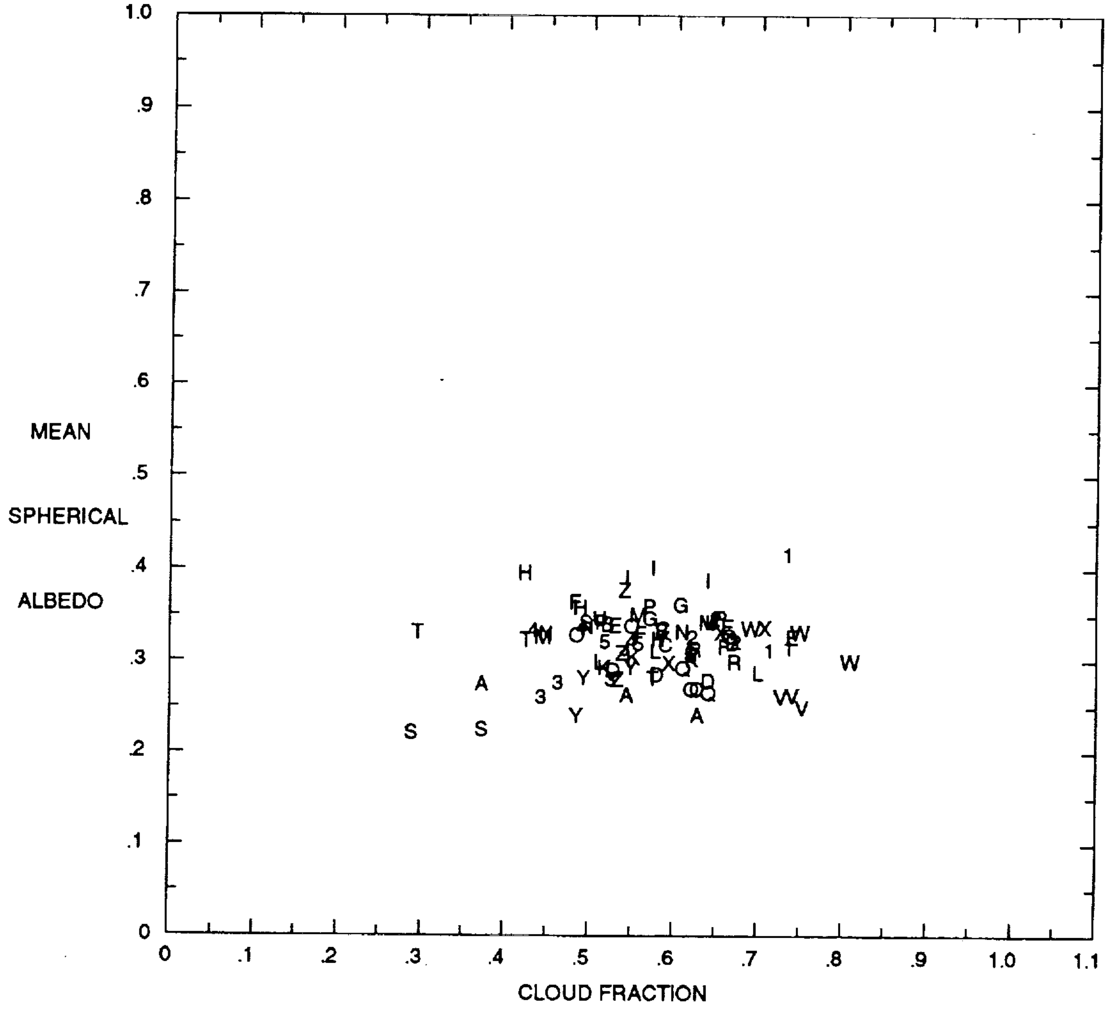

Figure 8.20 July 1988 mean spherical albedo versus cloud fraction for the entire tropic region.

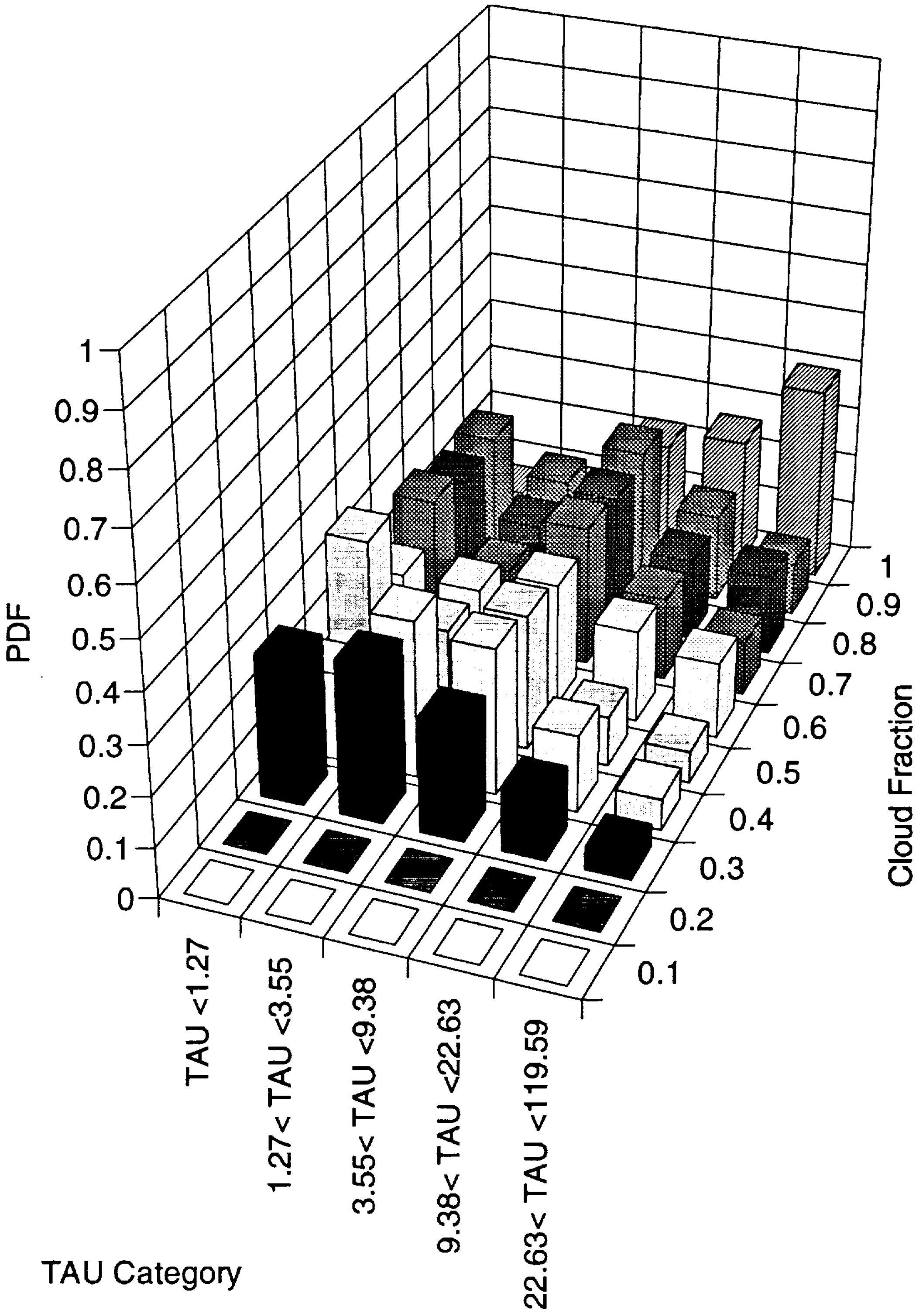

Figure 8.21 The probability distribution function (PDF) with respect to cloud fraction for box B, July1987.

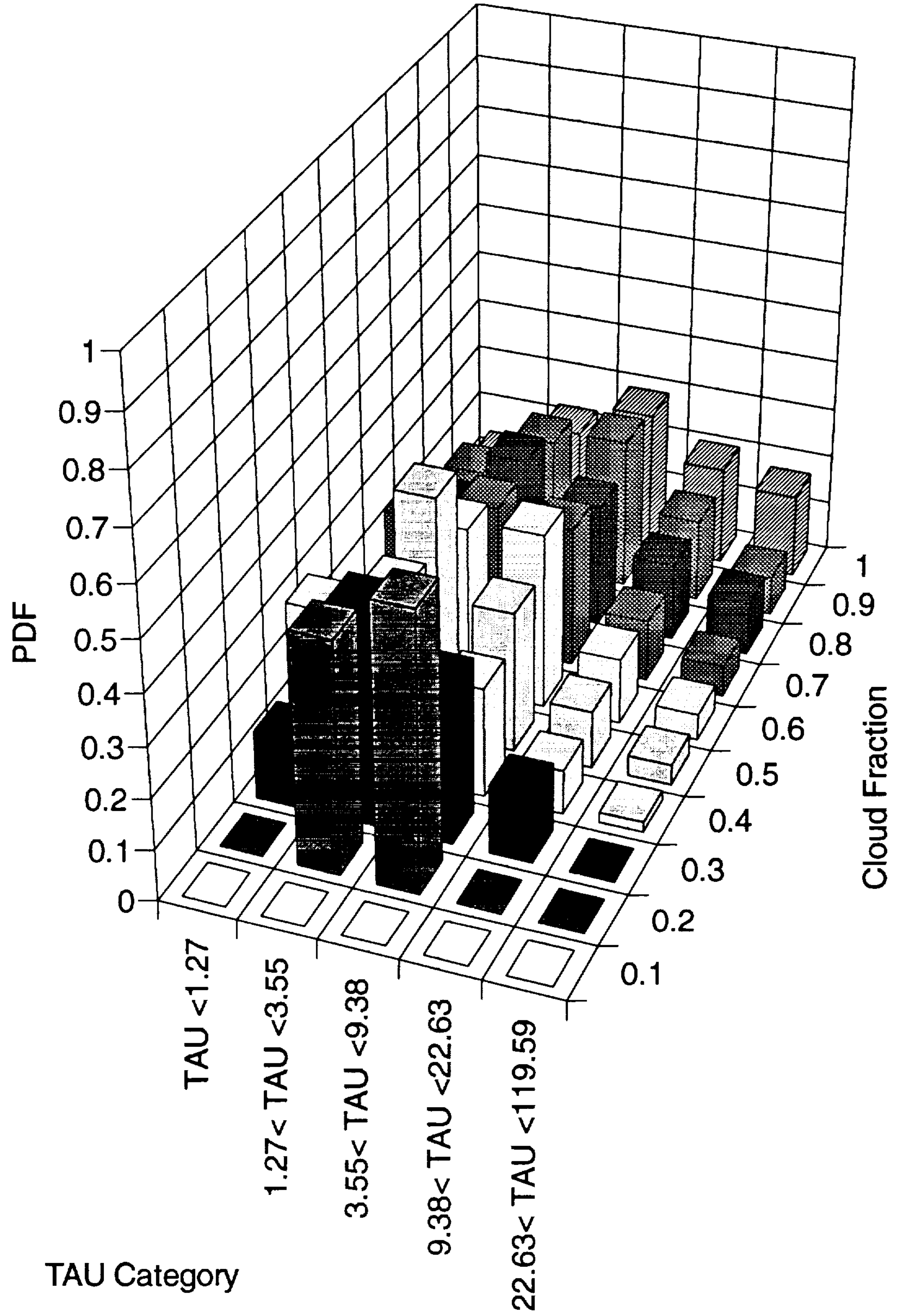

Figure 8.22 As in Fig. 8.21, except for box C.

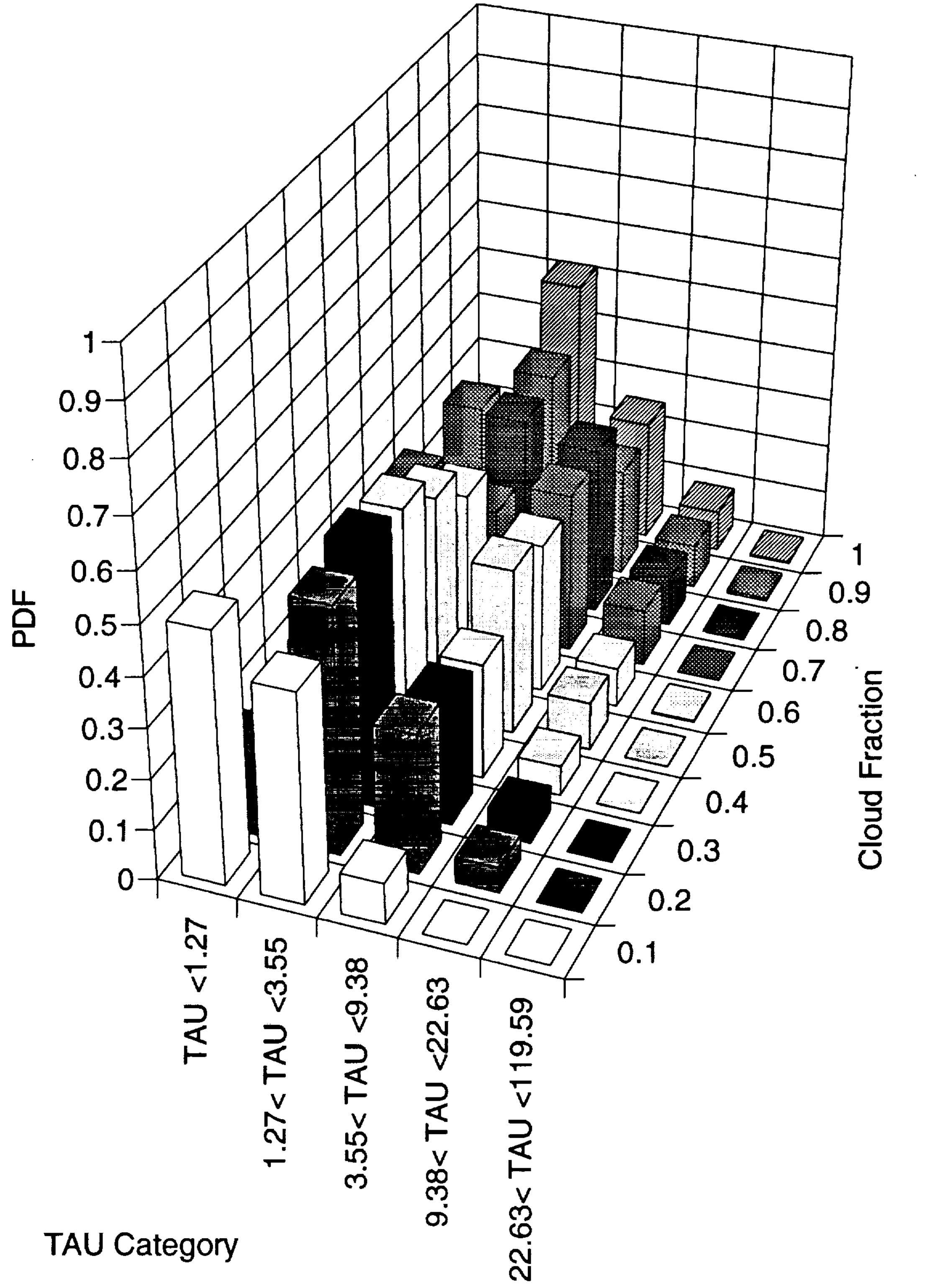

Figure 8.23 As in Fig. 8.21, except for box A.

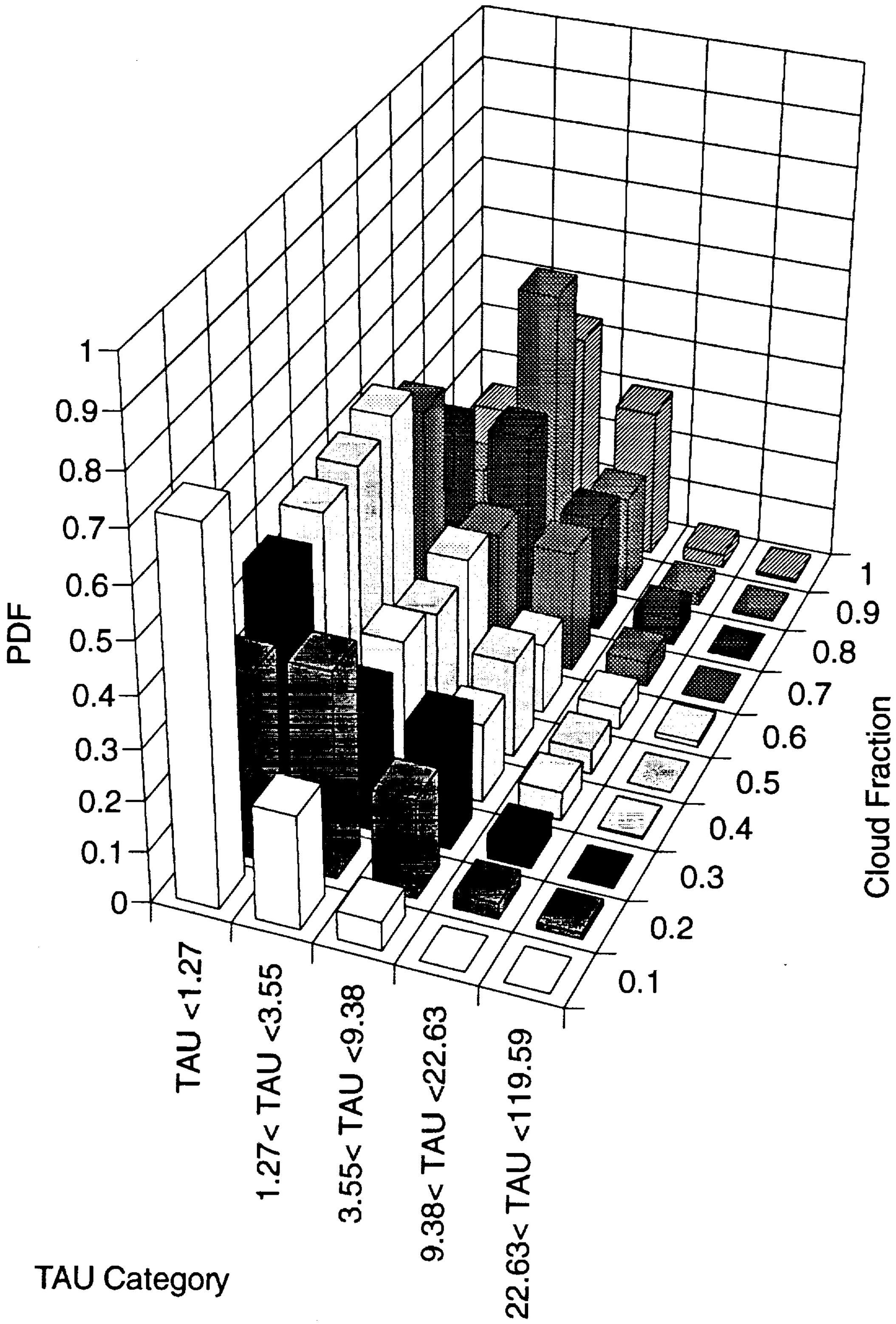

Figure 8.24 As in Fig. 8.21, except for box D.

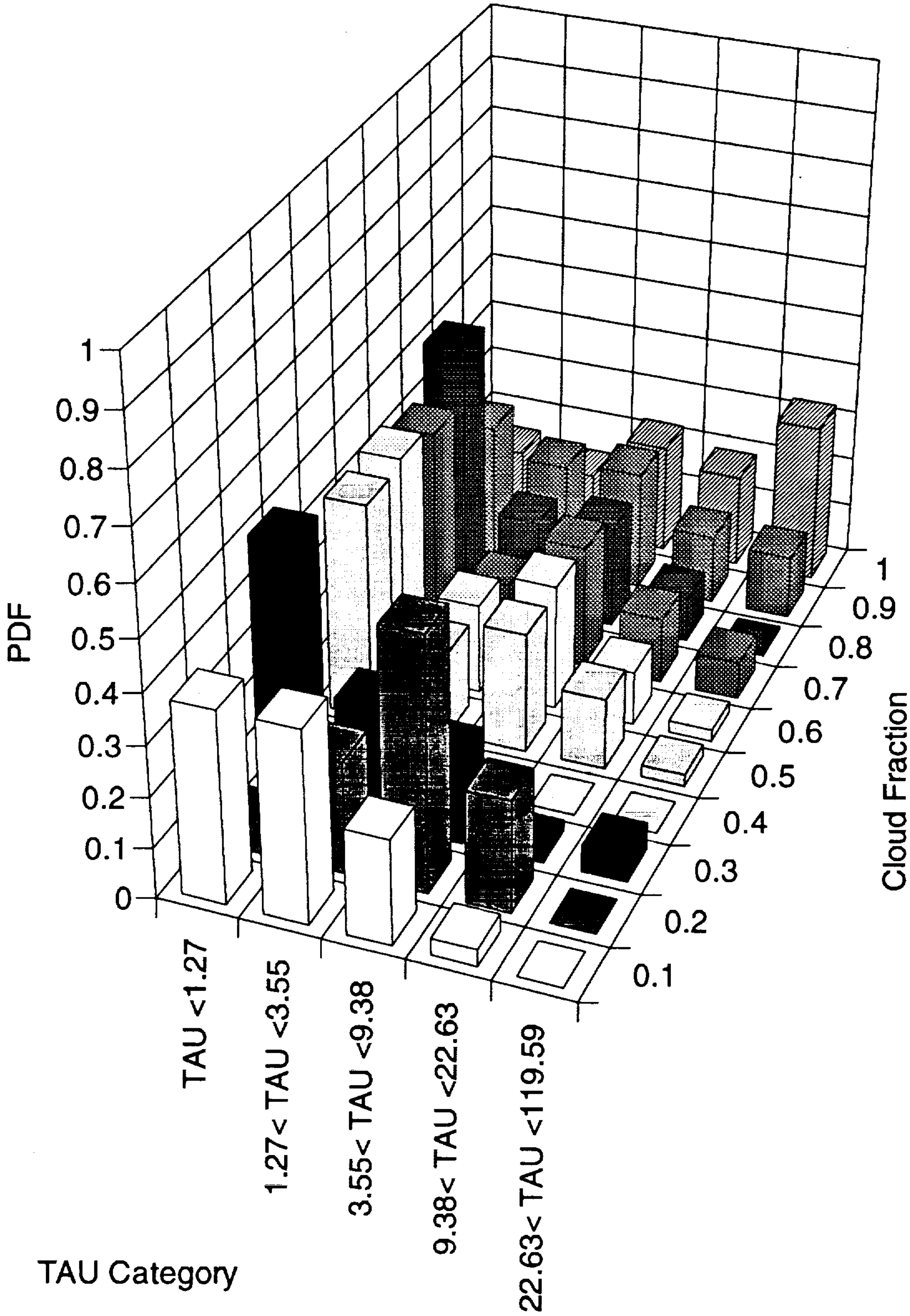

Figure 8.25 The probability distribution function (PDF) with respect to cloud fraction for box B, July 1988.

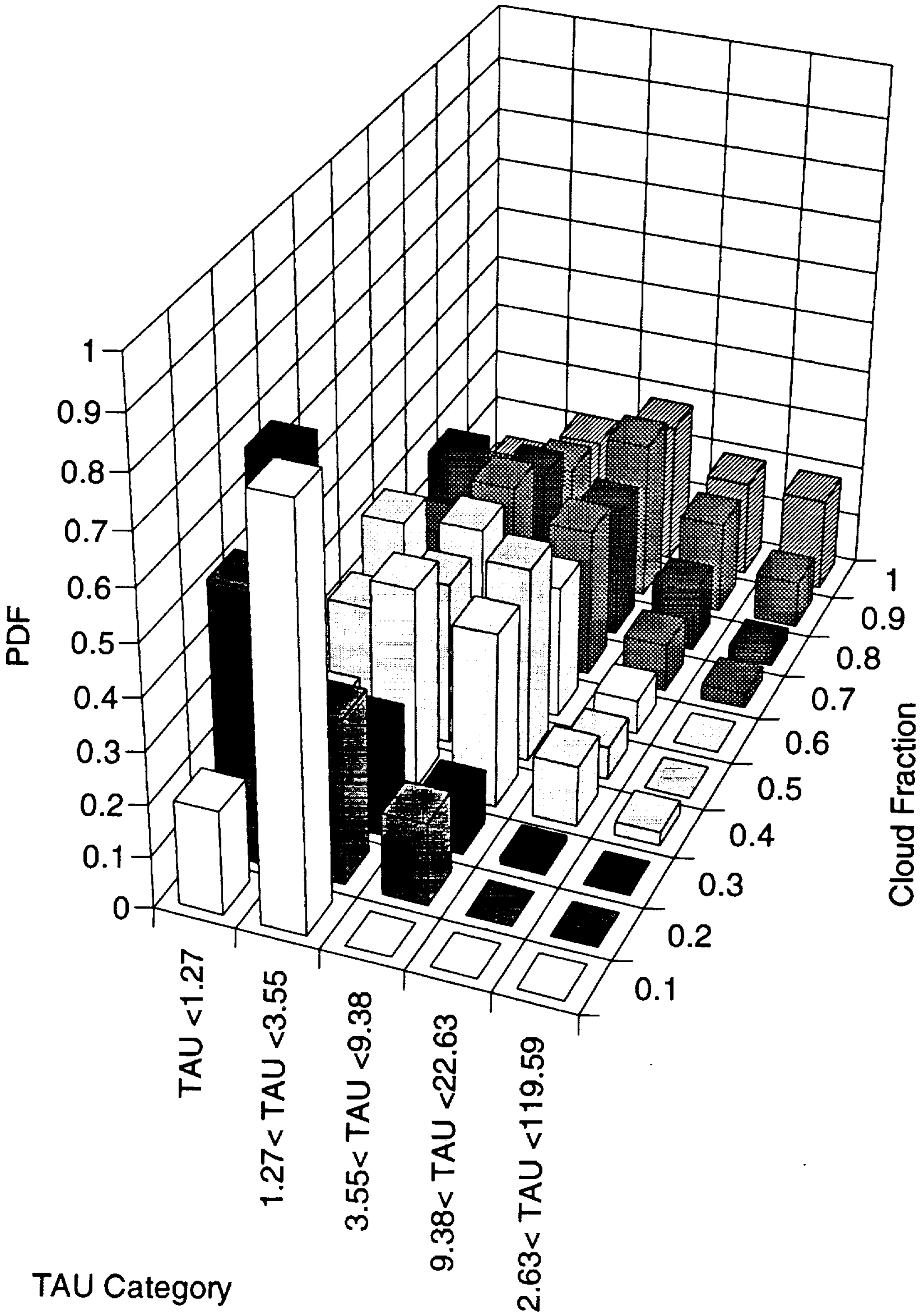

Figure 8.26 As in Fig. 8.25, except for box C.

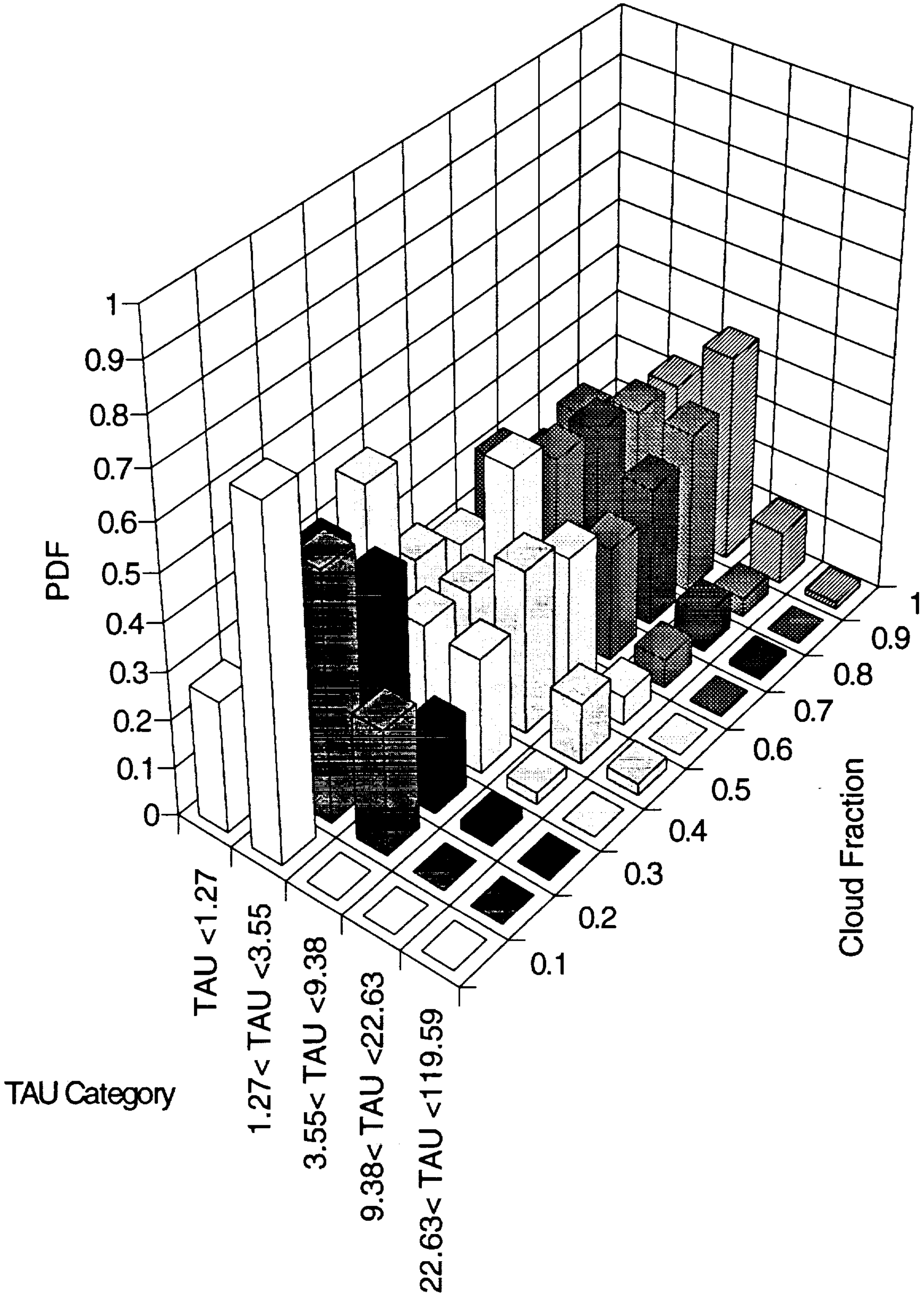

Figure 8.27 As in Fig. 8.25, except for box A.

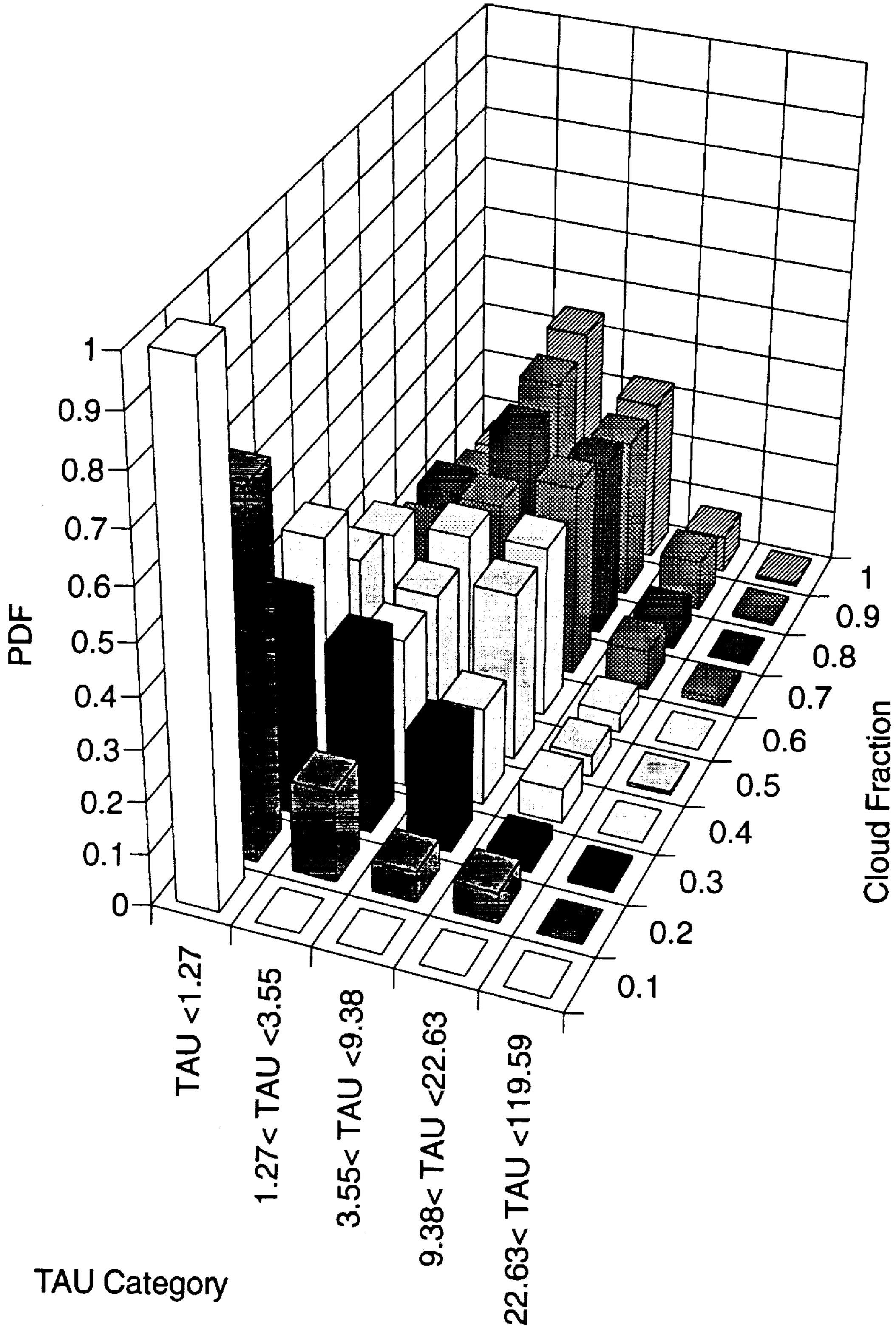

Figure 8.28 As in Fig. 8.25, except for box D.

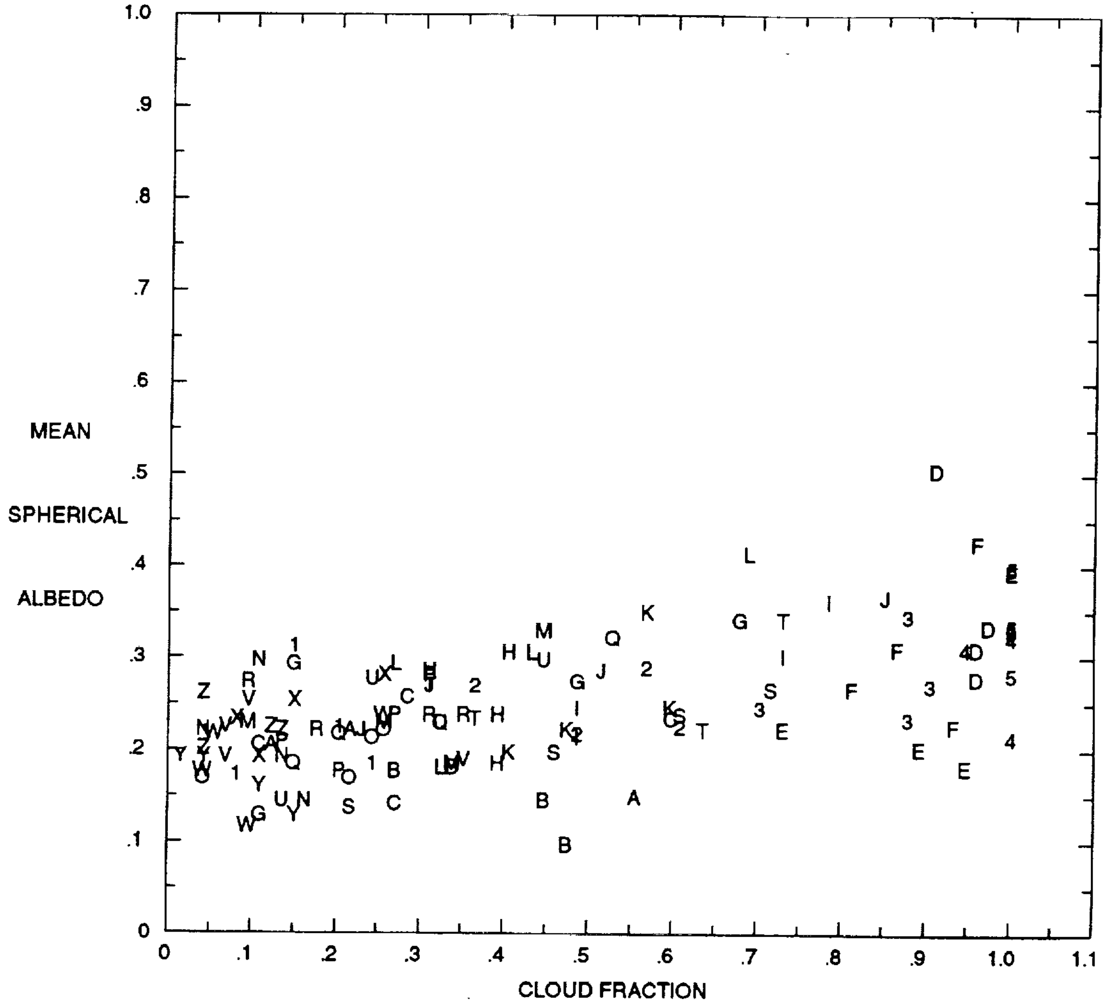

Figure 8.29 July 1987 mean spherical albedo versus cloud fraction for box E.

9. SUMMARY AND CONCLUSIONS

Comparisons between ISCCP satellite data and the hypotheses of Coakley (1991) and Kedem, et al. (1990) has been conducted for July 1987 and 1988. The goal of the study was to provide information for modeling subgrid scale cloud properties in order to supplement GCM grid-scale parameterizations. For the comparison, the variables of mean cloudy spherical albedo, cloud fraction and mean optical depth were used. Two different areas, marine stratocumulus off the coast of California and the tropical Atlantic, were the focus of the study.

To begin, a satellite and GCM framework for cloudiness was established. The satellite framework consists of pixels of approximately 4 to 8 km within an equal area grid box O(100 km). For cloudiness, the pixel radiance or brightness temperature exceeds a threshold in either the visible (0.63μm) or infrared (11μm). In a GCM, stratiform clouds exist according to a supersaturation criterion and convective clouds are parameterized. Then radiative transfer calculations are weighted by the cloud fraction.

The next step was to compare the satellite observations to the theories of Coakley and Kedem, et al. Coakley suggests the average visible reflectance of broken clouds is about 80 to 85% of the same clouds when layers are formed. He then proposes an idealized cloud model to explain this phenomenon. Clouds contain cores O(1 km) of high liquid water content and large droplet size surrounded by edges O(100 m) of low liquid water content and small droplet size. Kedem, et al.'s theory applied to modeling surface hydrology in a GCM. He concluded that a linear relationship exists in a statistical sense between area-averaged rain rate and fractional area of rain in convective systems. Kedem, et al.'s idea can be applied to GCM cloud radiative properties because of similar parameterization problems.

The results of the comparison between satellite observations and the above two theories in the stratus and tropical region were described. First, individual boxes were studied followed by averages over several grid boxes. For low-level, single layer marine stratocumulus clouds, mean cloudy albedo was invariant for cloud fractions of 20% to 80%. Coakley's model described above and displayed in Figure 1.2 portrays cloud structure, while Kedem, et al.'s linear relationship related the total volume of liquid in a box to cloud fraction. Kedem, et al.'s theory was considered to be a first order approximation to subgrid-scale variability. Cloud fraction (wetted area for rainfall) can be estimated from mean cloud properties (mean precipitation rate) of the cloudy (precipitating) area. Equation (8) calculates mean cloudy LWP and equation (9) determines cloud fraction. Although, his theory may be difficult to implement because a history of LWP is non-existent, it outlines a method for GCM LWP computations to be independent of cloud fraction. Therefore, in the future, it may be possible to differentiate between grid mean properties that occur under different climatic conditions.

For individual boxes in the tropics, but outside the ITCZ, albedo was also found to be independent of cloud fraction. Therefore, the ideas mentioned in the previous paragraph were applicable. For boxes within the ITCZ, neither Coakley's or Kedem, et al.'s theories were found to hold. Thus, the use of ISCCP data to determine relationships between regional mean cloudy albedo and GCM parameterizations was successful. For boxes in the tropical and stratus regions where albedo was independent of cloud fraction, cloud structure was explained by Coakley's theory and LWP was determined by the radiation equivalent of Kedem, et al.'s theory, equation (9).

A regional scale spatial average of albedo and cloud fraction was conducted next to determine if a relationship exists between these two variables and if the above two theories apply. A linear relationship resulted for the stratus area, while no relationship was determined for the tropics. The direct relationship for the stratus area was accounted for by the inclusion of numerous completely overcast scenes being averaged together. For the tropics, cloudy albedo values were found to average to 0.32, approximately the mean spherical albedo of the entire Earth. Since albedo failed to remain independent of cloud fraction, neither Coakley's or Kedem, et al.'s theories applied. In terms of supplementing grid-scale GCM parameterizations, it was concluded that GCM's must account for the areal extent over which clouds are resolved.

Besides albedo, the distribution of optical depth was also examined. For the marine stratus clouds, a 3.55 to 9.38 optical depth range was favored across all cloud fractions. Such a distribution supported the observations of albedo being independent of cloud fraction and the applicability of Coakley's theory. When locations had many completely overcast scenes, albedo was not always independent of cloud fraction because once a cloud fraction of 100% was reached increased thicknesses increased albedo.

A parallel between the stratus area and tropical boxes outside the ITCZ was found. The tropical boxes had a data trend similar to the stratus locations but lower albedos and hence lower TAU values. Locations within the ITCZ had albedo values that were the same statistically as overcast boxes in the stratus region. Upon examination of the TAU distribution, the fact of different forcing mechanisms was clearly evident in the lower TAU values for the tropics.

Ideally, the distribution function of TAU would allow for the calculation of LWP through equation (8). It would have been beneficial if ISCCP provided LWP values. It is suggested that if future studies wish to calculate LWP, use the finer resolution B3 radiance data set of ISCCP directly. The information presented in this study may be used to conduct climate change experiments in order to provide for cloud fraction feedback mechanisms. The results may also be used to verify cloud models by providing an alternate calculation of cloud fraction, or LWP, as a check on model parameterizations. Eventually, it may even be possible to differentiate between grid properties of open cell and closed cell convection.

LIST OF REFERENCES

LIST OF REFERENCES

Agee, E.M., 1987: Mesoscale cellular convection over the oceans. Dyn. Atmos. Oceans, 10, 317-341.

Avaste O.A., G.G. Campbell, S.K. Cox, D.DeMasters, O.Ü. Kärner, K.S. Shifrin, E.A.Smith, E.J. Steiner and T.H. Vonder Haar, 1979: On the estimation of cloud-amount distribution above the world oceans. The Global Atmospheric Research Program, Grant ATM 77-15369. Dept. of Atmos. Sci., Colorado State University, Fort Collins, CO., 73 pp.

Cahalan, R.F. and J.B. Snider, 1989: Marine stratocumulus structure. Remote Sens. Environ., 28, 95-107.

Cahalan, R.F., W. Ridgway, W.J. Wiscombe and T.L. Bell, 1993: The albedo of fractal stratocumulus clouds. Submitted to J. Atmos. Sci. 1993.

Cess, R.D., G.L. Potter, J.P. Blanchet, G.J. Boer, A.D. Del Genio, M. Déqué, V. Dymnikov, V. Galin, W.L. Gates, S.J. Ghan, J.T. Kiehl, A.A. Lacis, H. Le Treut, Z.-X. Li, X.-Z. Liang, B.J. McAvaney, V.P. Melechko, J.F.B. Mitchell, J.-J. Morcrette, D.A. Randall, L. Rikus, E. Roeckner, J.F. Royer, U. Schlese, D.A. Sheinin, A. Slingo, A.P. Sokolov, K.E. Taylor, W.M. Washington, R.T. Wetherald, I. Yagai and M.-H. Zhang, 1990: Intercomparison and interpretation of climate feedback processes in 19 atmospheric general circulation models. J. of Geophys. Res., 95, 16,601-16,615.

Chang, F.-L. and J.A. Coakley, Jr., 1993: Estimating errors in fractional cloud cover obtained with infrared threshold methods. J. Geophys. Res., 98, 8,825-8,839.

Coakley, J.A., Jr., 1991: Reflections of uniform and broken layered clouds. Tellus 43B, 420-433.

Cotton, W.R. and R. Anthes, 1990: Storm and Cloud Dynamics. Intern'tl Geophysics Series, v 44, San Diego:Academic Press, 883 pp.

Eltahir, E.A.B. and R.L.Bras, 1993: Estimation of the fractional coverage of rainfall in climate models. J. Climate, 6, 639-644.

Entekhabi, D. and P.S. Eagleson, 1989: Land surface hydrology parameterization for atmospheric general circulation models including subgrid scale spatial variability. J. Climate, 2, 816-831.

Gates, W.L., 1992: AMIP: The atmospheric model intercomparison project. Bull. Amer. Meteor. Soc., 73, 1962-1970.

Harshvardhan and D.A. Randall, 1985: Comments on 'The parameterization of radiation for numerical weather prediction and climate models'. Mon. Wea. Rev., 113, 1832-1833.

Harshvardhan, B.A. Wielicki and K.M. Ginger, 1993: The interpretation of remotely sensed cloud properties from a model parameterization perspective. Submitted to J. Climate 1993.

Hartmann, D.L. and D.S. Short, 1980: On the use of earth radiation budget statistics for studies of clouds and climate. J. Atmos. Sci., 39, 431-439.

Hughes, N.A. and A. Henderson-Sellers, 1983: The effect of spatial and temporal averaging on sampling strategies for cloud amount data. Bull. Amer. Meteor. Soc., 64, 250-257.

Kedem, B., L.S. Chiu and Z. Karni, 1990: An analysis of the threshold method for measuring area-average rainfall. J. Appl. Meteor., 29, 3-20.

Kloesel, K.A., B.A. Albrecht and D.P. Wylie, 1988: FIRE marine stratocumulus observations - summary of operations and synoptic conditions. FIRE Techincal Report No. 1, Pennsylvania State University, pp. 171.

Ohring, G. and P. Clapp, 1980: The effect of changes in cloud amout on the net radiation at the top of the atmosphere. J. Atmos. Sci., 37, 447-454.

Randall, D.A., Harshvardhan, D.A. Dazlich and T.G. Corsetti, 1989: Interactions among radiation, convection, and large scale-scale dynamics in a general circulation model. J. Atmos. Sci., 46, 1943-1970.

Rossow, W.B., 1989: Measuring cloud properties from space: A review. J. Clim., 2, 201-213.

Rossow, W.B., L.C. Garder, P.-J. Lu and A. Walker, 1988: International satellite cloud climatology project (ISCCP) documentation of data. WMO/TD - No. 266, World Meteorological Organization, Geneva, 78 pp. (plus two appendices).

Rossow, W.B. and R.A. Schiffer, 1991: ISCCP cloud data products. Bull. Amer. Meteor. Soc., 72, 2-20.

Sheu, R.-S. and J.A. Curry, 1992: Interactions between North Atlantic clouds and the large-scale environment. Mon. Wea. Rev., 120, 261-278.

Slingo, J.M., 1987: The development and verification of a cloud prediction scheme for the ECMWF model. Quart. J. Roy. Meteor. Soc., 113, 899-927.

Stephens, G.L., 1984: The parametrization of radiation for numerical weather prediction and climate models. Mon. Wea. Rev., 112, 826-867.

Stephens, G.L. and T.J. Greenwald, 1991: The earth's radiation budget and its relation to atmospheric hydrology: 2. Observations of cloud effects. J. Geophys. Res., 96, 15,325-15340.

Wielicki, B.A. and L. Parker, 1992: On the determination of cloud cover from satellite sensors: the effect of sensor spatial resolution. J. Geophys. Res., 97, 12,799-12,823.

Wielicki, B.A. and R.M. Welch, 1986: Cumulus cloud field properties derived using digital data. J. Clim. Appl. Meteor., 25, 261-276.

Xu, K.-M. and S.K. Krueger, 1991: Evaluation of cloudiness parameterizations using a cumulus ensemble model. Mon. Wea. Rev., 119, 342-367.

Xu, K.-M. and D.A. Randall, 1992: The semi-empirical basis of a prognostic cloud parameterization for use in climate models. Proceedings of the 11th International Conference Clouds and Precipitation, Montreal, Canada, 1144-1147.